Science

RESEARCH ARTICLES

Cite as: H. Zhang *et al*., *Science*
10.1126/science.aea1260 (2026).

Mucosal vaccination in mice provides protection from diverse respiratory threats

Haibo Zhang[1], Katharine Floyd[2], Zhuoqing Fang[1], Filipe Araujo Hoffmann[1], Audrey Lee[1]†, Heather Marie Froggatt[3]‡, Gurpreet Bharj[1], Xia Xie[1], Haleigh B. Eppler[1], Jordan Mariah Santagata[1], Yanli Wang[1], Mengyun Hu,[1] Christopher B. Fox[4,5]§, Prabhu S. Arunachalam[6], Ralph Baric[3], Mehul S. Suthar[2], Bali Pulendran[1,7,8]*

[1]Institute for Immunity, Transplantation and Infection, Stanford University School of Medicine, Stanford University, Stanford, CA, USA. [2]Center for Childhood Infections and Vaccines of Children's Healthcare of Atlanta, Department of Pediatrics, Emory Vaccine Center, Emory National Primate Research Center, Emory University School of Medicine, Atlanta, GA, USA. [3]Department of Epidemiology, University of North Carolina at Chapel Hill, Chapel Hill, NC, USA. [4]Access to Advanced Health Institute (AAHI), Seattle, WA, USA. [5]University of Washington, Department of Global Health, Seattle, WA USA. [6]Department of Immunobiology, University of Arizona, Tucson, AZ, USA. [7]Department of Pathology, Stanford University School of Medicine, Stanford University, Stanford, CA, USA. [8]Department of Microbiology and Immunology, Stanford University School of Medicine, Stanford University, Stanford, CA, USA. Haibo Zhang[1], Katharine Floyd[2], Zhuoqing Fang[1], Filipe Araujo Hoffmann[1], Audrey Lee[1]†, Heather Marie Froggatt[3]‡, Gurpreet Bharj[1], Xia Xie[1], Haleigh B. Eppler[1], Jordan Mariah Santagata[1], Yanli Wang[1], Mengyun Hu,[1] Christopher B. Fox[4,5]§, Prabhu S. Arunachalam[6], Ralph Baric[3], Mehul S. Suthar[2], Bali Pulendran[1,7,8]*

†Present address: Genome Institute of Singapore, Singapore.

‡Present address: Department of Molecular Genetics and Microbiology, Duke University School of Medicine, Durham, NC, USA.

§Present address: Utah State University, Department of Biological Engineering, Logan, UT, USA.

***Corresponding author. Email: bpulend@stanford.edu**

Traditional vaccines target specific pathogens, limiting their scope against diverse respiratory threats. We describe an intranasal liposomal formulation combining toll-like receptor (TLR) 4 and 7/8 ligands with a model antigen, ovalbumin, that provided broad, durable protection in mice for at least 3 months against infection with SARS-CoV-2 and *Staphylococcus aureus*. In addition, the vaccine protected mice from other viruses (SARS-CoV-2, SARS, SCH014 coronavirus), bacteria (*Acinetobacter baumannii*), and allergens. Protection was mediated by persistent ovalbumin-specific $CD4^+$ and $CD8^+$ memory T cells that imprinted alveolar macrophages (AMs), enhancing antigen presentation and antiviral immunity. Following infection, vaccinated mice mounted rapid pathogen-specific T cell and antibody responses and formed ectopic lymphoid structures in the lung. These results reveal a class of “universal vaccines” against diverse respiratory threats.

Respiratory pathogens, particularly emerging and re-emerging viral and bacterial infections, pose a major threat to planetary health and global economic stability (*1*–*4*). Current vaccines are largely pathogen-specific, providing effective protection against known strains; however, their efficacy is limited in the face of microbial mutation, antigenic drift, antigenic shift, and the emergence of unknown pathogens (*5*–*8*). There is, therefore, an urgent need for the development of a broadly protective, clinically applicable vaccine targeting diverse airborne viruses and bacteria to enhance pandemic preparedness and strengthen global health security. Epidemiological studies have shown that live-attenuated vaccines such as oral polio vaccine (OPV), measles, and Bacillus Calmette-Guérin (BCG) can confer non-specific protection against unrelated infections (*9*–*13*). This effect has been partly attributed to trained immunity—a memory-like state in innate immune cells such as monocytes, which enhances responses to secondary microbial exposures through durable epigenetic and metabolic reprogramming (*14*–*17*). However, recent studies with the BCG vaccine demonstrate that such heterologous protection against diverse respiratory viruses relies on the coordinated action of vaccine-induced antigen-specific T cells, which influence the functional state of innate and non-hematopoietic cells in tissues such as alveolar macrophages and lung epithelial cells (*18*–*20*). Together, these findings reveal a complex, tissue-localized immune network involving the concerted action of the adaptive and innate immune systems along with structural cells—a phenomenon we have termed “integrated organ immunity” (*18*, *21*).

Epidemiological studies have shown that live-attenuated vaccines such as oral polio vaccine (OPV), measles, and Bacillus Calmette-Guérin (BCG) can confer non-specific protection against unrelated infections (*9*–*13*). This effect has been partly attributed to trained immunity—a memory-like state in innate immune cells such as monocytes, which enhances responses to secondary microbial exposures through durable epigenetic and metabolic reprogramming (*14*–*17*). However, recent studies with the BCG vaccine demonstrate that such heterologous protection against diverse respiratory viruses relies on the coordinated action of vaccine-induced antigen-

specific T cells, which influence the functional state of innate and non-hematopoietic cells in tissues such as alveolar macrophages and lung epithelial cells (*18*–*20*). Together, these findings reveal a complex, tissue-localized immune network involving the concerted action of the adaptive and innate immune systems along with structural cells—a phenomenon we have termed "integrated organ immunity" (*18*, *21*).

Despite these promising findings, the nonspecific effects of BCG are most pronounced when administered intravenously in mice; however, because giving vaccines through the bloodstream is neither safe nor practical in humans, their translation to large-scale use is limited. We proposed harnessing lung integrated organ immunity to develop a mucosal immunization strategy that would be broadly protective against airborne pathogens (*21*). The strategy builds on findings that intravenous BCG immunization confers broad protection against diverse respiratory viruses through MyD88-mediated TLR activation of the innate and adaptive immune responses. In addition, in the lung, antigen-specific CD4$^+$ T cells provide feedback that promotes antiviral ISG expression in alveolar epithelial and myeloid cells via IFN-γ signaling (*18*). We thus hypothesized that a mucosal vaccine that delivers TLR ligands alongside an antigen could exploit the dynamic interplay between the adaptive and innate immune systems to stimulate integrated organ immunity and protect against diverse pathogens in vivo (*21*).

Results

Intranasal vaccination with GLA-3M-052-LS + OVA confers broad and durable protection against diverse viral and bacterial infections

We evaluated an intranasal vaccine combining the TLR4 agonist GLA and the TLR7/8 agonist 3M-052-LS with ovalbumin (OVA), selected to provide a defined antigen and broad innate stimulation. Mice received four intranasal doses, and resistance to diverse respiratory pathogens was assessed over time (Fig. 1A). Upon challenge with SARS-CoV-2 at 21 days, 42 days, and 3 months post-vaccinations, vaccinated mice exhibited markedly reduced weight loss compared to unvaccinated controls (Fig. 1B). Immunohistochemistry, plaque assay, and qPCR analyses confirmed reduced SARS-CoV-2 virus load and subgenomic RNA levels in vaccinated mice (fig. S1, A and B). Histological analysis of lung tissue at day 3 post-infection revealed reduced inflammation and alveolar damage in vaccinated animals (Fig. 1C and fig. S11C). Additional studies showed that vaccination conferred cross-protection against SARS-CoV MA15 and SCH014 MA15 infections (*22*, *23*), evidenced by reduced viral titers, preserved body weight, and attenuated lung damage (fig. S1, D to I). Three to four immunizations were sufficient to confer this protective effect (fig. S12).

Mice primed with PR8 and subsequently immunized with GLA-3M-052-LS in combination with an antigen found in PR8, the nucleoprotein NP (GLA-3M-052-LS + NP) exhibited reduced SARS-CoV-2 viral loads and attenuated weight loss upon challenge at both 28 days and 2 months post-vaccinations (fig. S3), indicating that GLA-3M-052-LS can harness pre-existing antigen-specific memory cells to confer heterotypic protection.

Furthermore, vaccinated mice showed durable protection against bacterial infection with *Staphylococcus aureus* and *A. baumannii* as indicated by lower lung bacterial loads at least 3 months post vaccinations (Fig. 1, D to F).

To determine whether intranasal administration of GLA-3M-052-LS + OVA might also contribute to protection against infections acquired via nonrespiratory routes, we assessed whether intranasal vaccination protected mice against intravenous infection with *S. aureus*. Immunized mice exhibited lower kidney bacterial load and diminished weight loss compared with unvaccinated mice (fig. S11, J and K).

Finally, we evaluated the effectiveness of the GLA-3M-052-LS + OVA mucosal vaccine in immunologically experienced tissues by vaccinating mice that had been infected with PR8 four months earlier. Vaccinated non-naïve mice exhibited reduced bacterial loads in the lung compared with unvaccinated controls, and to a similar extent as vaccinated naïve mice (fig. S14). These results demonstrated that intranasal GLA-3M-052-LS + OVA induced antigen-agnostic and broadly protective immunity in both naïve and antigen-experienced hosts.

Vaccination establishes durable antigen-specific TRM responses and reprograms alveolar macrophages through epigenomic remodeling

To elucidate the cellular mechanisms underpinning the durable, non-specific protection, we characterized the innate and adaptive responses elicited by GLA-3M-052-LS + OVA immunizations. Following intranasal vaccination, multiple innate immune cell subsets up-regulated the co-stimulatory molecule CD86 and antigen presenting cells (APC)—including alveolar macrophages (AM), dendritic cells (DC), monocyte, and F4/80$^+$ macrophages—infiltrated the bronchioalveolar lavage (BAL) fluid shortly after immunization (fig. S15, A and B). While most innate immune responses returned to baseline within one week, AM activation remained elevated for at least 90 days (Fig. 2A and S5B). MHC-II expression in AM and MHC-I expression in both AM and DC remained elevated at 21 days or 3 months after vaccination, consistent with sustained antigen-presenting capacity (fig. S5, C to G).

We evaluated T cell responses using flow cytometry. Mucosal vaccination generated a high frequency of long-lived vaccine-specific (tetramer$^+$ OVA-specific) CD4$^+$ and CD8$^+$ T cells in the lungs (Fig. 2B). These T cells could produce cytokines such as

IFNγ, IL-2, TNFα, and IL-17A upon antigen stimulation (Fig. 2B and fig. S16, A to C). Furthermore, we confirmed that high frequency of $CD8^+$ and $CD4^+$ tissue resident memory T (TRM) cells, which were identified as $CD45^+TCR\beta^+CD8^+/CD4^+CD45(i.v.)^-CD44^+CD69^+CD103^+$ cells, accumulated in vaccinated lungs at least 3 months post-vaccinations (Fig. 2C and fig. S16D). These results were notable because TRMs are highly effective in conferring protection against respiratory pathogens (*24*, *25*), yet standard intramuscular immunizations do not typically induce a high magnitude of TRMs (*26*, *27*).

We next assessed cytokine profiles using Luminex. Immunization was associated with a transient but marked elevation of key inflammatory mediators in BAL fluid, including CXCL10, CCL5, CCL2, and IFN-γ, reflecting effective engagement of both innate and adaptive immune pathways (*28*) (fig. S7B). While most cytokine levels normalized within 3 days, Interferon-induced chemokines CXCL10, CCL5, soluble Receptor Activator of Nuclear Factor κB Ligand (sRANKL), and B cell Activating Factor (BAFF) remained elevated at day 7. Inflammatory cytokine levels in serum (fig. S17C) were markedly lower than those in BAL fluid (fig. S17B), suggesting that the vaccine-induced cytokine response was mostly localized within the lung.

To capture system-wide, long-term transcriptional dynamics, we conducted single cell RNA-sequencing (scRNA-seq) on 119,876 lung cells collected at multiple timepoints. Cell clustering revealed antigen presentation pathways were enriched in type 2 conventional dendritic cells (DC2), interstitial macrophage (IM), ciliated epithelial cells, and AM at 21 days post-vaccinations, and elevated gene expression levels persisted for at least 3 months in ciliated cells and AM_2 populations (fig. S8, A to C). ATII cells and AM_2 populations exhibited persistent up-regulation of antigen-presentation relative genes, such as H2-D1, H2-K1, H2-Q7, H2-Aa, and CD74 (fig. S8, D to F). We performed scATAC-seq on a total of 96,834 lung cells, revealing distinct chromatin accessibility patterns across naïve, 21 days, and 90 days post-vaccinations groups (Fig. 2D). Chromatin loci associated with the antigen presentation gene H2-Aa, interferon-stimulated genes Ccl5, Ifnαr2, inflammation-regulation gene Il10rb, and membrane lipid transport protein-GRAM Domain Containing 1B (Gramd1b) remained accessible in AM for at least 3 months post-vaccination (Fig. 2E and fig. S19C). Transcription factor (TF) motif analysis showed enrichment of AP-1, including Fos, Fosb, Jund, Jun, and Junb, across multiple populations, including T cells, ATII, AM, IM, type 1 conventional dendritic cells (DC1), neutrophils, ciliated cells, and monocytes. TF motifs of several AP-1, STATs, IRFs, and NF-κB families remained accessible in various T cell populations and AM for at least 3 months post-vaccination, consistent with features of trained immunity (*16*, *17*, *29*, *30*) (Fig. 2F and fig. S9D).

We concluded that GLA-3M-052-LS + OVA vaccination induced a robust and durable immune response, characterized by the induction of antigen-specific TRM cells and persistent reprogramming of epithelial and innate cells—particularly AMs—marked by sustained epigenetic and transcriptional changes that promote heightened antigen-presenting and antiviral states.

Antigen-specific T cells orchestrate integrated lung immunity through alveolar macrophages

To dissect the potential contribution of adaptive immunity to vaccine-induced nonspecific protection, we compared the antigen-agnostic protection of GLA-3M-052-LS with or without OVA antigen. Although both formulations provided partial protection at 21 days, the addition of OVA to vaccine formulation was required for preventing weight loss at 42 days and 3 months post-vaccinations (fig. S10A). This suggested an adaptive response requirement for long-lived heterologous protection. Depletion of both $CD4^+$ and $CD8^+$ T cells in mice throughout the immunization regimen with GLA-3M-052-LS + OVA abolished vaccine-mediated protection against SARS-CoV-2, as body weight loss and lung pathology was similar to that observed in unvaccinated mice (Fig. 3A and fig. S110B). Moreover, GLA-3M-052-LS + OVA–induced protection against bacterial loads following *S. aureus* infection were abolished in mice depleted of both $CD4^+$ and $CD8^+$ T cells (Fig. 3A). Depletion of either $CD4^+$ or $CD8^+$ T cells alone was not sufficient to abrogate GLA-3M-052-LS + OVA protective effects, indicating that both T cell populations present redundant roles (Fig. 3A).

In the context of BCG vaccination, $CD4^+$ T cell help is required for the broadly protective roles of innate cells (*18*, *19*). Consequently, we assessed whether T cell depletion impaired the training of innate immune cells in our model. In mice where $CD4^+$ and $CD8^+$ T cells were depleted, the expression of CD86 across AM, $F4/80^+$ macrophages, and DC subsets in response to GLA-3M-052-LS + OVA was decreased compared to vaccinated control mice (Fig. 3B). T cell ablation also diminished MHC-II up-regulation in AM and altered the frequency of neutrophil in lung and infiltration of DCs in BAL (fig. S11). These findings suggested a feed-forward circuit linked antigen-specific T cell responses to tissue-resident innate programming and was essential for establishing broad, heterogeneous protective immunity.

We performed single-nucleus spatial transcriptomic analysis on lungs from unvaccinated mice, vaccinated mice, and vaccinated mice depleted of $CD4^+$ and $CD8^+$ T cell during immunizations. UMAP projection of 53,645 spatially resolved nuclei revealed diverse lung cell populations, including alveolar epithelial cells, AM, interstitial macrophages (IM), DC, T, and B lymphocytes (Fig. 3C). Spatial clustering and mapping of transcriptional signatures showed marked differences in tissue organization and cellular composition across groups, with pronounced spatial reconfiguration in vaccinated lungs (Fig. 3D and fig. S112B). Consistent with our previous results, pathway-level comparisons between vaccinated and unvaccinated mice using blood transcription modules (BTMs) (*18*, *31*) indicated up-regulation of antigen presentation, phagocytosis, and anti-viral immunity activation signatures in AM of vaccinated mice. Nevertheless, these alterations were lost upon T cell-depletion (Fig. 3E and fig. S12, C and D).

Focusing on T cells, we identified distinct transcriptional clusters enriched for TRM-associated genes, including Itgae, Itgal, Runx3 (fig. S113, A and B). Spatial mapping confirmed that TRM CD8$^+$ and memory CD4$^+$ T cells preferentially accumulated in vaccinated lungs whereas their frequency and spatial residency were markedly diminished in T cell–depleted mice (fig. S113, C to E). Analysis of intercellular communication strength, integrating spatial localization and ligand-receptor expression profiles, revealed globally enhanced interactions in vaccinated lungs (Fig. 3F). We observed enriched T cell–B cell and T cell–innate cell communications, as well as reinforced signaling between AM and alveolar epithelial cells (ATI and ATII), both of which were attenuated in T cell-depleted mice.

To further dissect the molecular mediators underlying vaccine efficacy, we assessed the role of key immunomodulatory pathways between T cells and innate cells. The protein RANKL which is a critical mediator of T cell–driven regulation of innate cell survival and antigen presentation (*32*), was abundant in BAL fluid during GLA-3M-052-LS + OVA immunizations (fig. S17B). Continuous depletion of RANKL during immunizations, using an anti-RANKL antibody, eliminated vaccine-induced protection SARS-CoV-2 and *S. aureus*, exacerbating weight loss and bacterial load relative to mice that had been vaccinated with GLA-3M-052-LS + OVA in the presence of a non-specific, isotype-control, antibody (fig. S114). However, pharmacological inhibition of CD40L, IFN-γ, or TNF-α signaling (*26*) did not impact vaccine-induced protection (fig. S15). These findings indicate a role for RANKL in protection induced by GLA-3M-052-LS + OVA.

Alveolar macrophages orchestrate vaccine-induced non-specific protection

Various studies have shown that alveolar macrophages (AMs) are critical for lung surveillance and host defense (*33*, *34*, *35*). As GLA-3M-052-LS + OVA induced long-lasting epigenetic changes in AMs, we aimed to assess the role of such epigenetic changes in AM in mediating nonspecific protection. Depletion of AMs via intranasal administration of chlodronate liposomes shortly before challenge with GLA-3M-052-LS + OVA compromised protection against *S. aureus*, as evidenced by higher pathogen burden in the lung (Fig. 4A).

To determine the functional changes in AMs that may contribute to protection, we quantified phagocytic capacity across multiple target types (Fig. 4B). AMs from vaccinated mice showed higher in vivo uptake of AF594-labeled *S. aureus* (Fig. 4C), apoptotic and necrotic neutrophils (Fig. 4D), and PR8-infected lung epithelial cells (Fig. 4E) compared to AMs from unvaccinated mice. Furthermore, AMs from vaccinated mice up-regulated activation markers—including CD86, MHC-I, and MHC-II—following PR8 infection and accumulated in the alveolar space within 6 hours (fig. S16). Furthermore, based on spatial transcriptomic data, trained AMs post-vaccination exhibited enhanced antigen presentation to T cells (e.g., H2-Ab1:CD4, H2-K1:CD8, CD80:CD28), promoted inflammation and tissue repair in epithelial cells (e.g., Il1a/Il1b:Il1r1/Il1rap, Tgfb1:Tgfbr1/2), and facilitated chemotaxis and immune cell recruitment (e.g., Cxcl10: Cxcr3, Ccl3: Ccr1, Cxcl11: Cxcr3). In addition, AMs displayed enhanced adhesion and recognition capacity toward T cells, pneumocytes, and fibroblasts (e.g., Icam1:Itgal, Jam3:Jam2, Fn1:CD44) (fig. S117). These results suggested that trained AMs serve as critical early effectors of vaccine-induced protection and display enhanced functional activities.

Vaccination primes tertiary lymphoid formation and enhances antigen presentation while limiting inflammation

To investigate the spatial organization and immunological dynamics following infection, we performed multiplexed spatial protein imaging and histopathological analyses on lung tissues from vaccinated and unvaccinated mice challenged with SARS-CoV-2. Three days post challenge, lungs from vaccinated mice infected with SARS-CoV-2 exhibited distinct spatial reprogramming, as shown by RSN-based t-SNE clustering (Fig. 5, A to C). Regions enriched in vaccinated lungs were characterized by increased frequencies of immune-dense microenvironments, including region 3 and 5 that displayed great abundance of helper (CD4$^+$) and Cytotoxic (CD8$^+$) T cells, B cells, regulatory T cells, and macrophages (Fig. 5D and fig. S118, A to D). These cells were spatially organized in distinct T cell and B cell zones resembling a lymph node structure, indicative of an accelerated de novo tertiary lymphoid structure (TLS) formation (*36*, *37*) (Fig. 5E). Concomitantly, immunohistochemistry demonstrated colocalization of TLS with SARS-CoV-2 N protein (Fig. 5E). These TLS features were absent in unvaccinated controls at day 3 post-infection. Spatial distribution analysis revealed that the TLS-enriched region (region 3) was predominantly localized around the airways (fig. S118E), suggesting that vaccination primed lung tissues for rapid and structured immune engagement upon infection.

Consistent with these findings, vaccinated mice exhibited accelerated accumulation of antigen-specific NP tetramer$^+$ CD8$^+$ T cells in the lungs (Fig. 5, F and G), along with increased HA-specific total IgG and IgG2c in the BAL fluid (Fig. 5H). These immune responses were associated with decreased expression of proinflammatory cytokines, including IL-6, CXCL10, CCL2, and GM-CSF in the BAL fluid, key mediators of cytokine storm (*38*) (Fig. 5I). Furthermore, vaccination markedly reduced lung pathology and prompted early immune cell recruitment to bronchial regions within 6 hours, as revealed by dynamic histopathological analysis (Fig. 5J). Immune cell clustering was not observed in either vaccinated or unvaccinated mice prior to infection, highlighting that this response was specifically triggered by pathogen challenge (Fig. 5J). We concluded that GLA-3M-052-LS + OVA vaccinations fostered the establishment of a tissue-specific immune microenvironment that promotes rapid antigen presentation and coordinated immune responses to enable early control of infection and limit immunopathology.

GLA-3M-052-LS + OVA vaccination confers long-lasting protection against allergic asthma

Since combinatorial TLR4 and TLR7 agonism drives a potent Th1-biased immune response (*39*, *40*), we hypothesized that this mucosal vaccination strategy may also suppress Th2-driven hypersensitivity disorders, such as house dust mite (HDM)-induced asthma. Vaccinated mice exhibited reduced infiltration of eosinophils and innate lymphoid cell type 2 (ILC2), decreased Th2 cells expressing IL4, IL5, and IL13, as well as lower serum IgE levels compared to unvaccinated controls (Fig. 6, A to I). These effects persisted for at least three months (Fig. 6, A to I, and fig. S119). Histological analysis of PAS-stained lung sections further demonstrated diminished mucus hypersecretion (Fig. 6J), confirming that GLA-3M-052-LS + OVA effectively mitigated allergic asthma. Furthermore, depletion of CD4$^+$ and CD8$^+$ T cells throughout the immunization regimen abolished protection against HDM/OVA-induced asthma. In a complementary approach, T cells were similarly depleted in vaccinated Thy1.1$^+$ mice and then replaced with naïve OVA-specific CD4$^+$ T cells from OT-II transgenic mice, which express the congenic Thy1.2$^+$ marker. This transfer restored eosinophilic infiltration in the BAL and increased Th2 cytokines in the lung following OVA/alum-induced asthma, demonstrating that protection required vaccine-primed T cells (fig. S120).

Discussion

We report a mucosal vaccination strategy which elicits durable and non-specific protection against viral and bacterial pathogens, as well as allergic airway inflammation. Intranasal GLA-3M-052-LS + OVA induced OVA-specific pulmonary CD4$^+$ and CD8$^+$ memory T cells, which reduced heterologous infection and allergic inflammation by epigenetically imprinting AMs to enhance antiviral defenses, antigen uptake, and antigen presentation. In addition, immunization imprinted the tissue to rapidly form tertiary lymphoid structures upon heterologous infection, accelerating pathogen-specific T- and B-cell immunity. Given their high abundance, TRMs likely play a dominant role in orchestrating this process; however, the relative contributions of circulating memory T cells versus TRMs remain to be determined.

We propose that this approach could provide a broadly effective solution for containing emerging respiratory pathogens while also mitigating allergic inflammation. This represents a conceptual shift from traditional vaccines, which include antigens from the target pathogen. In our platform, an antigen of any specificity could be included to engage T cells, while coordinated signals from TLR4/7/8 agonists and vaccine-induced memory T cells reprogram resident alveolar macrophages to establish durable organ-level immunity. Thus, protection is not dictated by antigen specificity but instead provides broad readiness against unrelated pathogens. Previous studies, showing that infection-induced heterologous immunity can arise through tissue-resident T cells or trained alveolar macrophages, support our findings (*41–44,45*). We show that such protection can be induced without prior infection through a clinically translatable universal vaccine approach. Importantly, in addition to broad protection against respiratory viruses and bacteria, we show that vaccination can prevent allergic asthma, extending the scope of integrated organ immunity–based interventions into allergic disease (*46*, *47*). It is important to consider how these findings may translate to humans, whose mucosal immune systems are shaped by lifelong microbial and environmental exposures. Such encounters with commensals or pathogens can intermittently deliver TLR-mediated signals that may pre-condition AM and TRM compartments and provide partial or context-dependent protection. Our intranasal GLA-3M-052-LS strategy may augment or stabilize these endogenous signals in a controlled manner. Although protection was maintained in influenza-experienced mice, the more complex exposure history of adult humans may alter responsiveness. Controlled human infection studies, in which vaccinated or placebo-treated volunteers are intentionally exposed under clinical supervision, will be essential to evaluate this strategy in immunologically experienced humans.

Regarding the mechanisms of heterologous protection, different stimuli may engage distinct yet overlapping pathways. Live BCG protection depends on IFNγ, which imprint an antiviral program (*18*). By contrast, blocking IFNγ or TNF did not abrogate protection after GLA-3M-052-LS + OVA vaccination, indicating a distinct mechanism. Whereas BCG maintains persistent IFNγ-secreting effector T cells, we propose that GLA-3M-052-LS plus OVA vaccination induces TRMs and circulating memory T cells that sustain protection through RANKL-mediated reprogramming of AMs, independent of IFNγ. Protection was T cell–dependent, and adjuvant alone provided only transient (~3 weeks) effects. Notably, in lower-injury infections such as SARS-CoV-2, resident AMs alone were sufficient to mount protective innate memory (*33*). Thus the protection mediated by memory T cell–driven RANKL signaling in AMs could represent a form of integrated organ immunity that sustains broad heterologous protection (*21*).

Beyond lowering pathogen burden, our findings suggest that GLA-3M-052-LS + antigen may also mitigate immunopathology. The vaccine reprograms AMs toward enhanced phagocytosis, promoting rapid clearance of pathogens and damaged cells, thereby limiting excessive inflammation—a major driver of mortality in severe infections (*48*,*49*,*50*). Concurrently, reprogrammed AMs sustain elevated CD86 and MHC-II for up to 3 months. Following infection, they rapidly enter BAL and promote tertiary lymphoid structures, enabling efficient recall responses (*51*, *52*). Thus, integrated organ immunity not only reduces pathogen burden in an antigen-agnostic manner but also imprints the tissue with innate memory that accelerates pathogen-specific adaptive responses. Together, these features suggest that this strategy could convert infections into organ-level immune imprinting that build lasting immunity.

Several vaccines have been reported to provide heterologous protection, including live-attenuated vaccines such as BCG, oral poliovirus (OPV), and measles–mumps–rubella (MMR), which can reduce all-cause infectious mortality (*9*–*13*). However, these off-target effects are variable and context-dependent, and mechanistically unclear. By contrast, our intranasal GLA-3M-052-LS strategy couples TLR4/7/8 co-activation with antigen-driven T cell engagement to reprogram AMs and support TRM formation, establishing integrated organ immunity against diverse respiratory viruses, bacteria, and allergens. The choice of GLA (TLR4) and 3M-052 (TLR7/8) was motivated by their complementary MyD88-dependent pathways and favorable safety records; both have been studied in non-human primates and entered clinical evaluation (*53*,*54*), increasing translational feasibility. Given that two to four intranasal doses conferred protection in mice, future optimization to 2 doses and use of user-friendly devices such as nasal sprays may enable practical deployment in humans. In this setting, influenza or SARS-CoV-2 antigens could be used, leveraging widespread pre-existing memory T cells from prior infection or vaccination. In addition, by enabling programmable, mucosal, non-specific protection, this approach offers a foundation for the development of universal vaccines that confer broad and durable protection against diverse respiratory pathogens and beyond. This could serve as an early pandemic countermeasure, providing broad protection before strain-matched vaccines are available. Outside pandemic settings, seasonal administration could protect against influenza, common cold viruses, RSV, and other respiratory threats—ultimately paving the way toward a truly universal vaccine.

Materials and Methods

Mice

C57BL/6J mice (strain no. 000664) were purchased from Jackson Laboratories. Female mice aged 6 to 8 weeks were used for GLA-3M-052-LS + OVA immunizations, while male mice of the same age range were used for GLA-3M-052-LS + NP immunization study. B6.PL-*Thy1*^{a}/CyJ (B6 Thy1.1, strain no. 000406) and B6.Cg-Tg(TcraTcrb)425Cbn/J (OT-II, strain no. 004194) were obtained from Jackson Laboratories. All animals were maintained on a 12 hours light/12 hours dark cycle at 18 to 23 °C and 40 to 60% humidity. All procedures were approved by the Institutional Animal Care and Use Committees of Stanford University (IACUC protocol number 32681), and of Emory University (IACUC protocol number 201700309). Mice were randomly assigned to experimental groups.

GLA-3M-052-LS adjuvant formulations and immunization

Mice were immunized intranasally (i.n.) with antigen admixed with a synthetic liposomal adjuvant formulation containing the Toll-like receptor (TLR) agonists GLA (TLR4) and 3M-052 (TLR7/8). The adjuvant (GLA-3M-052-LS) was provided by the Access to Advanced Health Institute (AAHI, Seattle, WA) at a stock concentration of 1 mg/mL GLA and 0.4 mg/mL 3M-052 in a PEGylated liposomal suspension. For each immunization, 10 μg of GLA and 4 μg of 3M-052 were delivered in a 20 μL total volume (10 μL per nostril). Antigens were co-administered in the same 20 μL volume: 25 μg of chicken ovalbumin (OVA EndoFit™; InvivoGen, Cat. No. vac-pova) or 5 μg of influenza nucleoprotein (Recombinant Influenza A/Puerto Rico/8/34/Mount Sinai NP Protein; Sino Biological, Cat.No.11675-V08B1). Antigen and adjuvant were mixed immediately prior to administration.

SARS-CoV-2 B.1.351 virus and cell culture

Vero E6-TMPRSS2 cells were kindly provided by B. Graham (Vaccine Research Center, NIH). SARS-CoV-2 B.1.351 seed stock (GISAID: EPI_ISL_890360) was provided by A. Pekosz (Johns Hopkins University). Viral stocks were propagated in Vero E6-TMPRSS2 cells, and titers were determined by plaque assay. Cells were cultured in complete Dulbecco's Modified Eagle Medium (DMEM) supplemented with puromycin (10 μg/mL, Gibco, A11138-03). All virus stocks were deep-sequenced to confirm identity.

SARS-CoV-2 B.1.351 mouse infections and viral burden analysis

Viral challenge was conducted as previously described (*18*). Briefly, to perform SARS-CoV-2 (B.1.351) infection, the virus was prepared by dilution in 0.9% sterile saline (MedLine, RDI30296). Mice were anesthetized using isoflurane and subsequently intranasally inoculated with 50 µL of viral suspension containing 1×10^6 plaque-forming units (PFU) per animal within an ABSL-3 containment facility. Body weight was recorded daily to monitor disease progression. At 3 days post-infection, animals were euthanized by isoflurane overdose, and one lung lobe was harvested into tubes pre-filled with TRIzol reagent (Roche, 11667165001) and homogenized using a Bead Ruptor 24 (Omni International; 5.15 m/s for 15 s). Total RNA was purified using the Direct-zol RNA Miniprep Kit (Zymo, R2051), followed by reverse transcription using a commercial cDNA synthesis kit (Thermo Fisher, 4368813). Gene expression was subsequently quantified by qPCR using the QuantStudio 5 system, Subgenomic-specific TaqMan primer/probe sets and PR8 M protein gene expression primer-were used as previously described (*18*, *33*). For the plaque assay, at the indicated day post-infection, mice were euthanized and lung tissue was collected in revvity Bead Ruptor tubes filled with 1% FBS–Hanks' balanced salt solution (HBSS). Tissue was homogenized in an Omni Bead Ruptor 24 instrument (5.15 m/s, 15 s). To perform plaque assays, 10-fold dilutions of the viral supernatant in serum-free DMEM (catalog number 30-2002, ATCC) were overlaid onto VeroE6-TMPRSS2-hACE2 cells monolayers and adsorbed for 1 hour at 37°C. After adsorption, 0.6% immunodiffusion agarose in 2× DMEM supplemented with 5% FBS (Corning 35-016-CV) and 1× sodium bicarbonate was overlaid, and cultures were incubated for 48 hours at 37°C. Agarose plugs were removed, cells were fixed with 4% PBS-buffered paraformaldehyde (PFA) for 15 min at room temperature, and plaques were visualized using crystal violet staining (20% methanol in double-distilled water).

Mouse-adapted coronavirus infection experiments

Mouse-adapted SARS-CoV MA15 and SCH014 MA15 strains were propagated and handled in accordance with previously established protocols and with approval from the Institutional Review Board at the University of North Carolina (UNC) at Chapel Hill (*23*). Female mice aged 20 weeks were anesthetized with a ketamine/xylazine cocktail and intranasally administered 50 µL of phosphate-buffered saline (PBS) containing either 1×10^4 PFU of SARS-CoV MA15 or 1×10^5 PFU of SCH014 MA15. Body weights were monitored daily following infection. Animals exposed to SCH014 MA15 were euthanized at day 4 post-infection, while those challenged with SARS-CoV MA15 were euthanized at days 2 and 4 to assess disease progression. For virological analysis, gross lung pathology was assessed, and the inferior right lung lobe was collected for viral titer determination. Lung tissues were homogenized in 1 mL PBS, centrifuged to remove debris, and serial dilutions of the supernatants were applied to confluent monolayers of Vero E6 cells. Viral titers were quantified by plaque assay using an agarose overlay (0.8% in culture medium), followed by visualization of plaques with Neutral Red staining after a 2-day incubation at 37°C. All infection procedures were performed under ABSL-3 conditions, in facilities certified by the CDC and UNC Environmental Health and Safety. Experimental procedures were approved by the UNC Institutional Biosafety Committee and the Institutional Animal Care and Use Committee (IACUC protocol #22-155.0) and were conducted following institutional biosafety and animal welfare guidelines.

PR8 influenza virus infection

Influenza A/PR/8/34 (H1N1) (PR8 virus) was generously provided by the Y.-H. Chien lab at Stanford. PR8 was propagated in MDCK cells as previously described (*55*). Virus stocks (1×10^8 PFU/mL) were stored at −80 °C. Mice were anesthetized with isoflurane and intranasally infected with 200 PFU of PR8 diluted in 20 µL PBS (10 µL per nare).

Bacterial strains and culture conditions

Methicillin-sensitive *S. aureus* TCH1516 [USA300-HOU-MR] (ATCC BAA-1717) and *A. baumannii* (ATCC 19606) were obtained from ATCC and handled under BSL-2 conditions. Strains were cultured according to ATCC recommendations and previously published protocols (*56*–*58*). Briefly, *S. aureus* and *A. baumannii* were grown on blood agar plates at 37 °C overnight in a static incubator. One to two isolated colonies were transferred into Todd Hewitt broth (*S. aureus*) or in Lennox broth/agar (LB) (*A. baumannii*) and cultured at 240 rpm for 14 to 16 hours at 37 °C. Bacterial cells were harvested by centrifugation at 5000 × g for 5 min at room temperature (RT), washed with PBS, and resuspended. Colony-forming units (CFUs) were determined by serial dilution and plating on blood agar. Bacteria were diluted to the desired concentrations for in vivo experiments.

Bacterial infection and burden assessment

Vaccinated or unvaccinated mice were intravenous (i.v.) challenged with 1×10^6 CFU of *S. aureus* or intranasally (i.n.) challenged with 5×10^6 CFU of *S. aureus* or 1×10^7 CFU of *A. baumannii* in 25 µL (12.5 µL per nostril) under isoflurane anesthesia. The CFU inoculum was determined by optical density (OD_{600}) and calculated based on bacterial growth curves. Twenty-four hours post-infection, mice were euthanized via isoflurane overdose. Lungs or kidneys were collected in 1 mL of cold PBS and homogenized at 5 m/s for 15 s, repeated four times using a tissue grinder, while maintaining cold conditions. Homogenates were serially diluted (1:10, 1:100, and 1:500 in PBS) and plated on blood agar. After 24 h incubation at 37 °C, colonies were counted and reported as CFU per gram of lung tissue.

Asthma model

House Dust Mite (HDM) extract containing *Dermatophagoides pteronyssinus* was purchased from Greer Laboratories Inc. (Cat. No.XPB82D3A25, Lot No. 385931). The lyophilized protein was reconstituted to a stock concentration of 1 mg/mL and aliquoted for storage at –20 °C. On day 0, vaccinated or unvaccinated mice were sensitized with 20 µg of HDM in 20 µL of ddH_2O intranasally under isoflurane anesthesia. From days 7 to 11, mice were challenged daily with 20 µg of HDM in 20 µL of ddH_2O. On day 13, all mice were euthanized, and peripheral blood, bronchoalveolar lavage fluid (BALF), and lung tissues were collected for further analysis. Each experimental group included at least five mice.

Histopathological analysis

Lungs were preserved in 4% Formaldehyde Solution or 10% neutral buffered formalin followed by paraffin embedding and sectioning. Histology was performed by HistoWitz, Inc and Histo-tec laboratory Inc. Briefly, slides were stained with H&E, Periodic Acid–Schiff Staining or subjected to immunohistochemistry (IHC) with an antibody specific for SARS-CoV-2 nucleocapsid protein (GeneTex, Cat. No. GTX635686). The stained lung slides 3 days after SARS-CoV-2 infection were read by a board-certified veterinary pathologist and scored from 0 to 5 for perivascular inflammation, bronchial/bronchiolar alveolar degeneration/necrosis, bronchial/bronchiolar inflammation and alveolar inflammation or from 0 to 3 for extent of IHC positivity in the bronchi and alveoli. A narrative description of leukocyte classes and histopathological findings observed was also provided. The score of lungs 4 days after SARS-CoV MA15 or SCH014 MA15 infection was given by UNC-Chapel Hill Lab based on Gross Pathology: 0 – no congestion noted; 1 – more than half of the left lung; 2 – no more than one lobe worth of tissue involved in congestion multiple lobes involved, no more than half of the total lung tissue; 3 – most of the lung involved, congestion generally looks severe but there are still healthy patches; 4 – lung looks like a liver, All tissue shows congestion, deep red/purple color.

In vivo depletion with antibodies

Antibodies used for depletion are listed in table S1. Mice received a single intraperitoneal dose of antibody every 2 to 3 days consecutively, the detail dose is provided in the corresponding figure legend.

Luminex assay

BAL and blood were collected from mice at the indicated timepoints. BALF was collected from mice and cell-free supernatants were stored at –80 °C until analysis. BALF was used directly without dilution. Blood was centrifuged at 10,000 rpm, 1 min at RT in the serum gel tubes, serum was collected. Luminex assay was performed on BALF and serum using Mouse 48-plex Procarta kits (Thermo Fisher Scientific, Cat. No. EPX480-20834-901) according to the manufacturer's protocol and modifications as previously described (*18*). Each sample was measured in singlets. Plates were read on an FM3D FlexMap instrument with a lower bound of 50 beads per sample per cytokine/chemokine.

ELISA

The concentrations of IgE in serum were determined using commercially available ELISA kits (BD OptEIA Cat. No. 555138) according to the manufacturer's instructions. The relative HA-specific total IgG, IgG1, and IgG2c were quantitated by Elisa plate coating with HA protein (Cat. No. 50-161-7183, Sino Biological Influenza A H1N1 (A/Puerto Rico/8/1934) Hemagglutinin / HA Protein (ECD,His Tag), 100 ng/50 µL PBS) and test with secondary antibodies (goat anti-mouse IgG, IgG1, IgG2c, SouthernBiotech, Cat. No. 1030-05, 1071-05, 1078-05, 1:6000). In all experiments, absorbance was detected using a Varioskan Flash multilabel counter (Thermo Fisher Scientific) to determine concentrations based on a standard curve drawn on each plate.

Flow cytometry analysis of innate immune cells in BAL and lungs

Bronchoalveolar lavage (BAL) was performed to collect cells and soluble mediators from the lungs. Mice were euthanized by CO_2 inhalation, and the trachea was cannulated using a 20G angiocatheter. The lungs were lavaged twice with 1 mL of ice-cold PBS per wash, yielding a total volume of approximately 1.8 to 2 mL. The recovered BAL fluid was centrifuged at 500 g for 5 min at 4 °C to separate cells from the supernatant. Red blood cells (RBCs) were lysed using ACK (ammonium–chloride–potassium) lysis buffer (Quality Biological), and the cell pellets were resuspended in flow cytometry staining buffer. Supernatants were stored at –80 °C for subsequent ELISA or Luminex assays.

Following euthanasia by CO_2 inhalation, lungs were harvested at the indicated time points and digested with 5 mL of enzymatic digestion buffer (1 mg/mL type IV collagenase and 100 ng/mL DNase I) and then dissociated using the gentleMACS dissociator (program m_lung_01). After enzymatic digestion at 37 °C with shaking at 180 rpm for 30 min, lungs were further processed using the lung_02 program. The resulting lung cell suspension was passed through a 100 µm cell strainer and subjected to RBC lysis with ACK buffer. Single cells were stained with innate panel antibodies for 30 min at

4°C (table S2). Samples were then washed twice with 1× PBS + 2% fetal bovine serum (FBS) and fixed with BD Cytofix (BD, Cat. No. 554655). Compensation was set using compensation beads (Invitrogen, Cat. No. 01-3333-42), Counting beads (Invitrogen, Cat. No. 01-1234-42) were added 10 min before loading samples onto flow cytometry. Samples were analyzed on a BD FACS Symphony analyzer with BD FACS Diva v.8.0.1.

Ex vivo stimulation of OVA-specific T cells.

Single-cell suspensions were prepared from mouse lungs. Cells were processed using a 70 to 40% Percoll gradient and centrifuged at 2500 rpm for 20 min at RT with the lowest acceleration and no brake. Mononuclear cells were collected from the interphase and resuspended in complete RPMI-1640 medium and plated at 1 to 2×10^6 cells per well in 96-well U-bottom plates. Cells were restimulated with 100 µg/mL ovalbumin (OVA) protein, 1 µg/ml OVA peptide pool (PepTivator® Ovalbumin, Miltenyi Biotec, Cat. No.130-099-771), or individual OVA peptides (1 µg/mL OVA 257-264, invivoGen, Cat. No. vac-sin, 1 µg/mL OVA 323-339, invivogen, Cat. No. vac-isq) at 37 °C in 5% CO_2. Brefeldin A (1:1000; Invitrogen, Cat. 00-4506-51) was added after 2 h. For OVA peptide pool stimulation, cells were incubated for 6 h total; for OVA protein or individual peptide stimulation, cells were incubated overnight. Stimulated cells were harvested and processed for intracellular cytokine staining.

Intracellular cytokine-staining assay for antigen-specific T cells

Cells were stained using a protocol as previously described (*59*). Briefly, cells were stained with Ghost Dye Violet 510 for 10 min at 4°C in PBS. After washing, cells were blocked with Fc receptor antibody α-CD16/32 for 5 min, OVA Class II Tetramer was stained at RT for 1 hour and directly add T cells antibodies (table S2). Cells were incubated for 30 min at 4°C and washed twice with PBS + 2% FBS. If the intracellular staining was needed, cells were then permeabilized with BD Fix/Perm for 20 min at RT and washed with 1 × Perm for two times, then stained intracellularly with T cells antibodies in 1× Perm buffer (table S2). Cells were then washed twice with 1× Perm buffer and fixed with BD Cytofix for 10 min at RT. Data were acquired on a BD Symphony analyzer and analyzed using FlowJo v.10.

Intravascular labeling and identification of lung tissue-resident T cells

To discriminate circulating from tissue-resident T cells in the lung, intravenous (*i.v.*) labeling was performed as previously described (*60*, *61*). Briefly, mice were injected intravenously via tail vein with 3 µg of anti-CD45 antibody, diluted in 100 µL of sterile PBS, 3 min prior to euthanasia. Following injection, mice were euthanized and perfused via the right ventricle with 10 mL of cold PBS to remove circulating blood cells. Lungs were harvested and processed into single-cell suspensions. After Fc block, cells were stained ex vivo with fluorochrome-conjugated Tissue-resident memory T cells (TRM) antibodies (table S2). TRM were identified as $CD45^+TCR\beta^+CD8^+/CD4^+CD45(i.v.)^-CD44^+CD69^+CD103^+$ cells.

Phagocytosis assay of alveolar macrophages

Isolation of neutrophils

Neutrophils were isolated from the bone marrow of C57BL/6 mice as previously described (*46*). Briefly, femurs and tibias were harvested, and bone marrow cells were flushed using HBSS supplemented with 2% FBS and 2 mM EDTA. After filtration through a 70 µm cell strainer, red blood cells were lysed using ACK lysis buffer. The remaining cells were layered over 3 mL Histopaque 1077 (Sigma, 10771-100ML; density 1.077 g/mL) and 3 mL of 72% Percoll (Merck, P1644) in a 15 mL conical tube. Centrifugation was performed for 30 minutes at 750 g at 25 °C using the lowest acceleration and zero deceleration settings. Neutrophils were collected from the interface between the Histopaque and Percoll layers and resuspended in culture medium. Neutrophil purity was confirmed by flow cytometry for Ly6G expression.

UV-induced cell death

To induce apoptosis and necrosis, purified neutrophils were suspended in HBSS at a concentration of 1×10^7 cells/mL and plated as a thin monolayer in a sterile, lid-open 6-well plate. Cells were irradiated with UV light (254 nm) for 15 minutes using the germicidal lamp inside a Class II biosafety cabinet (BSL-2). Subsequently, cells were incubated at 37 °C for 2 hours to allow for the progression of apoptosis or secondary necrosis. Cell viability and death status were assessed via Annexin V and Zombie UV staining.

A549 cell culture and infection with PR8

A549 human lung epithelial cells (ATCC, Cat.No. CCL-185) were maintained in DMEM supplemented with 10% FBS, 100 U/mL penicillin, and 100 µg/mL streptomycin at 37 °C with 5% CO_2. Cells were infected with Influenza A virus (PR8, A/Puerto Rico/8/34 H1N1) at a multiplicity of infection (MOI) of 500 in DMEM culture medium. After 24 hours, cells were harvested and washed twice with PBS.

Fluorescent labeling

Apoptotic and necrotic neutrophils, as well as PR8-infected A549 cells, were labeled with pHrodo Green succinimidyl ester (SE) dye (Thermo Fisher Scientific, Cat. No. P35369) according to the manufacturer's instructions. Briefly, cells were incubated with 10 μM pHrodo SE in sodium bicarbonate buffer (pH 8.4) for 30 min at RT, followed by two washes with PBS to remove unbound dye. Fluorescence labeling was validated by comparing signal intensity in MES buffer (pH 5.5) versus PBS (pH 7.4) to confirm pH sensitivity.

In vivo phagocytosis assay

A total of 1 × 10^6 labeled apoptotic/necrotic neutrophils, 1 × 10^5 PR8-infected epithelial cells, or 20 μg *S. aureus* (AF594, Thermo Fisher Scientific, Cat. No. S23372) in 25 μL PBS were administered intranasally into anesthetized vaccinated or unvaccinated mice. Mice were euthanized by CO_2 inhalation 30 minutes post-instillation. BAL was collected and centrifuged (5 min at 500 g, 4 °C), and cells were stained with innate panel antibodies (table S2). In the bacterial phagocytosis assay, cells were incubated with 0.2% Trypan blue for 3 min on ice and washed one time, then stained with antibodies cocktail. Data were acquired on a BD Symphony analyzer and analyzed using FlowJo v.10.

Alveolar macrophages depletion

Alveolar macrophages depletion was done as previously described with minor modifications (*62*). To deplete alveolar macrophages (AM), mice were lightly anesthetized with isoflurane and administered 50 μL of clodronate liposomes (Liposoma BV, Netherlands) intranasally on two consecutive days. Control mice received the same volume of PBS-containing control liposomes. The efficiency of AM depletion was verified 48 hours after the second administration via flow cytometry analysis of BAL cells. Cells were stained with fluorochrome-conjugated antibodies against CD45, CD11c, Siglec-F, and viability dye, and AMs were identified as $CD45^+CD11c^+Siglec\text{-}F^+$ viable singlets. More than 90% depletion of AMs was typically achieved with this protocol.

OT-II $CD4^+$ T cell adoptive transfer and OVA–alum asthma model

Vaccinated or unvaccinated B6.PL-Thy1a/CyJ recipient mice received 1 × 10^6 Thy1.2 OT-II $CD4^+$ T cells via *i.v.* injection on day 21 after the final immunization. The OVA–alum asthma model was established as described previously (*63*). Briefly, 75 μg of OVA (Albumin from chicken egg white, Sigma, Cat. No. A5503-1G) was adsorbed onto 2 mg of aluminum hydroxide (Alhydrogel 2%, InvivoGen, Cat. No. vac-alu-10) by rotating the mixture overnight at 4 °C. The OVA–alum preparation was administered intraperitoneally on days 42 and 49. Mice were subsequently challenged intranasally with 50 μg of OVA daily on days 56 through 58. Anti-Thy1.1 antibody (200 μg per dose, i.p.) was administered according to the experimental timeline to deplete $Thy1.1^+$ T cells, as indicated. All mice were euthanized on day 60. Bronchoalveolar lavage (BAL) and lung tissues were collected for downstream immunological and histological analyses.

Cell preparation for scAb-seq and scATAC-Seq

Lung immune and epithelial cells were isolated using a modified enzymatic digestion protocol from a previous study with minimal modification (*18*). Mice were euthanized and lungs were perfused and lavaged with digestion buffer composed of RPMI-1640 supplemented with elastase (Worthington), dispase II (Sigma-Aldrich), and DNase I (Sigma-Aldrich). Lung tissues were then excised, minced into small fragments, and further digested in RPMI-1640 containing liberase (Sigma-Aldrich) and DNase I at 37°C for 30 min. Following enzymatic digestion, single-cell suspensions were obtained by passing the mixture through a 100 μm cell strainer and red blood cells were lysed using ACK lysis buffer. To enrich for specific cell subsets, cells were stained with surface markers targeting $CD11b^+$, $EpCAM^+$, and $CD11c^+$ populations. $CD3^+$ T cells were enriched following FACS protocol. Cells were sorted using a FACSAria cell sorter (BD Biosciences) after staining with oligo antibodies (table S3). $CD11b^+$, $EpCAM^+$, $CD11c^+$, $CD3^+$ cells and the non-sorted fraction were combined at a 1:1:1:1:6 ratio and resuspended in cold PBS supplemented with 1% BSA (Miltenyi Biotec) and 0.5 U/μL RNase inhibitor (Sigma-Aldrich) for scRNA-seq. $CD11b^+$, $EpCAM^+$, $CD11c^+$ and the non-sorted fraction were combined at a 1:1:1:7 ratio and resuspended in BD OMICS Guard buffer (BD Biosciences, Cat. 570911)

scRNA-seq analysis

To simultaneously assess whole-transcriptome and targeted surface protein expression at the single-cell level, BD Rhapsody single-cell multi-omics technology was employed. Mouse lung cells were thawed and resuspended in FACS buffer prior to dextramer-based flow cytometric sorting for $CD11b^+$, $EpCAM^+$, $CD11c^+$, $CD3^+$ cells. Sorted cells were collected into staining buffer at a concentration of 200–800 cells/μL in ~600 μL per sample. Approximately half of the collected cells were loaded onto the BD Rhapsody Cartridge (BD Biosciences, Cat. #633733) using the associated BD Rhapsody Cartridge Reagent Kit (Cat. #633731). Cells were captured in microwell arrays with barcoded beads, followed by cell lysis, bead retrieval, cDNA synthesis, template switching, and Klenow extension. Full-length cDNA containing unique molecular identifiers (UMIs) and cell barcodes were PCR-amplified. Whole-transcriptome was prepared using the BD Rhapsody Whole Transcriptome Amplification Kit (Cat. #633801) following the manufacturer's instructions. Libraries were sequenced on the Illumina NovaSeq X Plus platform (Illumina, San Diego, CA). Raw sequencing data were processed using the BD Rhapsody Analysis Pipeline (v2.2.1) on VELSERA cloud platform and aligned to the GRCm39 reference genome. Output files were further converted to

SEURAT, H5MU, and SCANPY formats for downstream analysis and visualization using standard R packages or the Cellismo tool (BD). Quality control filters excluded cells with mitochondrial transcript fractions >25%, fewer than 200 detected genes, or >20,000 total reads. Potential doublets were identified and removed using ScDblFinder. Filtered counts were then scaled by a factor of 10,000 and log-transformed, and the top 2000 most variable genes were selected for principal component analysis. Clustering and UMAP visualization were performed using the first 30 principal components, with Seurat SNN graph construction followed by Louvain community detection. Differential expression was computed using the Wilcoxon rank-sum test, and gene-set enrichment analysis was performed on genes ranked by the Wald statistic. ComplexHeatmap (v2.2.0) was used for heatmap visualization.

scATAC-seq analysis

Single-nucleus chromatin accessibility profiling was performed using the BD Rhapsody Single-Cell ATAC-Seq platform, which employs a modified Tn5 transposase to simultaneously fragment genomic DNA and insert sequencing adapters into accessible chromatin regions of individual nuclei. Libraries were sequenced on the AVITI system (Element Biosciences, San Diego, CA) to investigate chromatin structure and regulatory elements at single-cell resolution. Cryopreserved cells stored in BD OMICS-Guard buffer (Cat. #570911) for less than 48 hours were centrifuged at 800 × g for 5 min to remove the preservation buffer. Without additional washing, cells were resuspended in BD sample buffer at ~800 cells/μL for downstream ATAC-seq processing. Splint beads were prepared using a custom splint oligonucleotide specific to V3 capture beads provided by BD Biosciences. Nuclei were isolated following a modified protocol (*64*). Briefly, cell pellets were lysed and resuspended in Nuclei Buffer using a wide-bore pipette, aiming for a concentration of 10,000 nuclei/μL. In situ tagmentation was performed by incubating the nuclei with a Tagmentase mix that targets accessible chromatin regions, generating DNA fragments with preloaded adapter sequences. An aliquot of tagmented nuclei was stained with DyeCycle Green (1 mM) and counted using the BD Rhapsody Scanner. Single-nucleus capture, cell lysis, and genomic DNA processing were performed according to the BD Rhapsody manufacturer's protocol. DNA fragments were captured via splint-oligo-bonded TSO (template-switch oligo) strands. Ligase was used to ligate the bead-bound oligos to the tagmented DNA, followed by gap filling and extension using a specific enzyme mix. Final denaturation removed DNA templates from beads, and Illumina-compatible adapters and sample indices were introduced during amplification. Libraries were prepared with the following sequencing parameters: Read 1: 50 cycles, Read 2: 50 cycles, Index 1: 8 cycles, and Index 2: 60 cycles. Sequencing data were analyzed using the BD Rhapsody ATAC Large Input pipeline (v2.2.1) on VELSERA cloud platform. Processed output files were used for secondary analysis and visualization using the Signac package (v1.14.0). In brief, fragment files were imported and used to create a Seurat object with a chromatin assay via the Create Chromatin Assay function. Quality control (QC) filtering was applied based on several metrics, including the total number of unique fragments per cell, nucleosome banding pattern score (nucleosome signal), transcription start site (TSS) enrichment score, and the fraction of reads overlapping ENCODE blacklist regions. Cells not meeting established thresholds (TSS enrichment > 3, nucleosome signal < 0.5, blacklist ratio < 0.08, number of peaks < 15000, number of peaks > 500, fraction of overlapping peaks > 0.4) were excluded from downstream analysis. Normalization was performed using term frequency–inverse document frequency (TF-IDF), followed by dimensionality reduction via singular value decomposition (SVD). Clustering was carried out using shared nearest neighbor (SNN) modularity optimization, and two-dimensional embedding was generated using Uniform Manifold Approximation and Projection (UMAP). A gene activity matrix was computed using the GeneActivity (Signac) function to infer gene-level accessibility based on the aggregation of chromatin accessibility signals over gene bodies and promoter regions. Motif enrichment and transcription factor activity were assessed using chromVAR.

Spatial transcriptomics

Lung tissues from C57BL/6 mice were freshly harvested, embedded in optimal cutting temperature (OCT) compound, and immediately snap-frozen in liquid nitrogen. Samples were stored at –80°C until sectioning. Spatially resolved single-nucleus transcriptomic profiling was performed using the Curio Trekker Single-Cell Spatial Mapping Kit (Cat. Nos. SK017 and SK020; Takara Bio). Briefly, 25 μm cryosections of mouse lung tissue were placed onto Trekker 10 × 10 mm glass tiles, each embedded with a monolayer of uniquely DNA-barcoded microparticles (beads). Upon exposure to ultraviolet (UV) light, the spatial DNA barcodes were photocleaved and internalized into the overlying tissue. Following UV exposure and barcode incorporation, the tissue was dissociated from the tile into single-nucleus suspensions. These spatially tagged nuclei were then loaded onto the BD Rhapsody Single-Cell system (BD Biosciences) for single-nucleus capture and transcriptomic profiling. Spatial transcriptomics data were processed using Seurat (v5.1.0) and analyzed using the Squidpy package (v1.6.2) in Python. Spatial neighborhood graphs were constructed using Squidpy's sq.gr.spatial_neighbors function, which uses spatial coordinates to define the connectivity between spots. For spatial feature enrichment, we computed co-occurrence and neighborhood enrichment scores across clusters using sq.gr.co_occurrence and sq.gr.nhood_enrichment. Spatial ligand-receptor interaction analysis was conducted with SOAPy (v1.0.1) (*65*) using a curated database of known interactions (cellphonedb v5), enabling inference of potential cell–cell communication events.

Multiplexed spatial protein imaging by PhenoCycler-Fusion system

Multiplexed spatial protein imaging was performed using the PhenoCycler Fusion (PCF, Akoya Biosciences) according to the manufacturer's protocol. Lung tissues from C57BL/6 mice were harvested, fixed in 4% paraformaldehyde (PFA), dehydrated, embedded in paraffin (FFPE), and sectioned at 5 µm thickness. Sections were deparaffinized, rehydrated, subjected to antigen retrieval. Sections were then stained with a cocktail of primary antibodies conjugated with unique DNA barcodes using an automated staining workflow. Following staining and fixation steps, the slides were stored in buffer until imaging. Antibody panels included markers for immune, epithelial, endothelial, and stromal cell subsets (table S4). For imaging, slides were mounted onto the PhenoCycler Fusion instrument. A flow cell was placed on the slides, the reporter plate was prepared, and the experimental template generated using the PhenoCycler Experiment Designer was loaded into the Fusion software. Reporter hybridization, imaging, and dehybridization cycles were performed fully automatically by the PhenoCycler Fusion system.

Quality control (QC)

Image analysis was performed using QuPath software. Antibody performance QC was determined by 1 to 2 experienced scientists after reviewing the QPTiff image in QuPath. The explanation of the QC scores is shown in table S5. First, the specificity of the antibody marker was compared to the reference images from Akoya's mouse spleen references. If the marker had a similar staining pattern as the reference images, it was marked as specific staining and a level of 4 for intensity was determined. If no signal was found on one tissue but was found on the other tissues, the marker has a score of 0. If the signal-to-noise ratio was low and there was high background noise, the marker had a score of 1. If the signal-to-noise ratio was high, the marker had a score of 2. If the signal was saturated at the maximum intensity, the marker had a score of 3. Only markers with scores above 1 were recommended for downstream analysis. Tissue artifact QC was manually removed using the brush selection tool in QuPath. The artifacts include out-of-focus, tissue folding, debris and bubbles on any of the markers.

Cell segmentation

Nuclear segmentation was first performed using StarDist method applied to the DAPI channel. Cytoplasm segmentation was then estimated from nuclear expansion by morphological dilation, and the centroid of each cell was defined by the x-y coordinates in the image. The mean fluorescent intensity (MFI) of each marker was calculated for each segmented cell from the corresponding expression compartment, e.g., nuclear or cytoplasmic surface, to produce a raw expression table where each row represents a cell and columns are their x-y coordinates and protein MFI expressions.

Supervised phenotyping

Phenotypes and their corresponding markers are listed in table S6. Multiple training regions of interest (ROIs) were selected across multiple samples to create a combined training image. The training ROIs should capture heterogeneity in cell phenotypes and marker intensities. On training ROIs, "Add Points" tool was used to select representative cells for each phenotype based on the expression markers. For example, for "Cytotoxic T cells" phenotype, 10 to 20 cells with double positive staining of CD8 and CD3e markers were chosen. The selection of cells had to capture both high and low intensity of CD8$^+$ cells to accommodate the heterogeneity of marker expression on different areas and different samples. After selecting training cells for all phenotypes, the "Train Object Classifier", artificial neural network classifier was used to train the phenotyping model. For features, the markers listed in table S6 and their expression compartment MFI were selected. "Live update" was selected to visualize the phenotyping results and to adjust the training cells by adding or removing cells. When finished live adjustment, the classifier was applied to the whole slide images. After phenotyping, the percentage of each phenotype i within each sample j was calculated and plotted as a bar chart.

Cellular neighborhood analysis

The spatial interactions between different cell phenotypes were quantified using the Cellular Neighborhood method in CytoMap software. The input data were the CSV files from QuPath Export Measurements, with x-y coordinates, region/sample annotation, phenotype classification and MFI for each marker for every segmented cells. The raster-scanned 50-µm-radius circle creates a table of neighborhoods, in which the position of each neighborhood is evenly distributed across the tissue in a grid pattern. Once neighborhoods were defined, phenotypes were used to cluster them into five regions using the default NN Self-Organizing Map algorithm. The phenotype composition was calculated for each cellular neighborhood and plotted on a heatmap. Dimensionality reduction was applied for data visualization by means of tSNE using the training markers MFI and the neighborhood model. tSNE was performed using the Barnes-Hut algorithm with Euclidean distance and parameters were set to 30 for perplexity, 4 for exaggeration, and 0.5 for theta.

REFERENCES AND NOTES

1. T. W. Crowther, R. Rappuoli, C. Corinaldesi, R. Danovaro, T. J. Donohue, J. Huisman, L. Y. Stein, J. K. Timmis, K. Timmis, M. Z. Anderson, L. R. Bakken, M. Baylis, M. J. Behrenfeld, P. W. Boyd, I. Brettell, R. Cavicchioli, C. S. Delavaux, C. M. Foreman, J. K. Jansson, B. Koskella, K. Milligan-McClellan, J. A. North, D. Peterson, M. Pizza, J. L. Ramos, D. Reay, J. V. Remais, V. I. Rich, W. J. Ripple, B. K. Singh, G. R. Smith, F. J. Stewart, M. B. Sullivan, J. van den Hoogen, M. J. H. van Oppen, N. S. Webster, C. M. Zohner, L. G. van Galen, Scientists' call to action: Microbes, planetary health, and the Sustainable Development Goals. *Cell* **187**, 5195–5216 (2024). doi:10.1016/j.cell.2024.07.051 Medline
2. B. S. Graham, N. J. Sullivan, Emerging viral diseases from a vaccinology perspective: Preparing for the next pandemic. *Nat. Immunol.* **19**, 20–28 (2018). doi:10.1038/s41590-017-0007-9 Medline
3. D. M. Morens, A. S. Fauci, Emerging Pandemic Diseases: How We Got to COVID-19. *Cell* **182**, 1077–1092 (2020). doi:10.1016/j.cell.2020.08.021 Medline
4. G. B. D. A. R. Collaborators; GBD 2019 Antimicrobial Resistance Collaborators, Global mortality associated with 33 bacterial pathogens in 2019: A systematic analysis for the Global Burden of Disease Study 2019. *Lancet* **400**, 2221–2248 (2022). doi:10.1016/S0140-6736(22)02185-7 Medline
5. D. M. Morens, J. K. Taubenberger, A. S. Fauci, Rethinking next-generation vaccines for coronaviruses, influenzaviruses, and other respiratory viruses. *Cell Host Microbe* **31**, 146–157 (2023). doi:10.1016/j.chom.2022.11.016 Medline
6. R. Rappuoli, G. Alter, B. Pulendran, Transforming vaccinology. *Cell* **187**, 5171–5194 (2024). doi:10.1016/j.cell.2024.07.021 Medline
7. K. Subbarao, The success of SARS-CoV-2 vaccines and challenges ahead. *Cell Host Microbe* **29**, 1111–1123 (2021). doi:10.1016/j.chom.2021.06.016 Medline
8. H. Kiyono, P. B. Ernst, Nasal vaccines for respiratory infections. *Nature* **641**, 321–330 (2025). doi:10.1038/s41586-025-08910-6 Medline
9. S. J. C. F. M. Moorlag, R. J. W. Arts, R. van Crevel, M. G. Netea, Non-specific effects of BCG vaccine on viral infections. *Clin. Microbiol. Infect.* **25**, 1473–1478 (2019). doi:10.1016/j.cmi.2019.04.020 Medline
10. P. Aaby, B. Samb, F. Simondon, A. M. C. Seck, K. Knudsen, H. Whittle, Non-specific beneficial effect of measles immunisation: Analysis of mortality studies from developing countries. *BMJ* **311**, 481–485 (1995). doi:10.1136/bmj.311.7003.481 Medline
11. P. Aaby, A. Roth, H. Ravn, B. M. Napirna, A. Rodrigues, I. M. Lisse, L. Stensballe, B. R. Diness, K. R. Lausch, N. Lund, S. Biering-Sørensen, H. Whittle, C. S. Benn, Randomized trial of BCG vaccination at birth to low-birth-weight children: Beneficial nonspecific effects in the neonatal period? *J. Infect. Dis.* **204**, 245–252 (2011). doi:10.1093/infdis/jir240 Medline
12. N. Lund, A. Andersen, A. S. K. Hansen, F. S. Jepsen, A. Barbosa, S. Biering-Sørensen, A. Rodrigues, H. Ravn, P. Aaby, C. S. Benn, The Effect of Oral Polio Vaccine at Birth on Infant Mortality: A Randomized Trial. *Clin. Infect. Dis.* **61**, 1504–1511 (2015). doi:10.1093/cid/civ617 Medline
13. P. Aaby, M. G. Netea, C. S. Benn, Beneficial non-specific effects of live vaccines against COVID-19 and other unrelated infections. *Lancet Infect. Dis.* **23**, e34–e42 (2023). doi:10.1016/S1473-3099(22)00498-4 Medline
14. R. J. W. Arts, S. J. C. F. M. Moorlag, B. Novakovic, Y. Li, S.-Y. Wang, M. Oosting, V. Kumar, R. J. Xavier, C. Wijmenga, L. A. B. Joosten, C. B. E. M. Reusken, C. S. Benn, P. Aaby, M. P. Koopmans, H. G. Stunnenberg, R. van Crevel, M. G. Netea, BCG Vaccination Protects against Experimental Viral Infection in Humans through the Induction of Cytokines Associated with Trained Immunity. *Cell Host Microbe* **23**, 89–100.e5 (2018). doi:10.1016/j.chom.2017.12.010 Medline
15. E. Kaufmann, J. Sanz, J. L. Dunn, N. Khan, L. E. Mendonça, A. Pacis, F. Tzelepis, E. Pernet, A. Dumaine, J.-C. Grenier, F. Mailhot-Léonard, E. Ahmed, J. Belle, R. Besla, B. Mazer, I. L. King, A. Nijnik, C. S. Robbins, L. B. Barreiro, M. Divangahi, BCG Educates Hematopoietic Stem Cells to Generate Protective Innate Immunity against Tuberculosis. *Cell* **172**, 176–190.e19 (2018). doi:10.1016/j.cell.2017.12.031 Medline
16. M. G. Netea, J. Domínguez-Andrés, L. B. Barreiro, T. Chavakis, M. Divangahi, E. Fuchs, L. A. B. Joosten, J. W. M. van der Meer, M. M. Mhlanga, W. J. M. Mulder, N. P. Riksen, A. Schlitzer, J. L. Schultze, C. Stabell Benn, J. C. Sun, R. J. Xavier, E. Latz, Defining trained immunity and its role in health and disease. *Nat. Rev. Immunol.* **20**, 375–388 (2020). doi:10.1038/s41577-020-0285-6 Medline
17. F. Wimmers, M. Donato, A. Kuo, T. Ashuach, S. Gupta, C. Li, M. Dvorak, M. H. Foecke, S. E. Chang, T. Hagan, S. E. De Jong, H. T. Maecker, R. van der Most, P. Cheung, M. Cortese, S. E. Bosinger, M. Davis, N. Rouphael, S. Subramaniam, N. Yosef, P. J. Utz, P. Khatri, B. Pulendran, The single-cell epigenomic and transcriptional landscape of immunity to influenza vaccination. *Cell* **184**, 3915–3935.e21 (2021). doi:10.1016/j.cell.2021.05.039 Medline
18. A. Lee, K. Floyd, S. Wu, Z. Fang, T. K. Tan, H. M. Froggatt, J. M. Powers, S. R. Leist, K. L. Gully, M. L. Hubbard, C. Li, H. Hui, D. Scoville, A. D. Ruggiero, Y. Liang, A. Pavenko, V. Lujan, R. S. Baric, G. P. Nolan, P. S. Arunachalam, M. S. Suthar, B. Pulendran, BCG vaccination stimulates integrated organ immunity by feedback of the adaptive immune response to imprint prolonged innate antiviral resistance. *Nat. Immunol.* **25**, 41–53 (2024). doi:10.1038/s41590-023-01700-0 Medline
19. K. A. Tran, E. Pernet, M. Sadeghi, J. Downey, J. Chronopoulos, E. Lapshina, O. Tsai, E. Kaufmann, J. Ding, M. Divangahi, BCG immunization induces $\text{CX3CR1}^{\text{hi}}$ effector memory T cells to provide cross-protection via IFN-γ-mediated trained immunity. *Nat. Immunol.* **25**, 418–431 (2024). doi:10.1038/s41590-023-01739-z Medline
20. K. L. Hilligan, S. Namasivayam, C. S. Clancy, P. J. Baker, S. I. Old, V. Peluf, E. P. Amaral, S. D. Oland, D. O'Mard, J. Laux, M. Cohen, N. L. Garza, B. A. P. Lafont, R. F. Johnson, C. G. Feng, D. Jankovic, O. Lamiable, K. D. Mayer-Barber, A. Sher, Bacterial-induced or passively administered interferon gamma conditions the lung for early control of SARS-CoV-2. *Nat. Commun.* **14**, 8229 (2023). doi:10.1038/s41467-023-43447-0 Medline
21. B. Pulendran, Integrated organ immunity: A path to a universal vaccine. *Nat. Rev. Immunol.* **24**, 81–82 (2024). doi:10.1038/s41577-024-00990-1 Medline
22. S. R. Leist, K. H. Dinnon 3rd, A. Schäfer, L. V. Tse, K. Okuda, Y. J. Hou, A. West, C. E. Edwards, W. Sanders, E. J. Fritch, K. L. Gully, T. Scobey, A. J. Brown, T. P. Sheahan, N. J. Moorman, R. C. Boucher, L. E. Gralinski, S. A. Montgomery, R. S. Baric, A Mouse-Adapted SARS-CoV-2 Induces Acute Lung Injury and Mortality in Standard Laboratory Mice. *Cell* **183**, 1070–1085.e12 (2020). doi:10.1016/j.cell.2020.09.050 Medline
23. V. D. Menachery, B. L. Yount Jr., K. Debbink, S. Agnihothram, L. E. Gralinski, J. A. Plante, R. L. Graham, T. Scobey, X.-Y. Ge, E. F. Donaldson, S. H. Randell, A. Lanzavecchia, W. A. Marasco, Z.-L. Shi, R. S. Baric, A SARS-like cluster of circulating bat coronaviruses shows potential for human emergence. *Nat. Med.* **21**, 1508–1513 (2015). doi:10.1038/nm.3985 Medline
24. D. H. Paik, D. L. Farber, Anti-viral protective capacity of tissue resident memory T cells. *Curr. Opin. Virol.* **46**, 20–26 (2021). doi:10.1016/j.coviro.2020.09.006 Medline
25. D. Masopust, A. G. Soerens, T. Tissue-Resident, Tissue-Resident T Cells and Other Resident Leukocytes. *Annu. Rev. Immunol.* **37**, 521–546 (2019). doi:10.1146/annurev-immunol-042617-053214 Medline
26. C. Li, A. Lee, L. Grigoryan, P. S. Arunachalam, M. K. D. Scott, M. Trisal, F. Wimmers, M. Sanyal, P. A. Weidenbacher, Y. Feng, J. Z. Adamska, E. Valore, Y. Wang, R. Verma, N. Reis, D. Dunham, R. O'Hara, H. Park, W. Luo, A. D. Gitlin, P. Kim, P. Khatri, K. C. Nadeau, B. Pulendran, Mechanisms of innate and adaptive immunity to the Pfizer-BioNTech BNT162b2 vaccine. *Nat. Immunol.* **23**, 543–555 (2022). doi:10.1038/s41590-022-01163-9 Medline
27. L. Grigoryan, A. Lee, A. C. Walls, L. Lai, B. Franco, P. S. Arunachalam, Y. Feng, W. Luo, A. Vanderheiden, K. Floyd, S. Wrenn, D. Pettie, M. C. Miranda, E. Kepl, R. Ravichandran, C. Sydeman, N. Brunette, M. Murphy, B. Fiala, L. Carter, R. L. Coffman, D. Novack, H. Kleanthous, D. T. O'Hagan, R. van der Most, J. S. McLellan, M. Suthar, D. Veesler, N. P. King, B. Pulendran, Adjuvanting a subunit SARS-CoV-2 vaccine with clinically relevant adjuvants induces durable protection in mice. *NPJ Vaccines* **7**, 55 (2022). doi:10.1038/s41541-022-00472-2 Medline
28. I. Rauch, M. Müller, T. Decker, The regulation of inflammation by interferons and their STATs. *JAK-STAT* **2**, e23820 (2013). doi:10.4161/jkst.23820 Medline
29. S. L. Hayward, C. D. Scharer, E. K. Cartwright, S. Takamura, Z. T. Li, J. M. Boss, J. E. Kohlmeier, Environmental cues regulate epigenetic reprogramming of airway-resident memory CD8^+ T cells. *Nat. Immunol.* **21**, 309–320 (2020). doi:10.1038/s41590-019-0584-x Medline
30. E. Glasmacher, S. Agrawal, A. B. Chang, T. L. Murphy, W. Zeng, B. Vander Lugt, A. A. Khan, M. Ciofani, C. J. Spooner, S. Rutz, J. Hackney, R. Nurieva, C. R. Escalante, W. Ouyang, D. R. Littman, K. M. Murphy, H. Singh, A genomic regulatory element that directs assembly and function of immune-specific AP-1-IRF complexes. *Science* **338**, 975–980 (2012). doi:10.1126/science.1228309 Medline

31. P. S. Arunachalam, M. K. D. Scott, T. Hagan, C. Li, Y. Feng, F. Wimmers, L. Grigoryan, M. Trisal, V. V. Edara, L. Lai, S. E. Chang, A. Feng, S. Dhingra, M. Shah, A. S. Lee, S. Chinthrajah, S. B. Sindher, V. Mallajosyula, F. Gao, N. Sigal, S. Kowli, S. Gupta, K. Pellegrini, G. Tharp, S. Maysel-Auslender, S. Hamilton, H. Aoued, K. Hrusovsky, M. Roskey, S. E. Bosinger, H. T. Maecker, S. D. Boyd, M. M. Davis, P. J. Utz, M. S. Suthar, P. Khatri, K. C. Nadeau, B. Pulendran, Systems vaccinology of the BNT162b2 mRNA vaccine in humans. *Nature* **596**, 410–416 (2021). doi:10.1038/s41586-021-03791-x Medline
32. D. M. Anderson, E. Maraskovsky, W. L. Billingsley, W. C. Dougall, M. E. Tometsko, E. R. Roux, M. C. Teepe, R. F. DuBose, D. Cosman, L. Galibert, A homologue of the TNF receptor and its ligand enhance T cell growth and dendritic-cell function. *Nature* **390**, 175–179 (1997). doi:10.1038/36593 Medline
33. A. Lercher, J.-G. Cheong, M. J. Bale, C. Jiang, H.-H. Hoffmann, A. W. Ashbrook, T. Lewy, Y. S. Yin, C. Quirk, E. J. DeGrace, L. Chiriboga, B. R. Rosenberg, S. Z. Josefowicz, C. M. Rice, Antiviral innate immune memory in alveolar macrophages following SARS-CoV-2 infection ameliorates secondary influenza A virus disease. *Immunity* **57**, 2530–2546.e13 (2024). doi:10.1016/j.immuni.2024.08.018 Medline
34. L. Sun, H. Zhang, H. Zhang, X. Lou, Z. Wang, Y. Wu, X. Yang, D. Chen, B. Guo, A. Zhang, F. Qian, Staphylococcal virulence factor HlgB targets the endoplasmic-reticulum-resident E3 ubiquitin ligase AMFR to promote pneumonia. *Nat. Microbiol.* **8**, 107–120 (2023). doi:10.1038/s41564-022-01278-7 Medline
35. Y. D. Woo, D. Jeong, D. H. Chung, Development and Functions of Alveolar Macrophages. *Mol. Cells* **44**, 292–300 (2021). doi:10.14348/molcells.2021.0058 Medline
36. S. M. Guillaume, W. S. Foster, I. San Martín Molina, E. M. Watson, S. Innocentin, G. M. Kennedy, A. E. Denton, M. A. Linterman, Lung B cells in ectopic germinal centers undergo affinity maturation. *Proc. Natl. Acad. Sci. U.S.A.* **122**, e2416855122 (2025). doi:10.1073/pnas.2416855122 Medline
37. J. E. Moyron-Quiroz, J. Rangel-Moreno, K. Kusser, L. Hartson, F. Sprague, S. Goodrich, D. L. Woodland, F. E. Lund, T. D. Randall, Role of inducible bronchus associated lymphoid tissue (iBALT) in respiratory immunity. *Nat. Med.* **10**, 927–934 (2004). doi:10.1038/nm1091 Medline
38. J. Nie, L. Zhou, W. Tian, X. Liu, L. Yang, X. Yang, Y. Zhang, S. Wei, D. W. Wang, J. Wei, Deep insight into cytokine storm: From pathogenesis to treatment. *Signal Transduct. Target. Ther.* **10**, 112 (2025). doi:10.1038/s41392-025-02178-y Medline
39. G. Napolitani, A. Rinaldi, F. Bertoni, F. Sallusto, A. Lanzavecchia, Selected Toll-like receptor agonist combinations synergistically trigger a T helper type 1-polarizing program in dendritic cells. *Nat. Immunol.* **6**, 769–776 (2005). doi:10.1038/ni1223 Medline
40. S. P. Kasturi, I. Skountzou, R. A. Albrecht, D. Koutsonanos, T. Hua, H. I. Nakaya, R. Ravindran, S. Stewart, M. Alam, M. Kwissa, F. Villinger, N. Murthy, J. Steel, J. Jacob, R. J. Hogan, A. García-Sastre, R. Compans, B. Pulendran, Programming the magnitude and persistence of antibody responses with innate immunity. *Nature* **470**, 543–547 (2011). doi:10.1038/nature09737 Medline
41. E. M. Cipolla, M. Yue, K. L. Nickolich, B. R. Huckestein, D. Antos, W. Chen, J. F. Alcorn, Heterotypic Influenza Infections Mitigate Susceptibility to Secondary Bacterial Infection. *J. Immunol.* **209**, 760–771 (2022). doi:10.4049/jimmunol.2200261 Medline
42. B. Slütter, N. Van Braeckel-Budimir, G. Abboud, S. M. Varga, S. Salek-Ardakani, J. T. Harty, Dynamics of influenza-induced lung-resident memory T cells underlie waning heterosubtypic immunity. *Sci. Immunol.* **2**, eaag2031 (2017). doi:10.1126/sciimmunol.aag2031 Medline
43. H. Aegerter, J. Kulikauskaite, S. Crotta, H. Patel, G. Kelly, E. M. Hessel, M. Mack, S. Beinke, A. Wack, Influenza-induced monocyte-derived alveolar macrophages confer prolonged antibacterial protection. *Nat. Immunol.* **21**, 145–157 (2020). doi:10.1038/s41590-019-0568-x Medline
44. H. Gu, X. Zeng, L. Peng, C. Xiang, Y. Zhou, X. Zhang, J. Zhang, N. Wang, G. Guo, Y. Li, K. Liu, J. Gu, H. Zeng, Y. Zhuang, H. Li, J. Zhang, W. Zhang, Q. Zou, Y. Shi, Vaccination induces rapid protection against bacterial pneumonia via training alveolar macrophage in mice. *eLife* **10**, e69951 (2021). doi:10.7554/eLife.69951 Medline
45. J. Yan *et al.*, A protein-free vaccine stimulates innate immunity and protects against nosocomial pathogens, *Sci Transl Med.* **15**, adf9556 (2023). doi:10.1126/scitranslmed.adf9556 Medline
46. H. Zhang, K. Xue, W. Li, X. Yang, Y. Gou, X. Su, F. Qian, L. Sun, Cullin5 drives experimental asthma exacerbations by modulating alveolar macrophage antiviral immunity. *Nat. Commun.* **15**, 252 (2024). doi:10.1038/s41467-023-44168-0 Medline
47. A. Didierlaurent, J. Goulding, S. Patel, R. Snelgrove, L. Low, M. Bebien, T. Lawrence, L. S. van Rijt, B. N. Lambrecht, J.-C. Sirard, T. Hussell, Sustained desensitization to bacterial Toll-like receptor ligands after resolution of respiratory influenza infection. *J. Exp. Med.* **205**, 323–329 (2008). doi:10.1084/jem.20070891 Medline
48. A. C. Doran, A. Yurdagul Jr., I. Tabas, Efferocytosis in health and disease. *Nat. Rev. Immunol.* **20**, 254–267 (2020). doi:10.1038/s41577-019-0240-6 Medline
49. C. J. Martin, M. G. Booty, T. R. Rosebrock, C. Nunes-Alves, D. M. Desjardins, I. Keren, S. M. Fortune, H. G. Remold, S. M. Behar, Efferocytosis is an innate antibacterial mechanism. *Cell Host Microbe* **12**, 289–300 (2012). doi:10.1016/j.chom.2012.06.010 Medline
50. R. P. H. De Maeyer, R. C. van de Merwe, R. Louie, O. V. Bracken, O. P. Devine, D. R. Goldstein, M. Uddin, A. N. Akbar, D. W. Gilroy, Blocking elevated p38 MAPK restores efferocytosis and inflammatory resolution in the elderly. *Nat. Immunol.* **21**, 615–625 (2020). doi:10.1038/s41590-020-0646-0 Medline
51. B. A. Helmink, S. M. Reddy, J. Gao, S. Zhang, R. Basar, R. Thakur, K. Yizhak, M. Sade-Feldman, J. Blando, G. Han, V. Gopalakrishnan, Y. Xi, H. Zhao, R. N. Amaria, H. A. Tawbi, A. P. Cogdill, W. Liu, V. S. LeBleu, F. G. Kugeratski, S. Patel, M. A. Davies, P. Hwu, J. E. Lee, J. E. Gershenwald, A. Lucci, R. Arora, S. Woodman, E. Z. Keung, P.-O. Gaudreau, A. Reuben, C. N. Spencer, E. M. Burton, L. E. Haydu, A. J. Lazar, R. Zapassodi, C. W. Hudgens, D. A. Ledesma, S. Ong, M. Bailey, S. Warren, D. Rao, O. Krijgsman, E. A. Rozeman, D. Peeper, C. U. Blank, T. N. Schumacher, L. H. Butterfield, M. A. Zelazowska, K. M. McBride, R. Kalluri, J. Allison, F. Petitprez, W. H. Fridman, C. Sautès-Fridman, N. Hacohen, K. Rezvani, P. Sharma, M. T. Tetzlaff, L. Wang, J. A. Wargo, B cells and tertiary lymphoid structures promote immunotherapy response. *Nature* **577**, 549–555 (2020). doi:10.1038/s41586-019-1922-8 Medline
52. L. Zhao, S. Jin, S. Wang, Z. Zhang, X. Wang, Z. Chen, X. Wang, S. Huang, D. Zhang, H. Wu, Tertiary lymphoid structures in diseases: Immune mechanisms and therapeutic advances. *Signal Transduct. Target. Ther.* **9**, 225 (2024). doi:10.1038/s41392-024-01947-5 Medline
53. S. Pillet, É. Aubin, S. Trépanier, J.-F. Poulin, B. Yassine-Diab, J. ter Meulen, B. J. Ward, N. Landry, Humoral and cell-mediated immune responses to H5N1 plant-made virus-like particle vaccine are differentially impacted by alum and GLA-SE adjuvants in a Phase 2 clinical trial, *npj Vaccines*. **3**, 3 (2018). doi:10.1038/s41541-017-0043-3 Medline
54. W. O. Hahn *et al.*, Use of 3M-052-AF with Alum adjuvant in HIV trimer vaccine induces human autologous neutralizing antibodies, *JEM* **221**, e20240604 (2024). doi:10.1084/jem.20240604
55. K. J. Szretter, A. L. Balish, J. M. Katz, Influenza: propagation, quantification, and storage. Curr Protoc Microbiol Chapter 15, Unit 15G 11 (2006).
56. S. Vivas-Alegre, I. Fernández-Natal, E. López-Fidalgo, O. M. Rivero-Lezcano, Preparation of inocula for experimental infection of blood with Streptococcus pneumoniae. *MethodsX* **2**, 463–468 (2015). doi:10.1016/j.mex.2015.11.003 Medline
57. N. P. Vitko, A. R. Richardson, Laboratory maintenance of methicillin-resistant Staphylococcus aureus (MRSA). *Curr Protoc Microbiol.* **9**, Unit 9C2 (2013). doi:10.1002/9780471729259.mc09c02s28 Medline
58. D. M. Missiakas, O. Schneewind, Growth and laboratory maintenance of Staphylococcus aureus. *Curr Protoc Microbiol.* **9**, Unit 9C 1 (2013). doi:10.1002/9780471729259.mc09c01s28 Medline
59. C. Sinclair, G. Bommakanti, L. Gardinassi, J. Loebbermann, M. J. Johnson, P. Hakimpour, T. Hagan, L. Benitez, A. Todor, D. Machiah, T. Oriss, A. Ray, S. Bosinger, R. Ravindran, S. Li, B. Pulendran, mTOR regulates metabolic adaptation of APCs in the lung and controls the outcome of allergic inflammation. *Science* **357**, 1014–1021 (2017). doi:10.1126/science.aaj2155 Medline
60. K. G. Anderson, K. Mayer-Barber, H. Sung, L. Beura, B. R. James, J. J. Taylor, L. Qunaj, T. S. Griffith, V. Vezys, D. L. Barber, D. Masopust, Intravascular staining for discrimination of vascular and tissue leukocytes. *Nat. Protoc.* **9**, 209–222 (2014). doi:10.1038/nprot.2014.005 Medline
61. E. M. Steinert, J. M. Schenkel, K. A. Fraser, L. K. Beura, L. S. Manlove, B. Z. Igyártó,

P. J. Southern, D. Masopust, Quantifying Memory CD8 T Cells Reveals Regionalization of Immunosurveillance. *Cell* **161**, 737–749 (2015). doi:10.1016/j.cell.2015.03.031 Medline

62. A. S. Neupane, M. Willson, A. K. Chojnacki, F. Vargas E Silva Castanheira, C. Morehouse, A. Carestia, A. E. Keller, M. Peiseler, A. DiGiandomenico, M. M. Kelly, M. Amrein, C. Jenne, A. Thanabalasuriar, P. Kubes, Patrolling Alveolar Macrophages Conceal Bacteria from the Immune System to Maintain Homeostasis. *Cell* **183**, 110–125.e11 (2020). doi:10.1016/j.cell.2020.08.020 Medline
63. H. Zhang, R. Wei, X. Yang, L. Xu, H. Jiang, M. Li, H. Jiang, H. Zhang, Z. Chen, F. Qian, L. Sun, AMFR drives allergic asthma development by promoting alveolar macrophage-derived GM-CSF production. *J. Exp. Med.* **219**, e20211828 (2022). doi:10.1084/jem.20211828 Medline
64. M. R. Corces, A. E. Trevino, E. G. Hamilton, P. G. Greenside, N. A. Sinnott-Armstrong, S. Vesuna, A. T. Satpathy, A. J. Rubin, K. S. Montine, B. Wu, A. Kathiria, S. W. Cho, M. R. Mumbach, A. C. Carter, M. Kasowski, L. A. Orloff, V. I. Risca, A. Kundaje, P. A. Khavari, T. J. Montine, W. J. Greenleaf, H. Y. Chang, An improved ATAC-seq protocol reduces background and enables interrogation of frozen tissues. *Nat. Methods* **14**, 959–962 (2017). doi:10.1038/nmeth.4396 Medline
65. H. Wang, J. Li, S. Jing, P. Lin, Y. Qiu, X. Yan, J. Yuan, Z. Tang, Y. Li, H. Zhang, Y. Chen, Z. Wang, H. Li, SOAPy: A Python package to dissect spatial architecture, dynamics, and communication. *Genome Biol.* **26**, 80 (2025). doi:10.1186/s13059-025-03550-5 Medline
66. Z. Fang, H. Zhang, Spatial transcriptomics dataset. Version V1 (Zenodo, 2025); https://zenodo.org/records/17651970.

ACKNOWLEDGMENTS

We thank M. Moore, Y. Hou, and Y. Peymanfar at Akoya involved in running mutipul-protein staining samples. We thank G. Gowrishankar for her help with the CODEX imaging work. We thank the NIH Tetramer Core Facility (NIH Contract 75N93020D00005 and RRID:SCR_026557) for providing the OVA specific Class I and Class II tetramers, and NP specific Class I Tetramers. **Funding:** The study was supported by NIH grants, the Violetta L. Horton Professor endowment, the Soffer Fund endowment and Open Philanthropy to B.P. A portion of this work was supported by AI167966 (R.S.B.) **Author contributions:** Conceptualization: B.P. and H.Z. Methodology: H.Z., K.F., Z.F., F.A.H., A.L., H.M.F., G.B., X.X., H.B.E., J.M.S., Y.W., and M.H., Investigation: C.B.F., P.S.A., R.B., and M.S.S. Funding acquisition: B.P. Project administration: B.P. and H.Z. Supervision: B.P. Writing – original draft: H.Z. Writing – review and editing: B.P., F.A.H., Z.F., X.X., G.B., K.F., A.L., C.B.F., P.S.A., R.B., M.S.S., H.B.E., and Y.W. **Competing Interests:** C.B.F. is a member of the Scientific Advisory Board of Maxvax LLC and have performed consulting services for AAHI and Merck. C.B.F. is an inventor on patent (US11266602B2) held by AAHI that covers the composition of the adjuvant formulation. R.S.B. holds patents on sarbecovirus vaccine design and norovirus therapeutics designs. He also has ongoing collaborations with Hillivax, GIVAX, Vaxart, MERK, Takeda Vaccines, and Maine Biotech. B.P. serves or has served on the External Immunology Board of GSK and on the Scientific Advisory Board of Sanofi, Medicago, Boehringer Ingelheim, Pharmajet, Icosavax, Imu Biosciences and Ed-Jen, and holds shares at CircBio and Orbital Therapeutics, B.P. and H.Z. are inventors on the provisional patent application (S25-533: "A universal vaccine that generates cross-protective immunity against diverse respiratory threats") that is being prepared for submission by Stanford University. In addition, B.P. and A.L. are inventors on the PCT (S23-361_STAN-2138WO_PCT: A universal vaccine strategy for conferring protection against diverse pathogens), that has been filed by Stanford University. Both patent applications cover a universal vaccine that generates cross-protective immunity against diverse respiratory threats. The other authors declare that they have no competing interests. **Data, code, and materials availability:** The adjuvant GLA-3M-052-LS is available from AAHI (Access to Advanced Health Institute) under a material agreement. All data for ssRNA-seq, ssATAC-seq, and spatial transcriptomics have been deposited in the NCBI Gene Expression Omnibus (accession number GSE310116). All code for spatial transcriptomics has been deposited on Zenodo (*66*). All other data are available in the paper or the supplementary materials.

SUPPLEMENTARY MATERIALS

science.org/doi/10.1126/science.aea1260
Figures S1 to S20
Tables S1 to S6

Received 27 June 2025; resubmitted 30 September 2025
Accepted 30 January 2026
Published online 19 February 2026

10.1126/science.aea1260

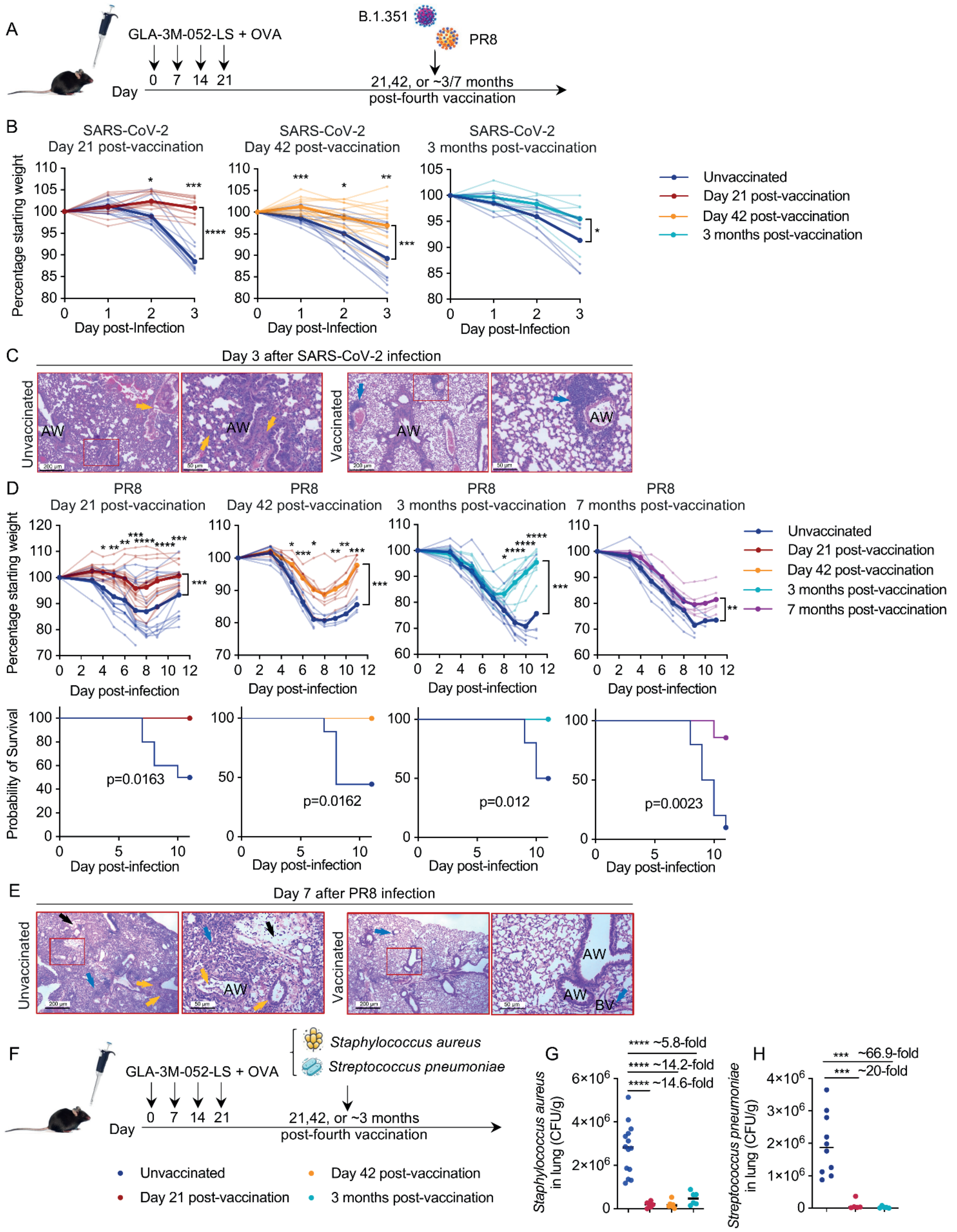
A
GLA-3M-052-LS + OVA
Day
0 7 14 21
B.1.351
PR8
21,42, or ~3/7 months
post-fourth vaccination
B
SARS-CoV-2
Day 21 post-vaccination
SARS-CoV-2
Day 42 post-vaccination
SARS-CoV-2
3 months post-vaccination
Percentage starting weight
Day post-Infection
Unvaccinated
Day 21 post-vaccination
Day 42 post-vaccination
3 months post-vaccination
C
Day 3 after SARS-CoV-2 infection
Unvaccinated
Vaccinated
AW
D
PR8
Day 21 post-vaccination
PR8
Day 42 post-vaccination
PR8
3 months post-vaccination
PR8
7 months post-vaccination
Percentage starting weight
Day post-infection
Unvaccinated
Day 21 post-vaccination
Day 42 post-vaccination
3 months post-vaccination
7 months post-vaccination
Probability of Survival
p=0.0163
p=0.0162
p=0.012
p=0.0023
Day post-infection
E
Day 7 after PR8 infection
Unvaccinated
Vaccinated
AW
BV
F
Staphylococcus aureus
Streptococcus pneumoniae
GLA-3M-052-LS + OVA
Day
0 7 14 21
21,42, or ~3 months
post-fourth vaccination
Unvaccinated
Day 21 post-vaccination
Day 42 post-vaccination
3 months post-vaccination
G
**** ~5.8-fold
**** ~14.2-fold
**** ~14.6-fold
Staphylococcus aureus in lung (CFU/g)
6×10^6
4×10^6
2×10^6
0
H
*** ~66.9-fold
*** ~20-fold
Streptococcus pneumoniae in lung (CFU/g)
4×10^6
3×10^6
2×10^6
1×10^6
0

Fig. 1. Intranasal GLA-3M-052-LS + OVA vaccination confers robust and long-lasting protection against SARS-CoV-2, PR8 influenza virus, *S. aureus*, and *Streptococcus pneumoniae* infections. (**A**) Experimental strategy for SARS-CoV-2 and PR8 infection. (**B**) Body weight changes following SARS-CoV-2 challenge 21 days (*n* = 12 for each group), 42 days (*n* = 13 unvaccinated mice, 15 vaccinated mice), and 3 months (*n* = 9 unvaccinated mice, 7 vaccinated mice) post vaccinations. (**C**) Representative H&E-stained lung sections from vaccinated and unvaccinated mice at day 3 post SARS-CoV-2 infection (21 days after vaccinations). Blue arrows show representative immune cell infiltrated area; yellow arrows show alveolar wall thickening and epithelial cell damage. AW, airway. Scale bar: left, 200 μm; right, 50 μm. (**D**) Experimental strategy for *S. aureus* and *A. baumannii* infection. (**E**) Bacterial load in lung following *S. aureus* infection 21 days, 42 days, and 3 months post-vaccinations. (*n* = 14 unvaccinated mice, 6 for other groups). (**F**) Bacterial load in lung following *A. baumannii* infection 21 days post-vaccinations (*n* = 5 for each group). Each dot represents one mouse. Data are pooled from at least two independent experiments. Statistical significance of body weight in (B) was assessed by two-way ANOVA with Šidák's multiple-comparison test. Statistical significance in (E) was assessed by one-way ANOVA followed by Dunnett's multiple-comparison test for each timepoint compared with unvaccinated group. Statistical significance in (F) were assessed by two-tailed Mann-Whitney U test. Data are mean ± SEM ($^*P < 0.05$, $^{**}P < 0.01$, $^{***}P < 0.001$, $^{****}P < 0.0001$).

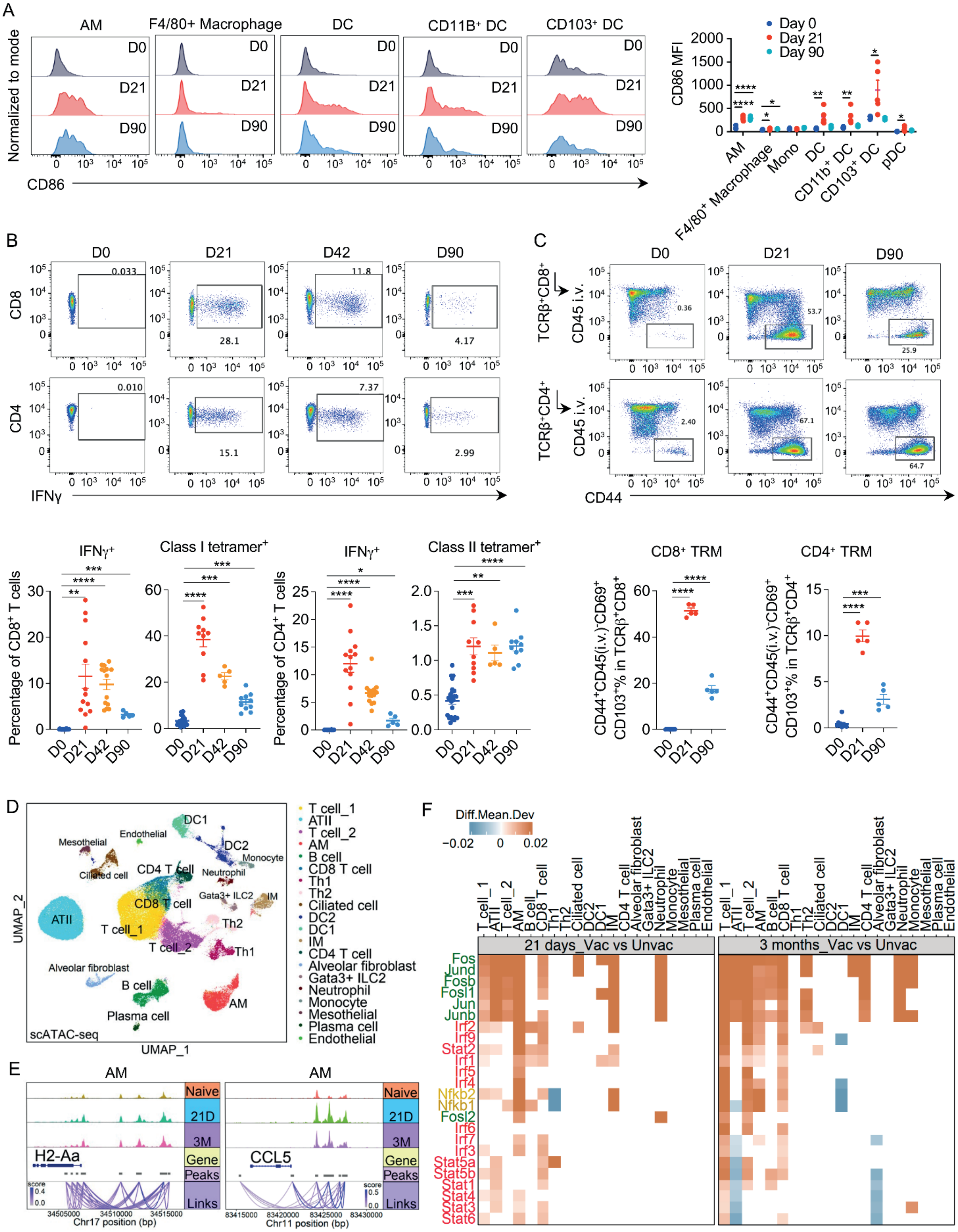
A
AM
F4/80+ Macrophage
DC
CD11B+ DC
CD103+ DC
D0
D21
D90
Normalized to mode
CD86
CD86 MFI
Day 0
Day 21
Day 90
AM
F4/80+ Macrophage
Mono
DC
CD11b+ DC
CD103+ DC
pDC
B
D0
D21
D42
D90
CD8
CD4
IFNγ
0.033
28.1
11.8
4.17
0.010
15.1
7.37
2.99
C
TCRβ+CD8+
TCRβ+CD4+
CD45 i.v.
CD44
0.36
53.7
25.9
2.40
67.1
64.7
IFNγ+
Class I tetramer+
Class II tetramer+
Percentage of CD8+ T cells
Percentage of CD4+ T cells
CD8+ TRM
CD4+ TRM
CD44+CD45(i.v.)−CD69+ CD103+% in TCRβ+CD8+
CD44+CD45(i.v.)−CD69+ CD103+% in TCRβ+CD4+
D
UMAP_1
UMAP_2
scATAC-seq
T cell_1
ATII
T cell_2
AM
B cell
CD8 T cell
Th1
Th2
Ciliated cell
DC2
DC1
IM
CD4 T cell
Alveolar fibroblast
Gata3+ ILC2
Neutrophil
Monocyte
Mesothelial
Plasma cell
Endothelial
E
AM
Naive
21D
3M
Gene
Peaks
Links
H2-Aa
CCL5
Chr17 position (bp)
Chr11 position (bp)
F
Diff.Mean.Dev
−0.02
0
0.02
21 days_Vac vs Unvac
3 months_Vac vs Unvac
Fos
Jund
Fosb
Fosl1
Jun
Junb
Irf2
Irf9
Stat2
Irf1
Irf5
Irf4
Nfkb2
Nfkb1
Fosl2
Irf6
Irf7
Irf3
Stat5a
Stat5b
Stat1
Stat4
Stat3
Stat6

Fig. 2. Intranasal GLA-3M-052-LS + OVA vaccination elicits robust and durable antigen-specific TRM responses alongside innate immune activation, and drives coordinated epigenomic remodeling in alveolar macrophages and T cells. (**A**) (Left) Representative flow cytometry plots of CD86 expression in alveolar macrophage (AM), F4/80$^+$ Macrophage, Dendritic Cell (DC), CD11b$^+$ DC, and CD103$^+$ DC. (Right) Mean fluorescence intensity (MFI) of CD86 in indicated cell types at 21 and 90 days post-four immunizations. $n = 5$ for each group. Gating strategies can be found in fig. S123A. (**B**) (Top) Representative flow cytometry plots of OVA-specific IFNγ expression in CD4$^+$ or CD8$^+$ T cells. (Bottom) Frequencies of IFNγ$^+$CD8$^+$ T cells and OVA Class I tetramer$^+$ CD8$^+$ T cells among CD8$^+$ T cells, and IFNγ$^+$CD4$^+$ T cells and OVA Class II tetramer$^+$ CD4$^+$ T cells among CD4$^+$ T cells at 21, 42, and 90 days post-four immunizations. IFNγ$^+$ cells were quantified after overnight stimulation with 100 μg/ml OVA protein. ($n = 25, 13, 14, 5$ for day 0, day 21, day 42, and day 90 respectively, for IFNγ$^+$ data. $n = 25, 10, 5, 10$ for day 0, day 21, day 42, and day 90 respectively, for Tetramer$^+$ figures). (**C**) (Top) Representative flow cytometry plots of CD4$^+$ or CD8$^+$ CD45(*i.v.*)$^-$CD44$^+$ cells gated from TCRβ$^+$CD4/CD8$^+$ cells at day 0, day 21, and day 90 post-four immunizations. (Bottom) Frequencies of CD4$^+$/CD8$^+$ TRM (CD45$^+$TCRβ$^+$CD4$^+$/CD8$^+$CD45(*i.v.*)$^-$ CD44$^+$CD69$^+$CD103$^+$) in live CD45$^+$TCRβ$^+$CD4$^+$/CD8$^+$ populations. $n = 10, 5, 5$ for day 0, day 21, and day 90 respectively. The representative flow cytometry plots from 21 days after vaccinations is also shown in fig. S17D. Gating strategies can be found in fig. S17D. Each dot represents one mouse. Data in (A) are representative of at least two independent experiments. The CD86 MFI in indicated cell types at different times post-vaccinations are shown in fig. S6B. Data in (B) and (C) are pooled from at least two independent experiments. Significance in (A) to (C) was assessed by one-way ANOVA followed by Dunnett's multiple-comparison test for each timepoint compared with day 0. Data are mean ± SEM ($^*P < 0.05$, $^{**}P < 0.01$, $^{***}P < 0.001$, $^{****}P < 0.0001$). (**D**) UMAP projection of 96,834 total lung cells clustered from scATAC-seq data from naïve mice, and from mice at 21 and 90 days post-vaccinations. IM (Interstitial macrophage), ATII (Type II alveolar epithelial cells). (**E**) Tracks of H2-Aa and Ccl5 on chromosomes 17 and 11, respectively, in AMs from naïve mice, 21 days and 3-month post-immunized mice. Co-accessible peaks are shown as links below the tracks. (**F**) Heat map showing transcription factor (TF) different mean deviation scores at 21 days and 3 months post-vaccinations compared with naïve mice. AP-1 transcription factors are shown in green. Stat and Irf transcription factors are shown in red. Nfκb transcription factors are shown in yellow.

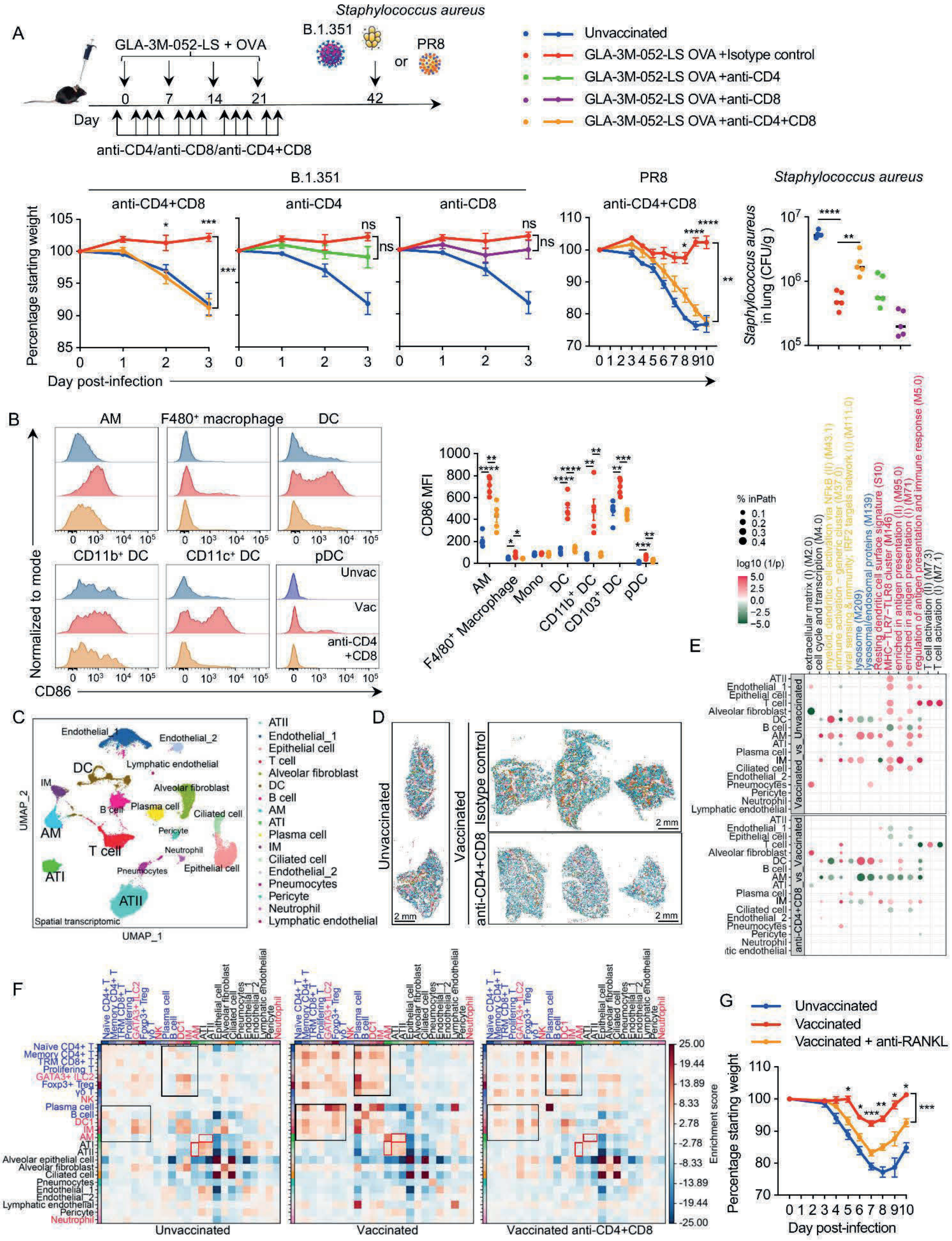
A
GLA-3M-052-LS + OVA
B.1.351
Staphylococcus aureus
or
PR8
0
7
14
21
42
Day
anti-CD4/anti-CD8/anti-CD4+CD8
Unvaccinated
GLA-3M-052-LS OVA +Isotype control
GLA-3M-052-LS OVA +anti-CD4
GLA-3M-052-LS OVA +anti-CD8
GLA-3M-052-LS OVA +anti-CD4+CD8
B.1.351
anti-CD4+CD8
anti-CD4
anti-CD8
PR8
anti-CD4+CD8
Staphylococcus aureus
Percentage starting weight
Day post-infection
Staphylococcus aureus in lung (CFU/g)
ns
B
AM
F480+ macrophage
DC
CD11b+ DC
CD11c+ DC
pDC
Unvac
Vac
anti-CD4 +CD8
Normalized to mode
CD86
CD86 MFI
AM
F4/80+ Macrophage
Mono
DC
CD11b+ DC
CD103+ DC
pDC
C
UMAP_1
UMAP_2
Spatial transcriptomic
ATII
Endothelial_1
Epithelial cell
T cell
Alveolar fibroblast
DC
B cell
AM
ATI
Plasma cell
IM
Ciliated cell
Endothelial_2
Pneumocytes
Pericyte
Neutrophil
Lymphatic endothelial
D
Unvaccinated
Vaccinated
Isotype control
anti-CD4+CD8
2 mm
E
% inPath
log10 (1/p)
Unvaccinated_vs_Vaccinated
anti-CD4+CD8_vs_Vaccinated
F
Unvaccinated
Vaccinated
Vaccinated anti-CD4+CD8
Enrichment score
G
Unvaccinated
Vaccinated
Vaccinated + anti-RANKL
Percentage starting weight
Day post-infection

Fig. 3. Antigen-specific T cells coordinate interactions among innate immune cells and lung epithelial cells. (**A**) (Top) Experimental design. (Bottom) Weight loss of unvaccinated, vaccinated, and vaccinated mice depleted of T cells, following challenge with SARS-CoV-2 ($n = 8$ unvaccinated mice, 5 vaccinated with isotype control treatment, 6 for other groups) or *S. aureus* ($n = 5$ for each group). 200 μg/dose CD4 and CD8 antibodies were used in this experiment. (**B**) (Left) Representative flow cytometry plots of CD86 expression in AM, F4/80$^+$ macrophage, DC, CD11b$^+$ DC, CD103$^+$ DC, and pDC. (Right) MFI of CD86 in indicated cell type of unvaccinated, vaccinated, and vaccinated mice depleted of CD4$^+$ and CD8$^+$ T cells, at 21 days post-4 immunizations. $n = 5$ for each group. Gating strategies can be found in fig. S123A. (**C**) UMAP projection of 53,645 total lung cells clustered from spatial transcriptomes of unvaccinated, vaccinated, and vaccinated mice depleted of CD4$^+$ and CD8$^+$ T cells at 21 days post-vaccinations. IM, interstitial macrophage. Anti-CD4 and CD8 antibodies were administered beginning with the first immunization. (**D**) Spatial mapping of scRNA-seq profiles, colored by cell type as in (C). Scale bar, 2 mm. (**E**) Blood transcriptional module (BTM) enrichment of differentially expressed genes (DEGs) from identified lung cell subsets in vaccinated versus unvaccinated mice (FDR < 0.05). Enrichment was performed using hypergeometric distribution with BH correction. Antigen-presentation-associated pathways are marked in red; lysosome and phagocytosis-associated pathways in blue; antiviral-immunity-associated pathways in yellow. (**F**) Heatmap showing the change between cell-cell communications among unvaccinated, vaccinated, and vaccinated mice depleted of CD4$^+$ and CD8$^+$ T cells at 21 days post-vaccinations. Colors represent the changes in communication strength, calculated from cellular spatial information and ligand-receptor interaction. Adaptive immune cells are marked in blue, innate immune cells in red, and structural cells in black. The black box highlights interactions between T cells and B cells, or T cells and innate cells, while the red box highlights interactions between AM and alveolar epithelial cells (ATI and ATII). Significance asterisks in (A) indicate comparisons between vaccinated + antibody-treated groups and vaccinated groups. Each dot represents one mouse. Data are representative of at least two independent experiments. Significance of body weight in (A) was assessed by two-way ANOVA with Šidák's multiple-comparison test. Other significance in (A) and (B) was assessed by one-way ANOVA followed by Dunnett's multiple-comparison test for each group compared with vaccinated group. Data are mean ± SEM (ns $P > 0.05$, $^*P < 0.05$, $^{**}P < 0.01$, $^{***}P < 0.001$, $^{****}P < 0.0001$).

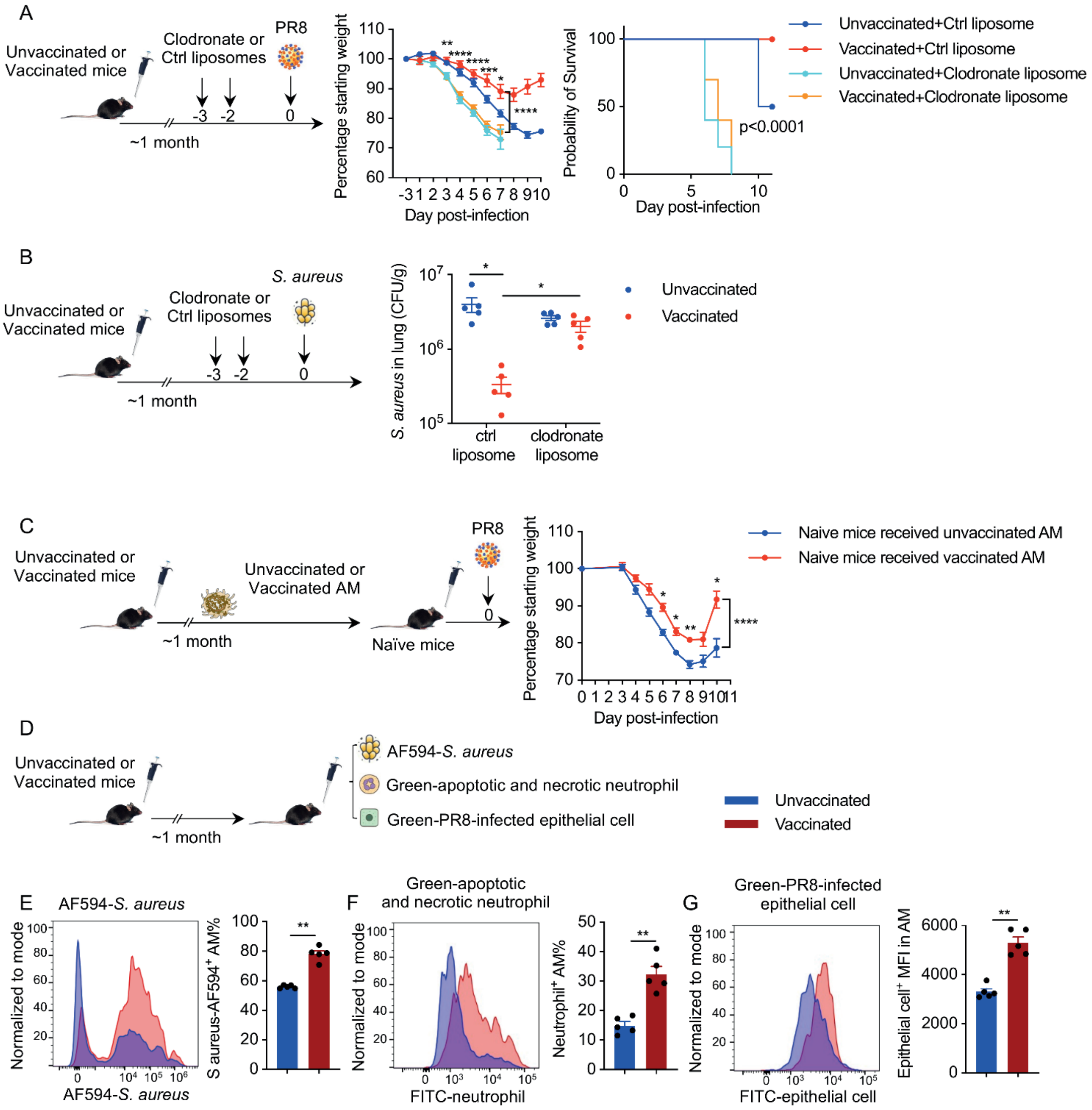
A
Unvaccinated or Vaccinated mice
Clodronate or Ctrl liposomes
PR8
-3
-2
0
~1 month
Percentage starting weight
Day post-infection
Probability of Survival
Day post-infection
p<0.0001
Unvaccinated+Ctrl liposome
Vaccinated+Ctrl liposome
Unvaccinated+Clodronate liposome
Vaccinated+Clodronate liposome
B
Unvaccinated or Vaccinated mice
Clodronate or Ctrl liposomes
S. aureus
-3
-2
0
~1 month
S. aureus in lung (CFU/g)
ctrl liposome
clodronate liposome
Unvaccinated
Vaccinated
C
Unvaccinated or Vaccinated mice
Unvaccinated or Vaccinated AM
PR8
~1 month
Naïve mice
0
Percentage starting weight
Day post-infection
Naive mice received unvaccinated AM
Naive mice received vaccinated AM
D
Unvaccinated or Vaccinated mice
~1 month
AF594-S. aureus
Green-apoptotic and necrotic neutrophil
Green-PR8-infected epithelial cell
Unvaccinated
Vaccinated
E
AF594-S. aureus
Normalized to mode
AF594-S. aureus
S aureus-AF594⁺ AM%
F
Green-apoptotic and necrotic neutrophil
Normalized to mode
FITC-neutrophil
Neutrophil⁺ AM%
G
Green-PR8-infected epithelial cell
Normalized to mode
FITC-epithelial cell
Epithelial cell⁺ MFI in AM

Fig. 4. Enhanced phagocytic function of AMs following vaccination contributes to the vaccine-induced non-specific protective immunity. (A) (Left) Experimental design. (Right) Bacterial load, 1 day after *S. aureus* (*S. aureus*) infection, in the lungs of vaccinated and unvaccinated mice treated with ctrl or clodronate liposomes. *n* = 5 for each group. (**B**) Experimental design schematic for (**C** to **E**). AMs were collected 30 min after infection in vivo. In (C) to (E), blue color represents unvaccinated mice and red color represents vaccinated mice. (C) (Left) Representative flow cytometry histogram showing uptake of AF594-labeled *S. aureus* by AMs. (Right) Frequency of AF594-labeled *S. aureus*$^+$ AMs among total AMs in BAL. Gating strategies can be found in fig. S123A. (D) (Left) Representative flow cytometry histogram showing uptake of green-labeled apoptotic and necrotic neutrophils by AMs. (Right) Frequency of green-labeled neutrophil$^+$ AMs among total AMs in BAL. (E) (Left) Representative flow cytometry histogram showing uptake of green-labeled PR8 infected lung epithelial cells (A549) by AMs. (Right) MFI of green-labeled epithelial$^+$ AMs among total AMs in BAL. *n* = 5 for each group. Each dot represents one mouse. Data are representative of at least two independent experiments. Significance in (A) was assessed by two-way ANOVA with Šidák's multiple-comparison test, (C) to (E) were assessed by two-tailed Mann-Whitney U test. Data are mean ± SEM ($*P < 0.05$, $**P < 0.01$).

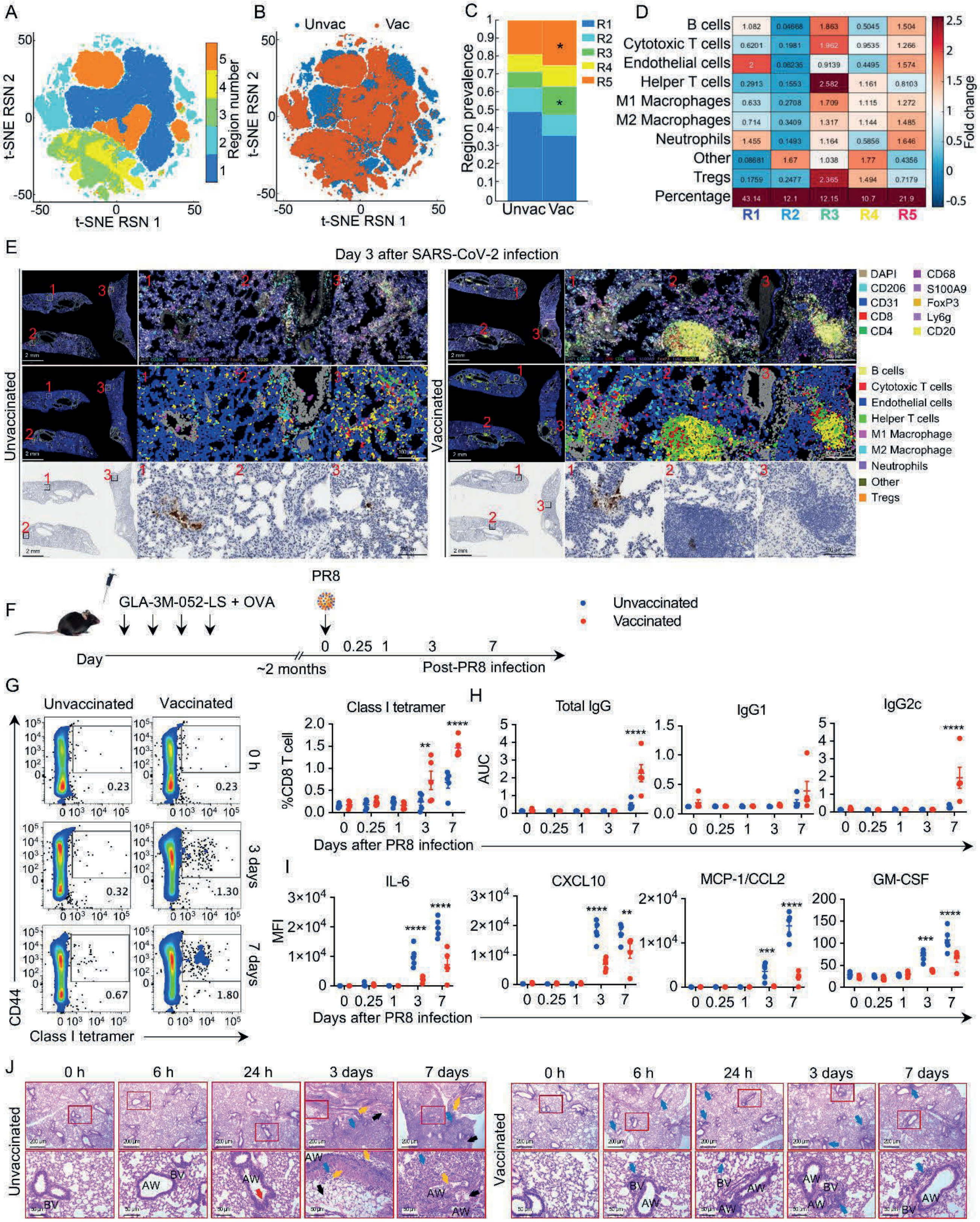
A
t-SNE RSN 2
t-SNE RSN 1
Region number
1
2
3
4
5
B
Unvac
Vac
t-SNE RSN 2
t-SNE RSN 1
C
Region prevalence
Unvac
Vac
R1
R2
R3
R4
R5
*
*
D
B cells 1.082 0.04668 1.863 0.5045 1.504
Cytotoxic T cells 0.6201 0.1981 1.962 0.9535 1.266
Endothelial cells 2 0.08236 0.9139 0.4495 1.574
Helper T cells 0.2913 0.1553 2.582 1.161 0.8103
M1 Macrophages 0.633 0.2708 1.709 1.115 1.272
M2 Macrophages 0.714 0.3409 1.317 1.144 1.485
Neutrophils 1.455 0.1493 1.164 0.5856 1.646
Other 0.08681 1.67 1.038 1.77 0.4356
Tregs 0.1759 0.2477 2.365 1.494 0.7179
Percentage 43.14 12.1 12.15 10.7 21.9
R1
R2
R3
R4
R5
Fold change
E
Day 3 after SARS-CoV-2 infection
Unvaccinated
Vaccinated
DAPI
CD206
CD31
CD8
CD4
CD68
S100A9
FoxP3
Ly6g
CD20
B cells
Cytotoxic T cells
Endothelial cells
Helper T cells
M1 Macrophage
M2 Macrophage
Neutrophils
Other
Tregs
2 mm
F
GLA-3M-052-LS + OVA
PR8
Day
~2 months
0 0.25 1 3 7
Post-PR8 infection
Unvaccinated
Vaccinated
G
Unvaccinated
Vaccinated
0 h
3 days
7 days
0.23
0.23
0.32
1.30
0.67
1.80
CD44
Class I tetramer
Class I tetramer
%CD8 T cell
Days after PR8 infection
**
****
H
Total IgG
IgG1
IgG2c
AUC
****
****
I
IL-6
CXCL10
MCP-1/CCL2
GM-CSF
MFI
Days after PR8 infection
****
****
****
**
***
****
***
****
J
0 h
6 h
24 h
3 days
7 days
Unvaccinated
Vaccinated
AW
BV

Fig. 5. Vaccination promotes rapid formation of tertiary lymphoid structures and regulated inflammation following infection. (**A**) Multiplexed spatial protein imaging was performed using the PhenoCycler-Fusion (PCF; updated CODEX platform). t-SNE plot showing spatial clustering of regions from unvaccinated and vaccinated mice (one-month post-vaccinations) at day 3 following SARS-CoV-2 infection, based on region-specific neighborhood (RSN) features. Each dot represents a cell, color-coded by region number (1 to 5). $n = 12$ lung sections, including six slides from three unvaccinated mice and six slides from three vaccinated mice. (**B**) t-SNE plot showing the distribution of vaccinated (red) and unvaccinated (blue) samples across RSN-defined spatial regions. (**C**) Bar plot illustrating the composition of regions 1 to 5 in vaccinated and unvaccinated mice, based on spatial clustering analysis. Asterisks denote the regions with increased proportions in vaccinated mice compared with unvaccinated mice following challenge with SARS-CoV-2. (**D**) Heat map showing the cellular composition within each region and the relative frequencies of regions 1 to 5 in all samples. Colors indicate fold-change values (red, up-regulated; blue, down-regulated), with fold-change values indicated directly. (**E**) (Top) Representative images of CD206, CD31, CD8, CD4, CD68, S100A9, Foxp3, Ly6G, CD20, and DAPI. Inserts below showing images of different cell types. (Bottom) Immunohistochemical staining images about SARS-CoV-2 N protein localization on adjacent tissue sections. Scale bar: left, 2 mm; right, 160 μm. (**F**) Experimental design. (**G**) (Left) Representative flow-cytometry plots of NP class I tetramer$^+$ CD3$^+$CD8$^+$CD44$^+$ T cells gated from CD3$^+$CD8$^+$ T cells in lungs of vaccinated and unvaccinated mice at indicated times after PR8 infection. (Right) Frequency of NP Class I tetramer$^+$ CD8$^+$ cells in CD8$^+$ T cells at indicated time after PR8 infection. (**H**) Levels of HA-specific total IgG, IgG1, and IgG2c in BAL fluid. (I) Levels of IL-6, CXCL10, MCP-1/CCL2, and GM-CSF in BAL fluid. (J) Representative H&E-stained lung sections from mice unvaccinated and vaccinated at 0, 6 hours, 24 hours, 3 days, and 7 days after PR8 infection. Blue arrows indicate immune cell infiltrates; red arrows indicate virus infected epithelial cells; yellow arrows indicate alveolar wall thickening and epithelial cell damage; black arrows indicate hyaline membrane formation. AW, airway; BV, blood vessel. Scale bar: top, 200 μm; bottom, 50 μm. $n = 5$ for all groups. Each dot represents one mouse. Data are representative of at least two independent experiments. Significance in (G) to (I) was assessed by two-way ANOVA with Šidák's multiple-comparison test. Data are mean ± SEM (**$P < 0.01$, ***$P < 0.001$, ****$P < 0.0001$).

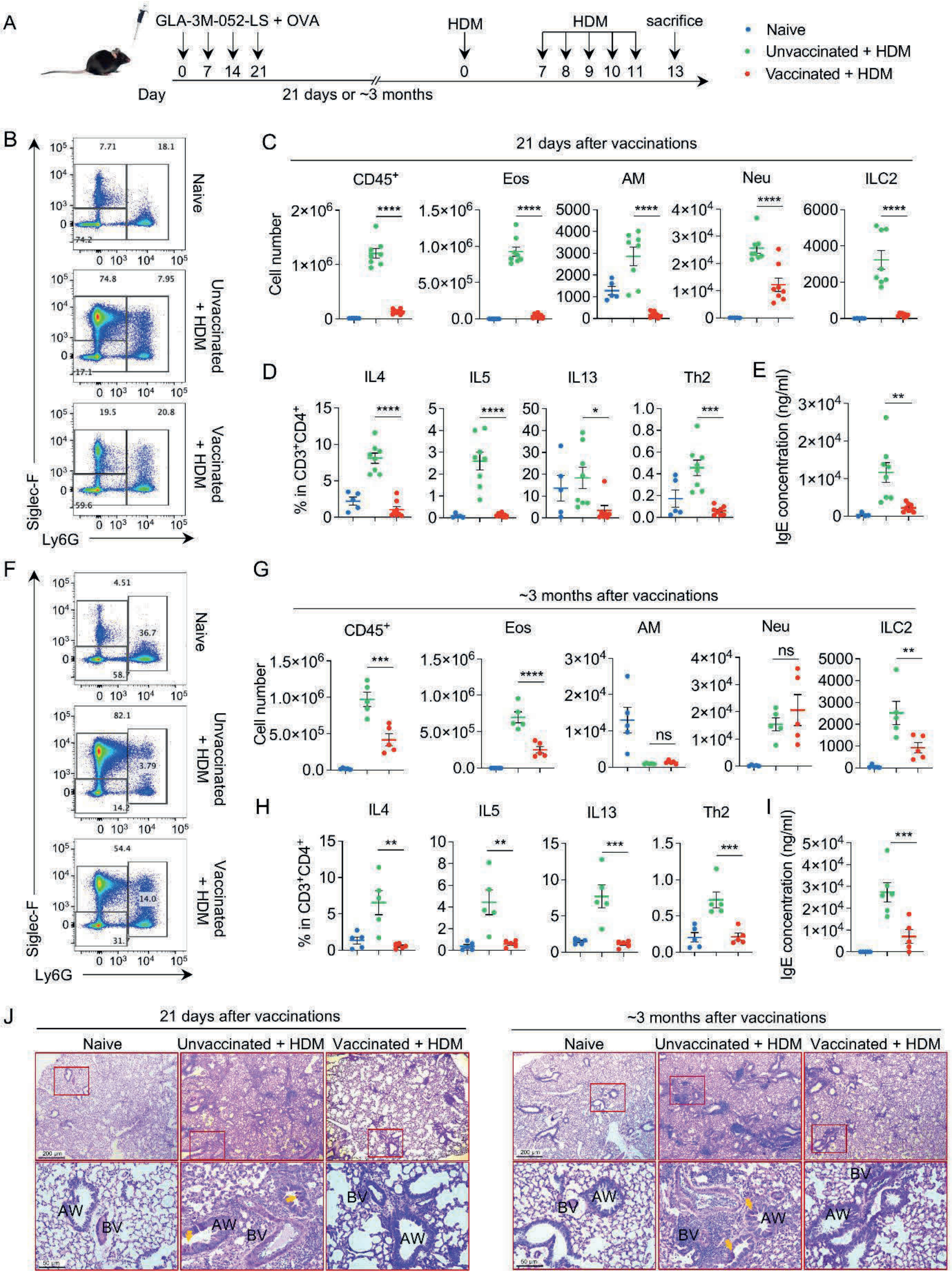
A
GLA-3M-052-LS + OVA
HDM
HDM
sacrifice
0 7 14 21
0
7 8 9 10 11
13
Day
21 days or ~3 months
Naive
Unvaccinated + HDM
Vaccinated + HDM
B
Siglec-F
Ly6G
Naive
Unvaccinated + HDM
Vaccinated + HDM
7.71
18.1
74.2
74.8
7.95
17.1
19.5
20.8
59.6
C
21 days after vaccinations
Cell number
CD45+
Eos
AM
Neu
ILC2
****
D
% in CD3+CD4+
IL4
IL5
IL13
Th2
****
*
***
E
IgE concentration (ng/ml)
**
F
Siglec-F
Ly6G
Naive
Unvaccinated + HDM
Vaccinated + HDM
4.51
36.7
58.7
82.1
3.79
14.2
54.4
14.0
31.1
G
~3 months after vaccinations
Cell number
CD45+
Eos
AM
Neu
ILC2
***
****
ns
**
H
% in CD3+CD4+
IL4
IL5
IL13
Th2
**
***
I
IgE concentration (ng/ml)
***
J
21 days after vaccinations
~3 months after vaccinations
Naive
Unvaccinated + HDM
Vaccinated + HDM
AW
BV
200 μm
50 μm

Fig. 6. Intranasal GLA-3M-052-LS + OVA vaccination confers robust and long-lasting protection against allergic asthma. (**A**) Experimental design. Representative flow cytometry plot of Ly6G$^-$Siglec-F$^+$ Eosinophils (Eos) gated from CD11b$^+$ cells in the indicated groups of (**B**) 21 days or (**F**) 3 months after vaccinations. Gating strategies can be found in fig. S123A. Cell number of CD45$^+$ cells, Eos, AM, neutrophil (Neu), and ILC2 cells in the BAL of mice (**C**) 21 days or (**G**) 3 months after vaccinations. The frequency of IL4$^+$, IL5$^+$, IL13$^+$, and Th2 cells (GATA3$^+$) in CD4$^+$ T cells in the lungs of mice (**D**) 21 days or (H) 3 months after vaccinations. Serum IgE concentrations in mice (**E**) 21 days or (**I**) 3 months after vaccinations. (**J**) Representative Periodic Acid–Schiff (PAS)- stained image from the indicated groups at (left) 21 days and (right) 3 months after vaccinations. Scale bar, top, 200 μm; bottom, 50 μm. Yellow arrows highlight representative mucus accumulation in the airways, visualized as magenta-stained regions. *n* = 5, 8, 8, in 21 days after vaccinations and *n* = 5, 5, 5, in 3 months after vaccinations for naïve, unvaccinated and HDM challenge, GLA-3M-052-LS + OVA vaccinated and HDM challenge groups, respectively. Each dot represents one mouse. Data are representative of at least two independent experiments. Significance was assessed by one-way ANOVA with Šidák's multiple-comparison test. Only the significance between unvaccinated + HDM and vaccinated + HDM groups is shown. Data are mean ± SEM (ns $P > 0.05$, *$P < 0.05$, **$P < 0.01$, ***$P < 0.001$, ****$P < 0.0001$).

Mucosal vaccination in mice provides protection from diverse respiratory threats

Haibo Zhang, Katharine Floyd, Zhuoqing Fang, Filipe Araujo Hoffmann, Audrey Lee, Heather Marie Froggatt, Gurpreet Bharj, Xia Xie, Haleigh B. Eppler, Jordan Mariah Santagata, Yanli Wang, Mengyun Hu, Christopher B. Fox, Prabhu S. Arunachalam, Ralph Baric, Mehul S. Suthar, and Bali Pulendran

Science **Ahead of Print** DOI: 10.1126/science.aea1260

Science (ISSN 1095-9203) is published by the American Association for the Advancement of Science. 1200 New York Avenue NW, Washington, DC 20005. The title *Science* is a registered trademark of AAAS.

Science

AAAS

Supplementary Materials for

Mucosal vaccination in mice provides protection from diverse respiratory threats

Haibo Zhang, Katharine Floyd, Zhuoqing Fang, Filipe Araujo Hoffmann, Audrey Lee, Heather Marie Froggatt, Gurpreet Bharj, Xia Xie, Haleigh B. Eppler, Jordan Mariah Santagata, Yanli Wang, Mengyun Hu, Christopher B. Fox, Prabhu S. Arunachalam, Ralph Baric, Mehul S. Suthar, Bali Pulendran
Correspondence to: bpulend@stanford.edu

This PDF file includes:

Figs. S1 to S20
Tables S1 to S6

Fig. S1.

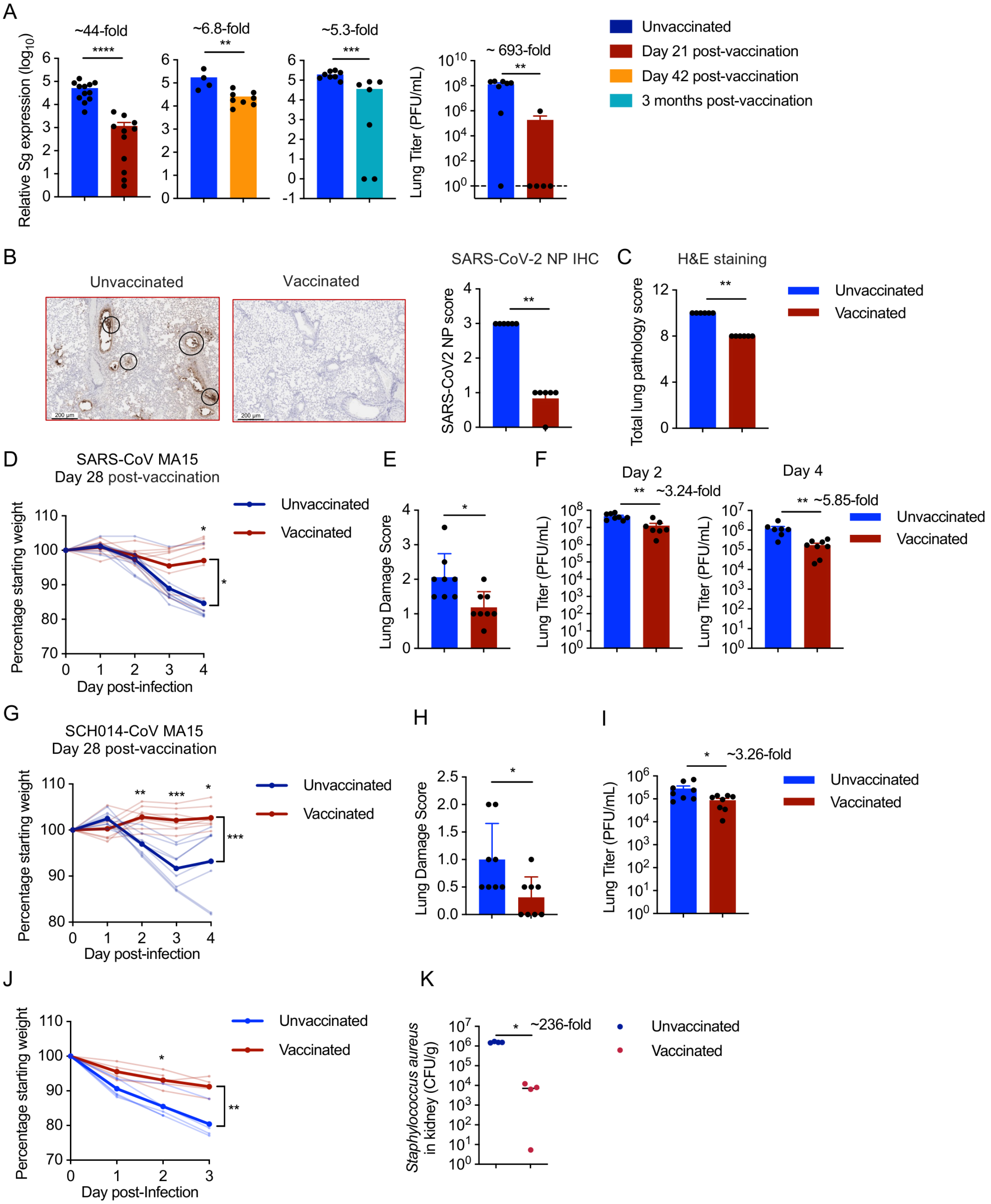

Fig. S1 Vaccination with GLA-3M-052-LS + OVA protects against SARS-CoV-2, SARS-CoV MA15, SCH014-CoV MA15, and *S. aureus* infections. (A) SARS-CoV-2 subgenomic (Sg) gene expression in lungs 21 days ($n = 12$ unvaccinated mice, 11 vaccinated mice), 42 days ($n = 4$ unvaccinated mice, 8 vaccinated mice), and 3 months ($n = 8$ unvaccinated mice, 7 vaccinated mice) post-vaccinations. Virus load in lung measured by plaque assay 21 days post-vaccinations (*n* = 8 unvaccinated and 5 vaccinated mice). (B) Left: Representative immunohistochemical (IHC) staining images of SARS-CoV-2 nucleocapsid protein in vaccinated and unvaccinated mice at day 3 after SARS-CoV-2 infection. Scale bar, 200 µm. Circles indicate SARS-CoV-2 nucleocapsid protein positive areas. Right: IHC score at day 3 after SARS-CoV-2 infection (*n* = 6 for each group). (C) H&E staining score at day 3 after SARS-CoV-2 infection (n = 6 for each group). (D) Body weight changes following SARS-CoV MA15 infection 28 days post-vaccinations. (E) Lung damage score at day 4 after SARS-CoV MA15 infection. (F) Virus load in lung measured by plaque assay at day 2 and day 4 after SARS-CoV MA15 infection. (G) Body weight changes following SCH014-CoV MA15 infection 28 days post-vaccinations. (H) Lung damage score at day 4 after SCH014-CoV MA15 infection. (I) Virus load in lung measured by plaque assay at day 4 after SCH014-CoV MA15 infection. *n* = 8 for each group in (D, E, G to I), *n* = 8 unvaccinated and 7 vaccinated mice in Day 2, *n* = 7 unvaccinated and 8 vaccinated mice in Day 4 in (F). (J) Body weight changes following *S. aureus* systemic infection one-month post-vaccinations. *n* = 5 for each group. (K) Bacterial load in kidneys at day 3 after *S. aureus* systemic infection. *n* = 4 for each group. Each dot represents one mouse. Data are representative of at least two independent experiments. Significance of weight loss in (D, G, J) were assessed by two-way ANOVA with Šidák's multiple-comparison test. Others were assessed by two-tailed Mann-Whitney U test. Data are mean ± SEM (*P < 0.05, **P < 0.01, ***P < 0.001, ****P < 0.0001).

Fig. S2.

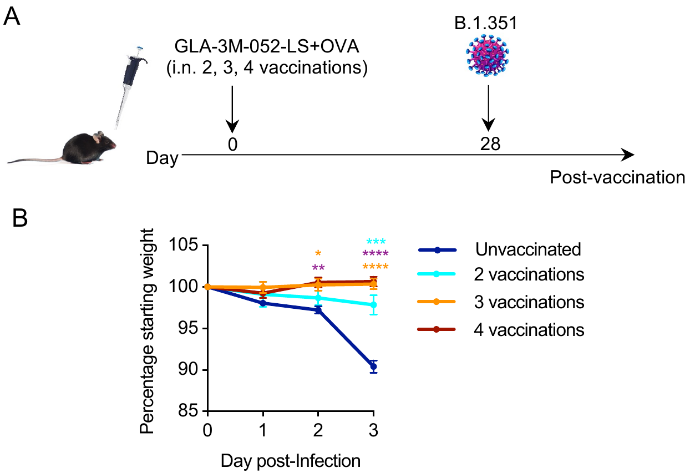

Fig. S2 SARS-CoV-2 infection following two, three, or four intranasal doses of GLA-3M-052-LS + OVA. (A) Experimental design. (B) Body weight changes following SARS-CoV-2 infection 28 days post-vaccinations. *n* = 9, 8, 8, 8 mice for unvaccinated, 4 immunizations, 3 immunizations, and 2 immunizations groups. Colored asterisks indicate statistical significance compared to the unvaccinated group for the corresponding color-coded group. Data are representative of at least two independent experiments. Significance was assessed by two-way ANOVA with Dunnett's multiple-comparison test. Data are mean ± SEM (*$P < 0.05$, **$P < 0.01$, ***$P < 0.001$, ****$P < 0.0001$).

Fig. S3.

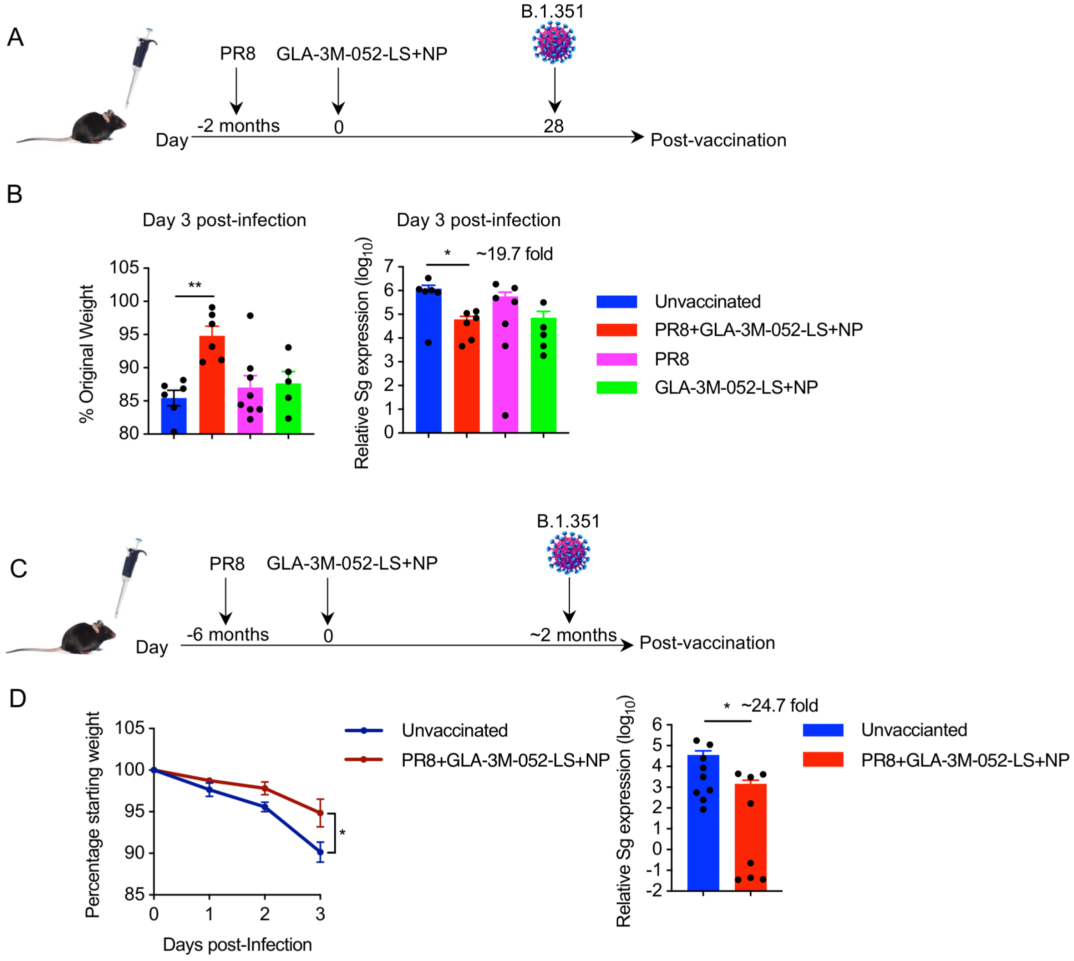

Fig. S3 A single GLA-3M-052-LS + NP vaccination following PR8 infection protects against SARS-CoV-2 infection. (A) Experimental design. (B) Left: Body weight changes following SARS-CoV-2 infection 28 days post-vaccinations. Right: SARS-CoV-2 subgenomic (Sg) gene expression in lungs. *n* = 6, 6, 7, 5 mice for unvaccinated, GLA-3M-052-LS + NP vaccinated following PR8 infection, only PR8 infected, and only GLA-3M-052-LS + NP vaccinated groups. (C) Experimental design schematic for (D). (D) Left: Body weight changes following SARS-CoV-2 infection 2 months post-vaccinations. Right: SARS-CoV-2 subgenomic (Sg) gene expression in lungs. *n* = 9 unvaccinated mice, 8 mice for GLA-3M-052-LS + NP vaccination following PR8 infection. Each dot represents one mouse. Data are representative of at least two independent experiments. Significance was assessed by one-way ANOVA followed by Dunnett's multiple-comparison test for each group compared with unvaccinated group in (B), two-way ANOVA with Šidák's multiple-comparison test in (D, left), two-tailed Mann-Whitney U test in (D, right), Data are mean ± SEM ($^{*}P < 0.05$, $^{**}P < 0.01$).

Fig. S4.

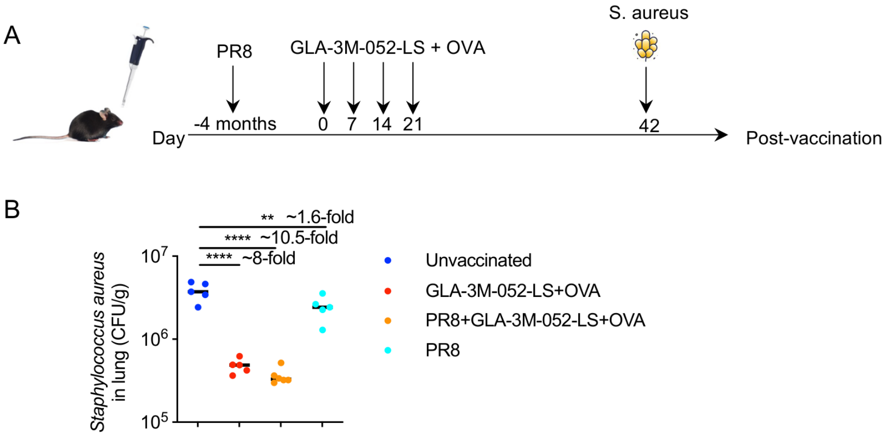

Fig. S4 GLA-3M-052-LS + OVA vaccination protects against *S. aureus* infection in PR8 infected non-naïve mice. (A) Experimental design. (B) Bacterial load in the lung at day 1 after infection. $n = 6$ for PR8 infected and GLA-3M-052-LS+OVA vaccinated mice, 5 for other groups. Each dot represents one mouse. Data are representative of at least two independent experiments. Significance was assessed by one-way ANOVA followed by Dunnett's multiple-comparison test for each group compared with unvaccinated group. Data are mean ± SEM (**$P < 0.01$, ****$P < 0.0001$).

Fig. S5.

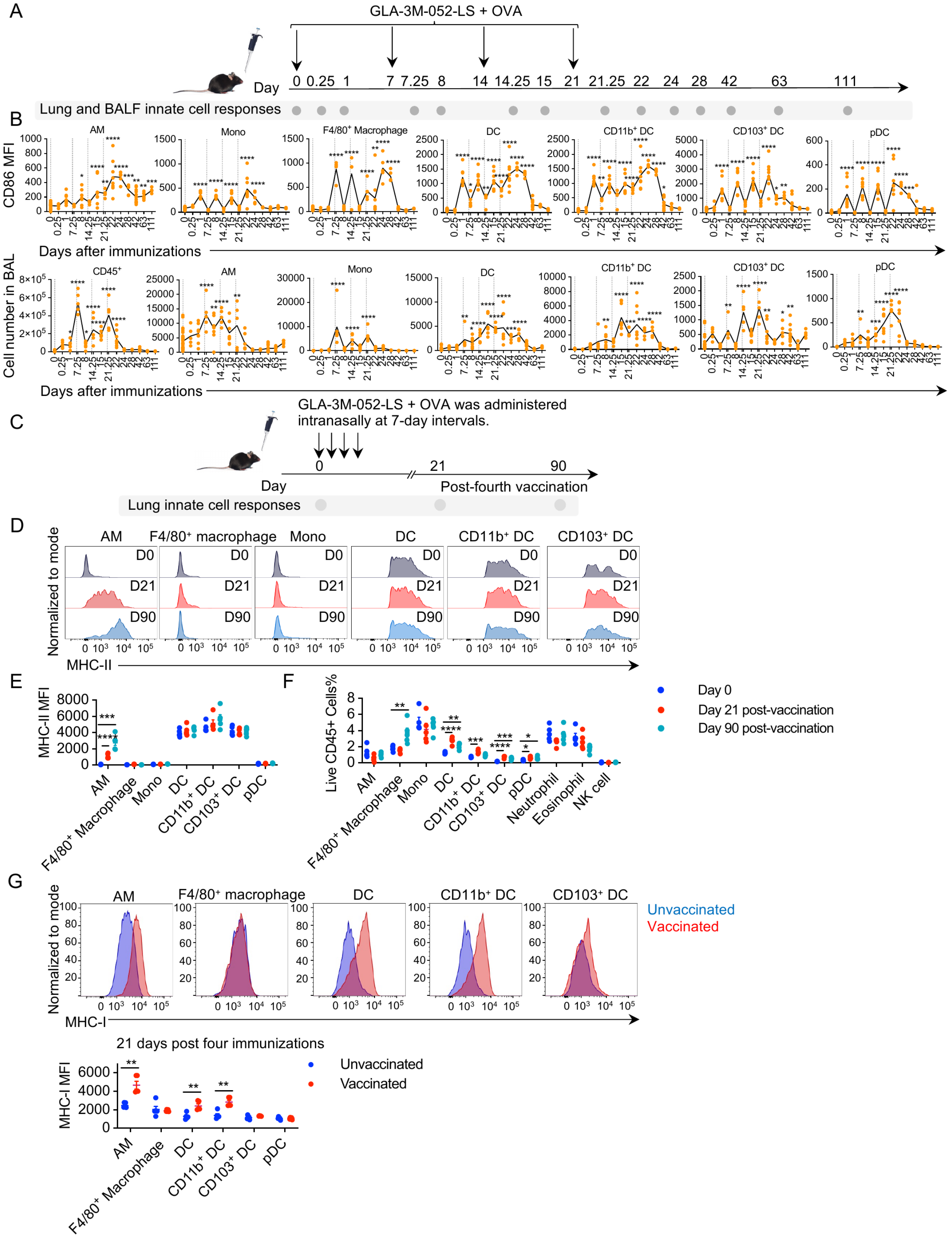
A
GLA-3M-052-LS + OVA
Day
0 0.25 1 7 7.25 8 14 14.25 15 21 21.25 22 24 28 42 63 111
Lung and BALF innate cell responses
B
CD86 MFI
AM
Mono
F4/80+ Macrophage
DC
CD11b+ DC
CD103+ DC
pDC
Days after immunizations
Cell number in BAL
CD45+
AM
Mono
DC
CD11b+ DC
CD103+ DC
pDC
Days after immunizations
C
GLA-3M-052-LS + OVA was administered intranasally at 7-day intervals.
Day
0
21
90
Post-fourth vaccination
Lung innate cell responses
D
Normalized to mode
AM
F4/80+ macrophage
Mono
DC
CD11b+ DC
CD103+ DC
D0
D21
D90
MHC-II
E
MHC-II MFI
AM
F4/80+ Macrophage
Mono
DC
CD11b+ DC
CD103+ DC
pDC
F
Live CD45+ Cells%
AM
F4/80+ Macrophage
Mono
DC
CD11b+ DC
CD103+ DC
pDC
Neutrophil
Eosinophil
NK cell
Day 0
Day 21 post-vaccination
Day 90 post-vaccination
G
Normalized to mode
AM
F4/80+ macrophage
DC
CD11b+ DC
CD103+ DC
Unvaccinated
Vaccinated
MHC-I
21 days post four immunizations
MHC-I MFI
Unvaccinated
Vaccinated
AM
F4/80+ Macrophage
DC
CD11b+ DC
CD103+ DC
pDC

Fig. S5 Innate cell responses in BAL and lung following four vaccinations with GLA-3M-052-LS + OVA. (A) Experimental design schematic for (B). (B) Top: CD86 MFI of indicated cell types in lung. *n* = 28 naïve mice, 5 mice for 6 hours post-each immunization, 8 mice for 24 hours post-each immunization, 5 mice for day 24 and day 28, 13 mice for day 42, 8 mice for day 63, 5 mice for day 111. Gray dashed lines indicate the 1st to 4th immunization time points, respectively. Bottom: Cell number in BAL. *n* = 28 naïve mice, 5 mice for 6 hours post-each immunization, 8 mice for 24 hours post-each immunization, 5 mice for day 24 and day 28, 12 mice for day 42, 7 mice for day 63, 5 mice for day 111. (C) Experimental design schematic for (D to F). (D) Representative flow cytometry plots of MHC-II expression in AM, F4/80+ macrophage, Monocyte (Mono), DC, CD11b+ DC, and CD103+ DC. (E) MHC-II MFI of indicated cell types in lung at 21 days or 90 days after immunizations. (F) Indicated cell type percentage in live CD45+ cell 21 days and 90 days post-four vaccinations. (G) Top: Representative flow cytometry plots of MHC-I expression in AM, F4/80+ macrophage, DC, CD11b+ DC, and CD103+ DC at day 28 post four immunizations. Bottom: MHC-I MFI of indicated cell types in lung. Gating strategies can be found in Fig. S23A. Each dot represents one mouse. Data in (B) are pooled from at least two independent experiments. Data in (D to G) are representative of at least two independent experiments. Significance in (B, E, F) were assessed by one-way ANOVA followed by Dunnett's multiple-comparison test for each time point compared with day 0. Significance in (G) was assessed by multiple Mann–Whitney (two-tailed) U-test. Data are mean ± SEM (*$P < 0.05$, **$P < 0.01$, ***$P < 0.001$, ****$P < 0.0001$).

Fig. S6.

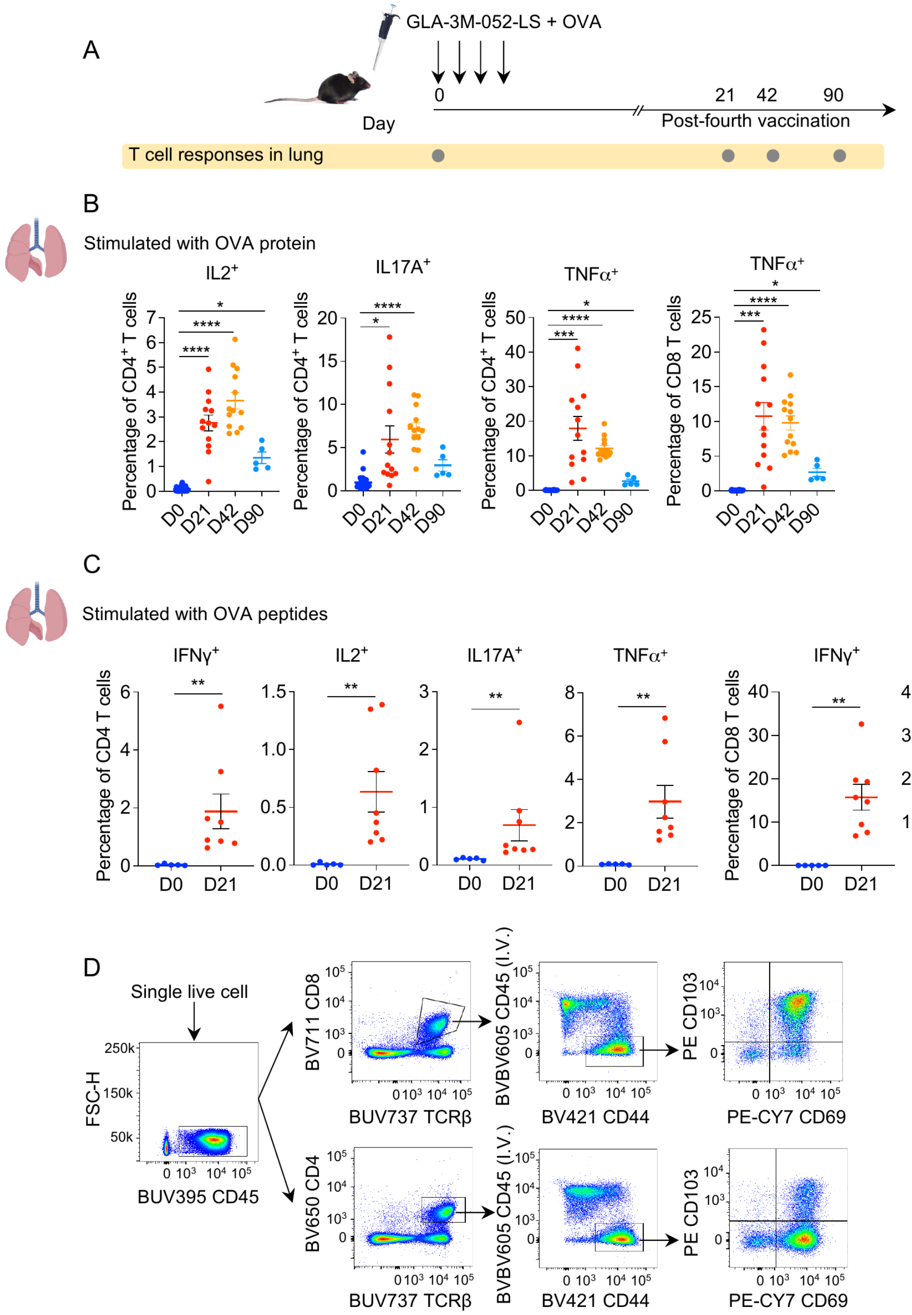

Fig. S6 OVA-specific T cell responses in lung post four vaccinations with GLA-3M-052-LS + OVA. (A) Experimental design. (B) IL2^{+}/IL17A^{+}/TNFα^{+} CD4^{+} T cells percentage in CD4^{+} T cells and TNFα^{+} CD8^{+} T cells percentage in CD8^{+} T cells at 21, 42, and 90 days post-four immunizations (after stimulation with 100 µg/ml OVA protein overnight *in vitro*). Data are pooled from at least two independent experiments, $n = 25, 13, 14, 5$ mice for day 0, day 21, day 42, and day 90, respectively. (C) IFNγ^{+}/IL2^{+}/IL17A^{+}/TNFα^{+} CD4^{+} T cells percentage in CD4^{+} T cells and IFNγ^{+}/TNFα^{+} CD8^{+} T cells percentage in CD8^{+} T cells at 21 days post-four immunizations (after stimulated with OVA peptides 6 hours *in vitro*) in lung, $n = 5$ in day 0, 8 in day 21. (D) Flow cytometric gating strategy for classifying lung resident memory T cells (TRM) in lung for Figure 2C. The representative gating shown is from one sample collected 21 days after vaccination. Each dot represents one mouse. Data are pooled from at least two independent experiments. Significance in (B) was assessed by one-way ANOVA followed by Dunnett's multiple-comparison test for each time point compared with day 0. Significance in (C) was assessed by two-tailed Mann-Whitney U test. Data are mean ± SEM (*P < 0.05, **P < 0.01, ***P < 0.001, ****P < 0.0001).

Fig. S7.

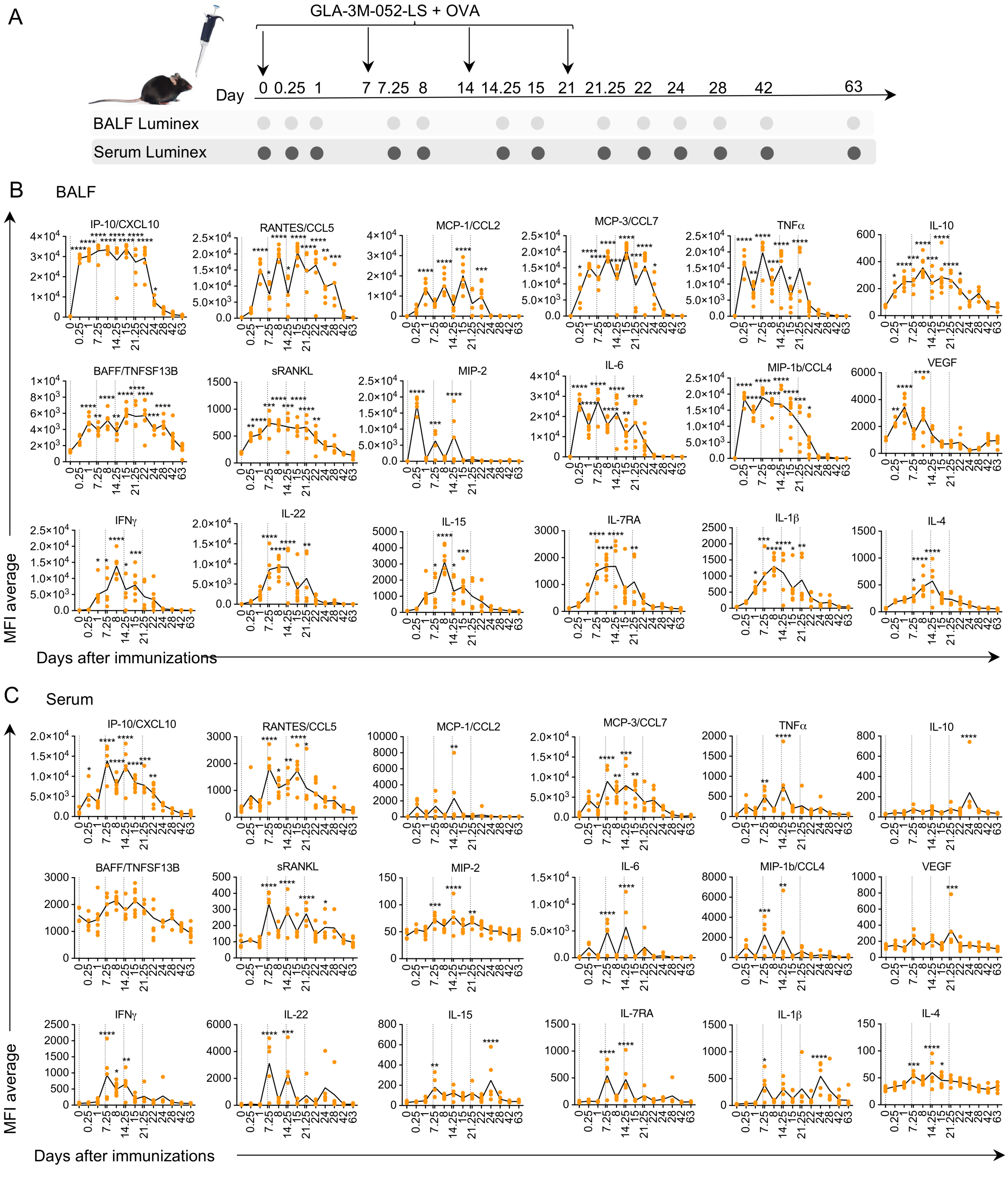

Fig. S7 Cytokines in BAL fluid and serum during and after immunizations with GLA-3M-052-LS + OVA. (A) Experimental design. (B) Average MFI of indicated cytokines in BALF and in (C) serum. *n* = 8 mice for 24 hours post-each immunization and day 42, 7 mice for Day 63, and 5 mice for other time points. Each dot represents one mouse. Data are pooled from at least two independent experiments. Significance was assessed by one-way ANOVA followed by Dunnett's multiple-comparison test for each time point compared with day 0. Data are mean ± SEM (*$P < 0.05$, **$P < 0.01$, ***$P < 0.001$, ****$P < 0.0001$).

Fig. S8.

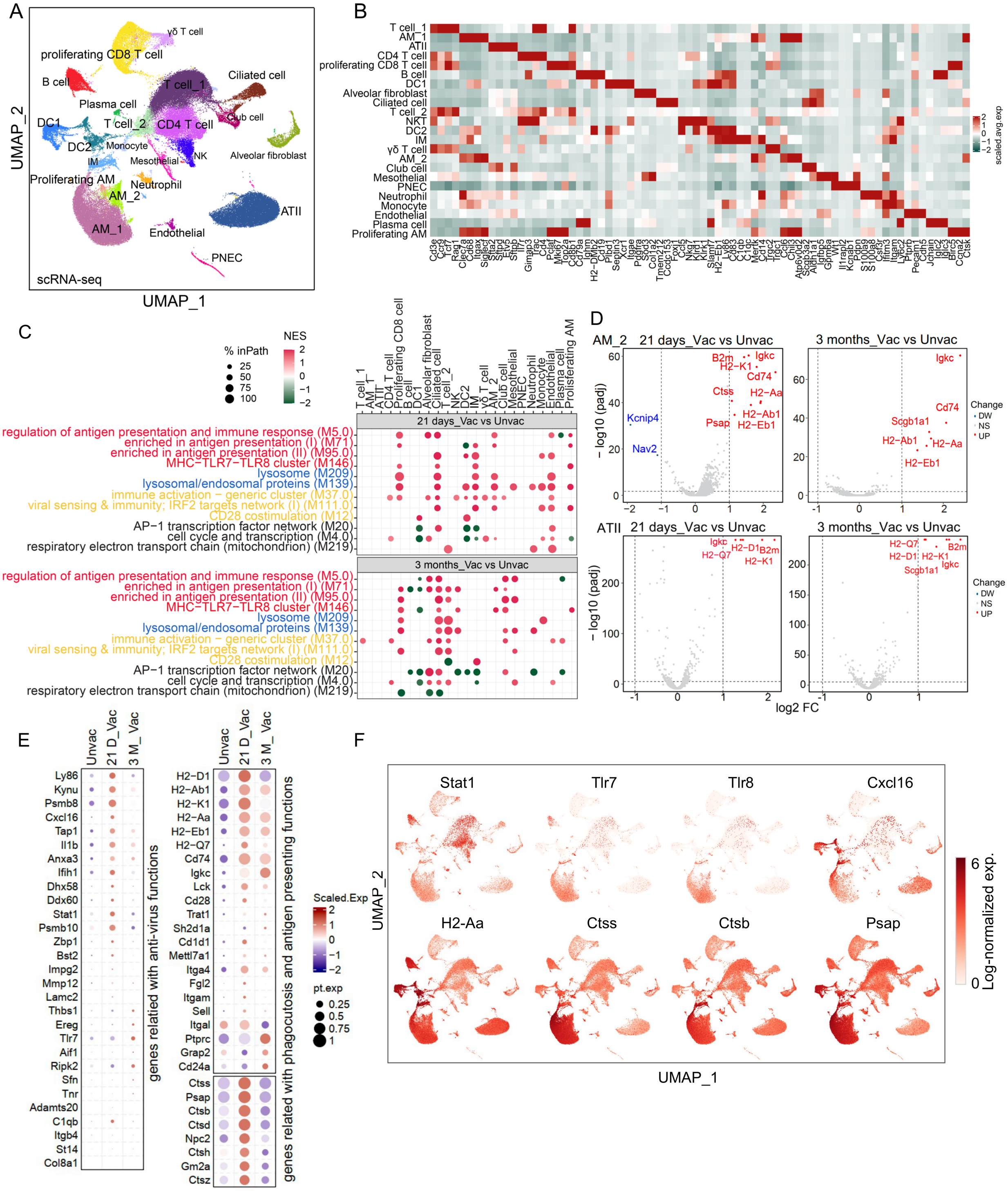

Fig. S8 Vaccinations with GLA-3M-052-LS + OVA promoted long-term activation of antigen presentation and antiviral immunity-related gene expression in AM and epithelial cells. (A) UMAP projection of 119,876 total lung cells clustered from scRNA-seq of naïve, 21 and 90 days post-immunization mice. IM, Interstitial macrophage. (B) Top variable genes defining cell clusters identified from scRNA-seq data. (C) Overrepresentation analysis and enrichment of Gene Ontology (GO) biological processes across identified cell clusters, using differentially expressed genes (DEGs; log2FC cutoff > 0.25; FDR cutoff < 0.05). Enrichment was performed using hypergeometric distribution with BH correction. (D) Volcano plots of DEGs logFC in ATII and AM_2 in 21 days post-vaccinations and 3 months post-vaccinations vs unvaccinated mice. (E) The bubble plot showing the expression changes of representative antiviral, antigen presentation, and phagocytosis-related differentially expressed genes at day 21 or 3 months following four vaccinations. (F) UMAP projection colored by scaled expression of markers.

Fig. S9.

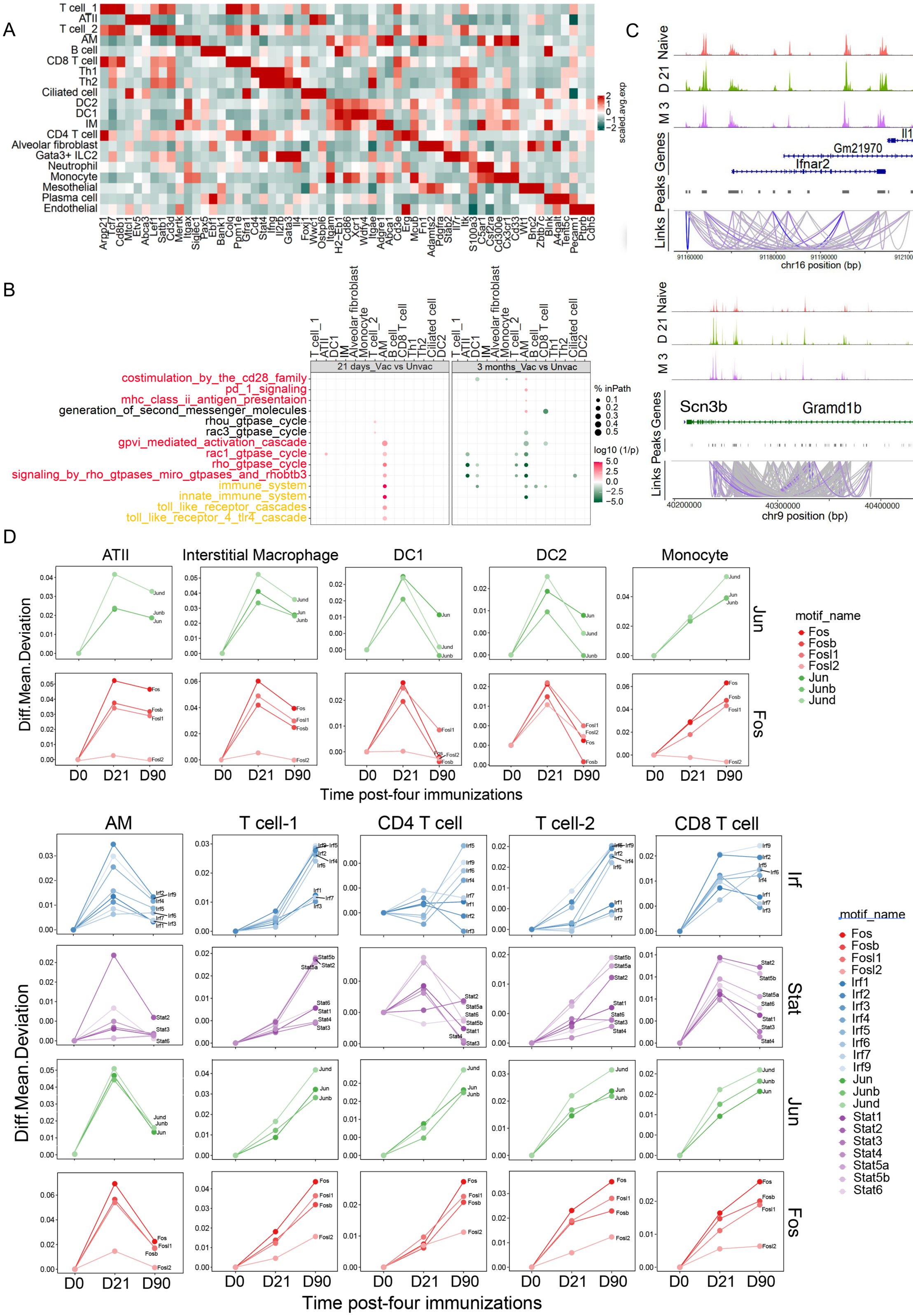
A
T cell_1
ATII
T cell_2
AM
B cell
CD8 T cell
Th1
Th2
Ciliated cell
DC2
DC1
IM
CD4 T cell
Alveolar fibroblast
Gata3+ ILC2
Neutrophil
Monocyte
Mesothelial
Plasma cell
Endothelial
scaled.avg.exp
Arpp21
Tcf7
Cd8b1
Mctp1
Etv5
Abca3
Lef1
Satb1
Cd3d
Mertk
Itgax
Siglecf
Pax5
Bank1
Colq
Ppm1e
Gfra1
Cd4
Stat4
Ifng
Il2rb
Gata3
Il4
Foxj1
Wdr5
Osbpl6
Itgam
H2-Eb1
Cd86
Xcr1
Wdfy4
Itgae
Adgre1
Apoe
Cd3e
Erg
Mcub
Fn1
Adamts2
Pdgfra
Stab2
Il7r
Itk
S100a3
C5ar1
Csf3r
Cd300e
Cx3cr1
Cd33
Wt1
Bnc2
Zbtb7c
Blnk
Aqp1
Tenc1
Pecam1
Ptprb
Cdh5
B
costimulation_by_the_cd28_family
pd_1_signaling
mhc_class_ii_antigen_presentaion
generation_of_second_messenger_molecules
rhou_gtpase_cycle
rac3_gtpase_cycle
gpvi_mediated_activation_cascade
rac1_gtpase_cycle
rho_gtpase_cycle
signaling_by_rho_gtpases_miro_gtpases_and_rhobtb3
immune_system
innate_immune_system
toll_like_receptor_cascades
toll_like_receptor_4_tlr4_cascade
21 days_Vac vs Unvac
3 months_Vac vs Unvac
% inPath
log10 (1/p)
C
Naive
D 21
M 3
Genes
Peaks
Links
Il10rb
Gm21970
Ifnar2
score
chr16 position (bp)
Scn3b
Gramd1b
chr9 position (bp)
D
ATII
Interstitial Macrophage
DC1
DC2
Monocyte
Diff.Mean.Deviation
Jun
Fos
motif_name
Time post-four immunizations
AM
T cell-1
CD4 T cell
T cell-2
CD8 T cell
Irf
Stat
D0
D21
D90

Fig. S9 scATAC-seq in the lung. (A) Top variable genes defining cell clusters identified from scATAC-seq data. (B) Overrepresentation analysis of biological processes across identified cell clusters, using differentially expressed genes (DEGs; log2FC cutoff > 0.25; FDR cutoff < 0.05). Enrichment was performed using hypergeometric test with BH correction. (C) Tracks of genes Gramd1b, Ifnar2, and Il10rb on Chromosome 9 and 16 in AM of naïve, 21 days and 3 months post-immunized mice. Peaks and links are shown below the track. (D) Line graph showing the differences in transcription factor (TF) accessibility 21 days and 3 months (D90) after four-vaccinations. Each line represents a separate TF within the indicated family.

Fig. S10.

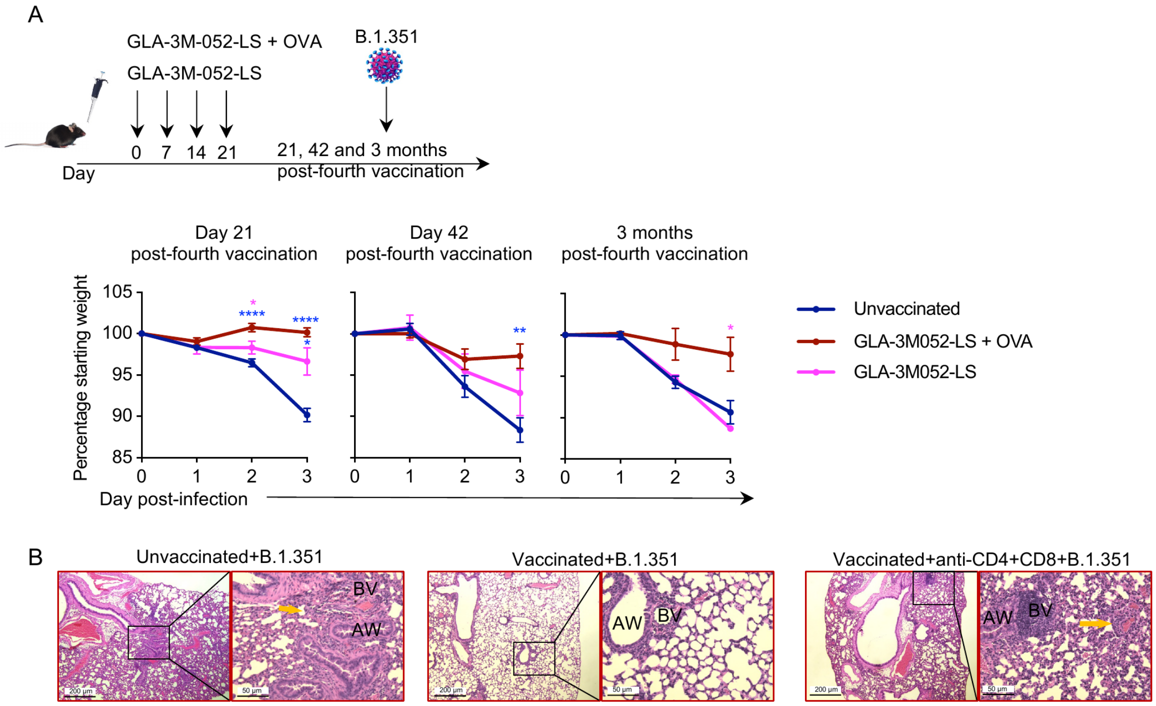

Fig. S10 Antigen-specific T-cell responses contribute to the protection against SARS-CoV-2 infection. (A) Top: experimental design. Bottom: Body weight changes of GLA-3M-052-LS with OVA or without OVA immunized mice 21 days (*n* = 14 unvaccinated mice, 16 GLA-3M-052-LS+OVA vaccinated mice, 8 GLA-3M-052-LS vaccinated mice), 42 days (*n* = 8 for each group), and 3 months (*n* = 10 unvaccinated mice, 5 GLA-3M-052-LS+OVA vaccinated mice, 7 GLA-3M-052-LS vaccinated mice) post-vaccinations, following SARS-CoV-2 infection. Colored asterisks indicate the significance of comparisons with the group of the corresponding color. (B) Representative H&E-stained lung sections from unvaccinated, vaccinated and vaccinated mice with T cell depletion at days 3 after SARS-CoV-2 infection. AW: airway, BV: blood vessel. Yellow arrows indicate alveolar structural damage and inflammation. Scale bar: left, 200 µm; right 50 µm. Data are pooled from at least two independent experiments. Significance was assessed by two-way ANOVA with Tukey's multiple-comparison test. Data are mean ± SEM (*P < 0.05, **P < 0.01, ****P < 0.0001).

Fig. S11.

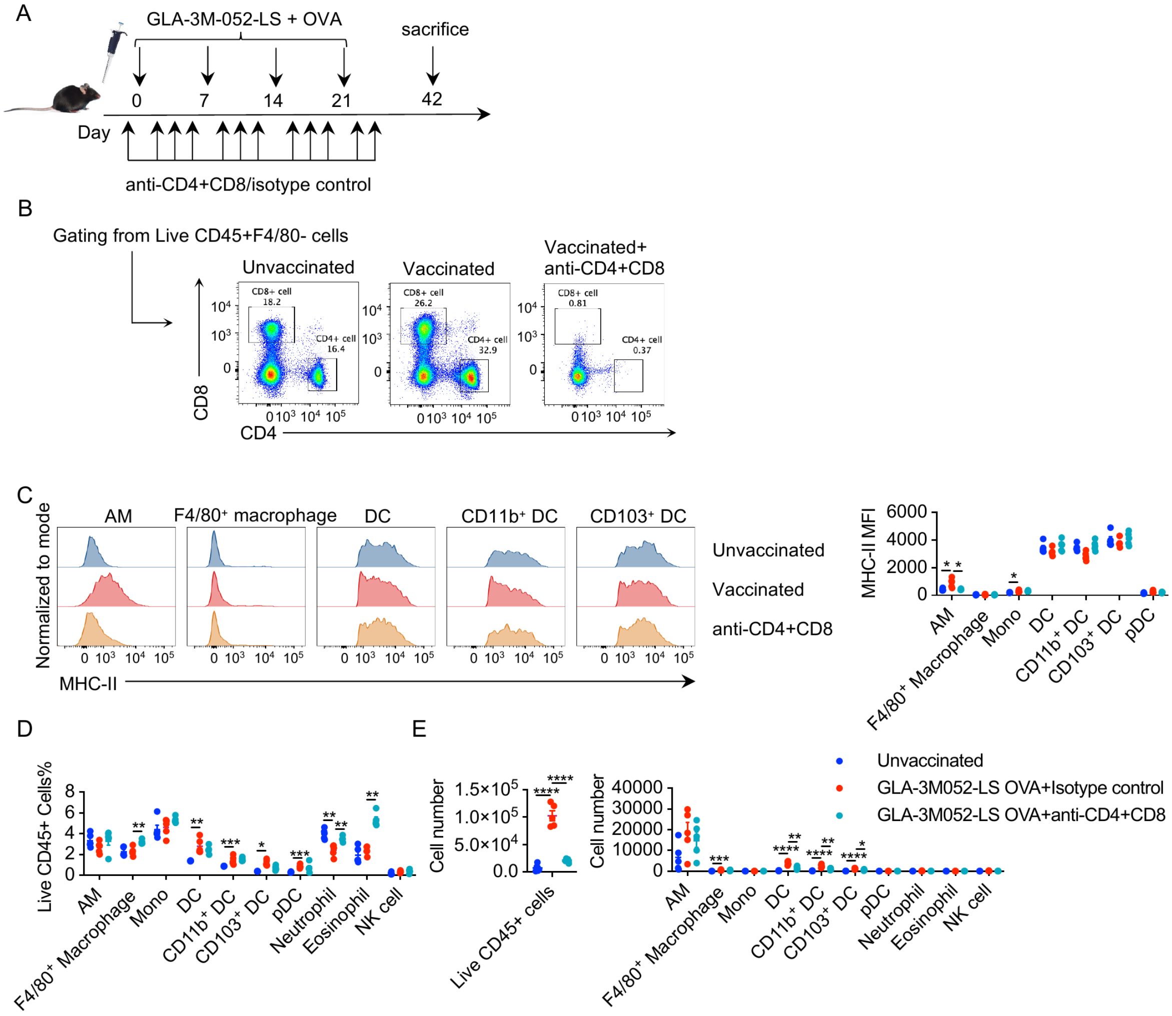

Fig. S11 Innate cell responses after $CD4^+$ and $CD8^+$ T cells blockade 21 days post-vaccinations. (A) Experimental design. (B) Representative flow cytometry plots of $CD4^+$ and $CD8^+$ cells in the lungs of unvaccinated mice, vaccinated mice, and vaccinated mice depleted of T cells. (C) Left: representative flow cytometry plots of MHC-II expression in alveolar macrophage (AM), F4/80^+ macrophage, DC, $CD11b^+$ DC, and $CD103^+$ DC. Right: MFI of MHC-II in indicated cell type of unvaccinated, vaccinated and vaccinated mice depleted of T cells, at 21 days post-four immunizations. (D) Indicated cell types percentage in live $CD45^+$ cells of unvaccinated, vaccinated, and vaccinated mice depleted of T cells, 21 days post-vaccinations. (E) Left: total cell numbers in BAL. Right: cell numbers of AM, F4/80^+ macrophage, Monocyte (Mono), DC, $CD11b^+$ DC, $CD103^+$ DC, pDC, Neutrophil, Eosinophil, and NK in BAL. $n = 5$ for each group. Each dot represents one mouse. Gating strategies can be found in Fig. S23A. Data are representative of at least two independent experiments. Significance was assessed by one-way ANOVA followed by Dunnett's multiple-comparison test for each group compared with GLA-3M-052-LS + OVA + isotype control group. Data are mean ± SEM ($^*P < 0.05$, $^{**}P < 0.01$, $^{***}P < 0.001$, $^{****}P < 0.0001$)

Fig. S12.

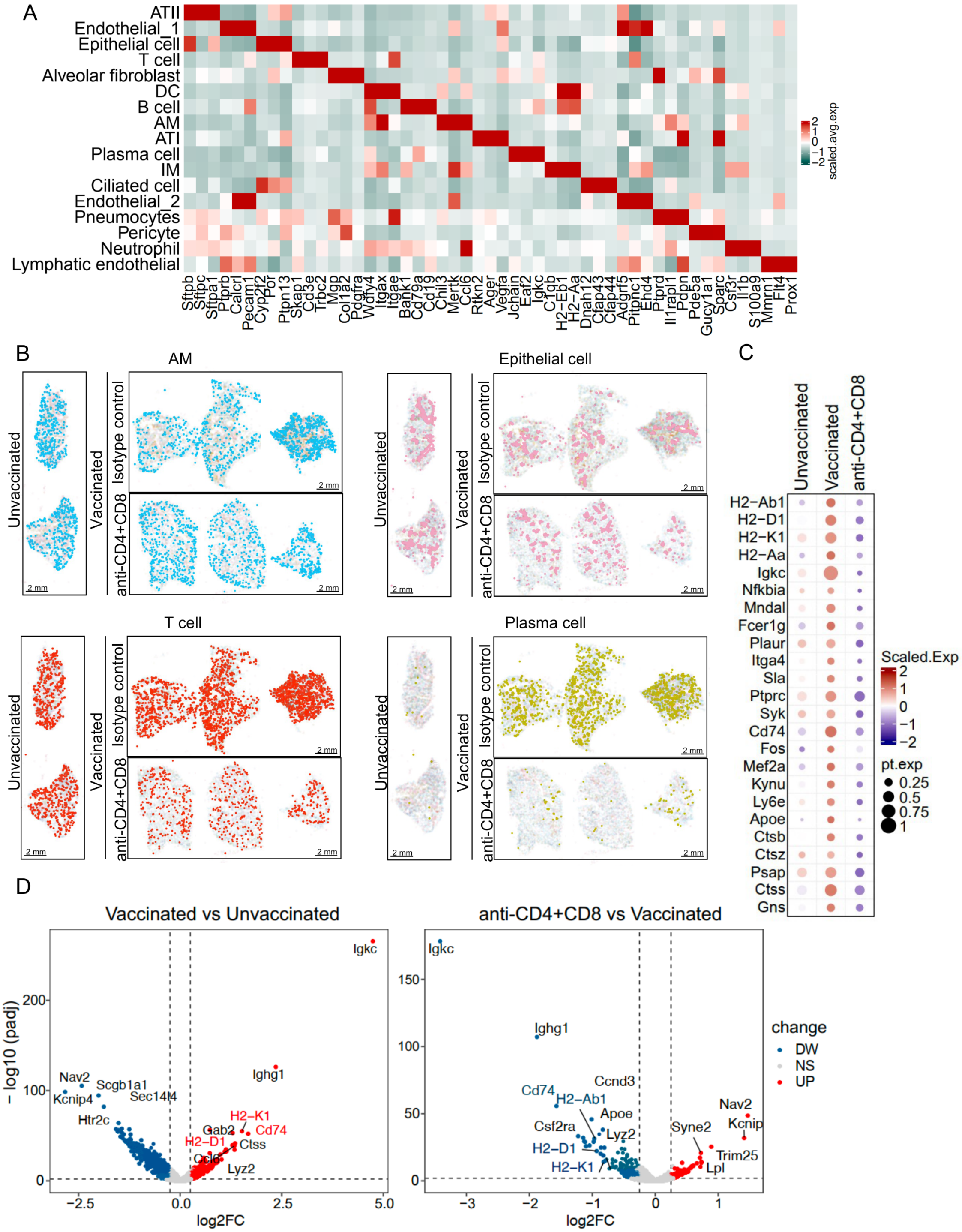

Fig. S12 Spatial transcriptomics analysis in lung. (A) Top variable genes defining cell clusters identified from spatial transcriptomics data. (B) Spatial mapping of representative cell types. Scale bar: 2 mm. (C) The bubble plot showing the representative expression changes of antigen presentation and phagocytosis-related differentially expressed genes. (D) Volcano plots of DEGs logFC in AM in vaccinated *vs* unvaccinated and vaccinated with CD4$^+$ and CD8$^+$ T cells blockade *vs* vaccinated mice groups. The upregulated antigen presentation genes were labeled red and downregulated antigen presentation genes were labeled blue.

Fig. S13.

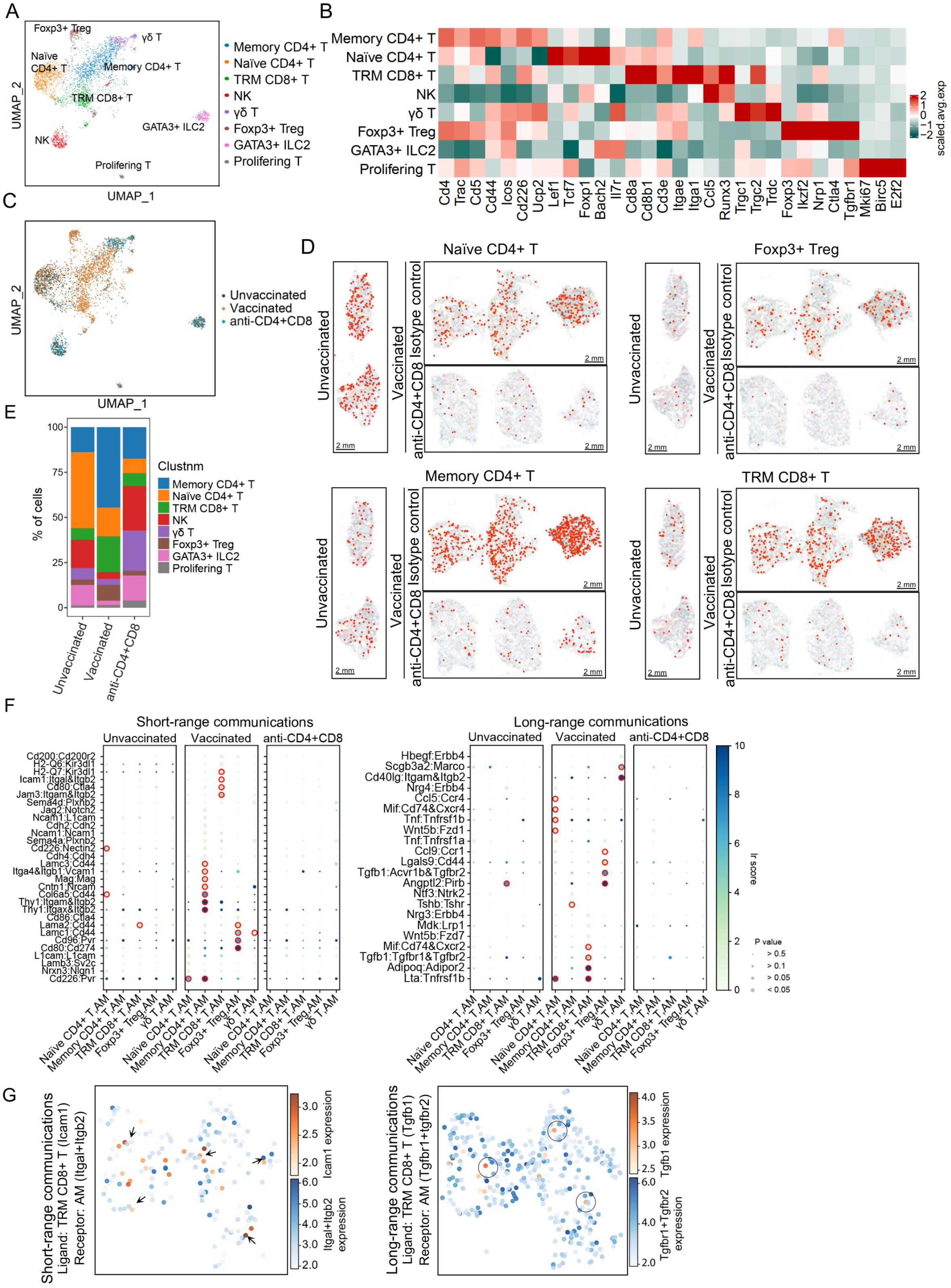
A
Foxp3+ Treg
γδ T
Naïve CD4+ T
Memory CD4+ T
TRM CD8+ T
GATA3+ ILC2
NK
Prolifering T
UMAP_2
UMAP_1
Memory CD4+ T
Naïve CD4+ T
TRM CD8+ T
NK
γδ T
Foxp3+ Treg
GATA3+ ILC2
Prolifering T
B
Memory CD4+ T
Naïve CD4+ T
TRM CD8+ T
NK
γδ T
Foxp3+ Treg
GATA3+ ILC2
Prolifering T
Cd4
Trac
Cd5
Cd44
Icos
Cd226
Ucp2
Lef1
Tcf7
Foxp1
Bach2
Il7r
Cd8a
Cd8b1
Cd3e
Itgae
Itga1
Ccl5
Runx3
Trgc1
Trgc2
Trdc
Foxp3
Ikzf2
Nrp1
Ctla4
Tgfbr1
Mki67
Birc5
E2f2
2
1
0
−1
−2
scaled.avg.exp
C
UMAP_2
UMAP_1
Unvaccinated
Vaccinated
anti-CD4+CD8
D
Naïve CD4+ T
Foxp3+ Treg
Memory CD4+ T
TRM CD8+ T
Unvaccinated
Vaccinated
Isotype control
anti-CD4+CD8
2 mm
E
100
75
50
25
0
% of cells
Unvaccinated
Vaccinated
anti-CD4+CD8
Clustnm
Memory CD4+ T
Naïve CD4+ T
TRM CD8+ T
NK
γδ T
Foxp3+ Treg
GATA3+ ILC2
Prolifering T
F
Short-range communications
Unvaccinated
Vaccinated
anti-CD4+CD8
Cd200:Cd200r2
H2-Q6:Kir3dl1
H2-Q7:Kir3dl1
Icam1:Itgal&Itgb2
Cd80:Ctla4
Jam3:Itgam&Itgb2
Sema4d:Plxnb2
Jag2:Notch2
Ncam1:L1cam
Cdh2:Cdh2
Ncam1:Ncam1
Sema4a:Plxnb2
Cd226:Nectin2
Cdh4:Cdh4
Lamc3:Cd44
Itga4&Itgb1:Vcam1
Mag:Mag
Cntn1:Nrcam
Col6a5:Cd44
Thy1:Itgam&Itgb2
Thy1:Itgax&Itgb2
Cd86:Ctla4
Lama2:Cd44
Lamc1:Cd44
Cd96:Pvr
Cd80:Cd274
L1cam:L1cam
Lamb3:Sv2c
Nrxn3:Nlgn1
Cd226:Pvr
Naïve CD4+ T.AM
Memory CD4+ T.AM
TRM CD8+ T.AM
Foxp3+ Treg.AM
γδ T.AM
Long-range communications
Unvaccinated
Vaccinated
anti-CD4+CD8
Hbegf:Erbb4
Scgb3a2:Marco
Cd40lg:Itgam&Itgb2
Nrg4:Erbb4
Ccl5:Ccr4
Mif:Cd74&Cxcr4
Tnf:Tnfrsf1b
Wnt5b:Fzd1
Tnf:Tnfrsf1a
Ccl9:Ccr1
Lgals9:Cd44
Tgfb1:Acvr1b&Tgfbr2
Angptl2:Pirb
Ntf3:Ntrk2
Tshb:Tshr
Nrg3:Erbb4
Mdk:Lrp1
Wnt5b:Fzd7
Mif:Cd74&Cxcr2
Tgfb1:Tgfbr1&Tgfbr2
Adipoq:Adipor2
Lta:Tnfrsf1b
Naïve CD4+ T.AM
Memory CD4+ T.AM
TRM CD8+ T.AM
Foxp3+ Treg.AM
γδ T.AM
10
8
6
4
2
0
lr score
P value
> 0.5
> 0.1
> 0.05
< 0.05
G
Short-range communications
Ligand: TRM CD8+ T (Icam1)
Receptor: AM (Itgal+Itgb2)
3.0
2.5
2.0
Icam1 expression
6.0
5.0
4.0
3.0
2.0
Itgal+Itgb2 expression
Long-range communications
Ligand: TRM CD8+ T (Tgfb1)
Receptor: AM (Tgfbr1+tgfbr2)
4.0
3.5
3.0
2.5
Tgfb1 expression
6.0
4.0
2.0
Tgfbr1+Tgfbr2 expression

Fig. S13 Spatial transcriptomic analysis of T cell subclusters in lung. (A) UMAP projection of 3,912 total cells clustered from T cells in Figure 3C. (B) Top variable genes defining T cell subclusters identified from spatial transcriptomic data. (C) UMAP visualization shows the distribution of distinct cell types across different samples. (D) Spatial mapping of representative T cell subclusters. Scale bar: 2 mm. (E) Stacked bar plot showing the percentage of T cell subsets within each group. (F) Bubble plots display the top differentially expressed ligand–receptor interactions between distinct T cell subsets and alveolar macrophage (AM) in short- (left) and long-range communication (right). Bubble size represents P value, and color indicates Interaction Ranking (Ir) score. (G) Left, representative short-range communications in the two vaccinated lung slides. Red level means relative Icam1 expression in TRM CD8$^+$ T cells. Blue level means relative Itgal+Itgb2 expression in AM. Arrows display representative sites of cell-cell short-range communications. Right, representative long-range communications in the two vaccinated lung slides. Red level means relative Tgfb1 expression in TRM CD8$^+$ T cells. Blue level means relative Tgfbr1+Tgfbr2 expression in AM. Circles display representative regions of long-range communication.

Fig. S14.

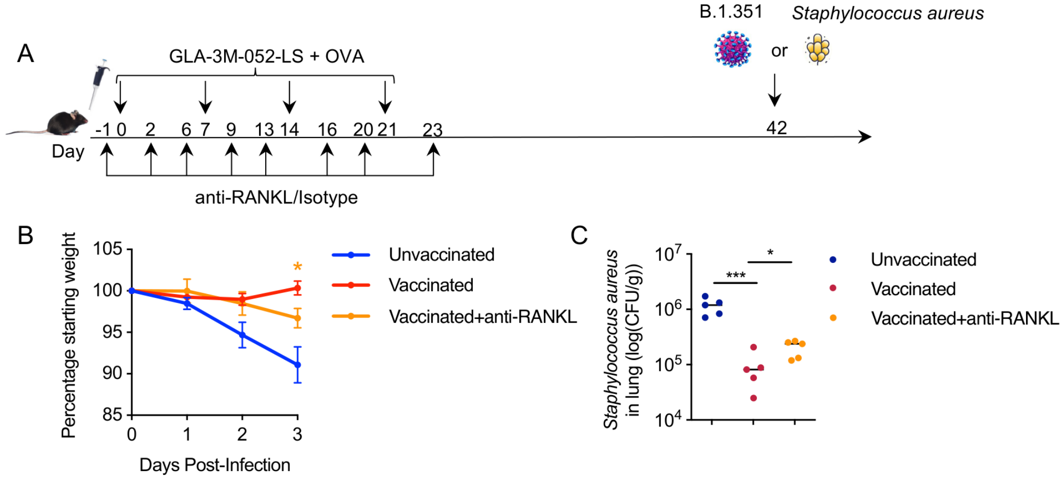

Fig. S14 RANKL mediates the protection conferred by GLA-3M-052-LS + OVA vaccination against SARS-CoV-2 and *Staphylococcus aureus* infection. (A) Experimental strategy. 250 µg/dose RANKL antibody was used at indicated time. (B) Body weight changes following SARS-CoV-2 infection. $n = 8$ unvaccinated mice, 8 vaccinated mice with isotype control antibody treatment, 9 vaccinated mice with RANKL antibody treatment. Colored asterisks indicate statistical significance between vaccinated group and vaccinated with anti-RANKL treatment group. (C) Bacterial load in the lung at one day after *Staphylococcus aureus* infection. $n = 5$ for each group. Significance was assessed by two-way ANOVA with Šidák's multiple-comparison test in (B) and one-way ANOVA with Šidák's multiple-comparison test in (C). Data are representative of at least two independent experiments. Data are mean ± SEM (*$P < 0.05$, ***$P < 0.001$).

Fig. S15.

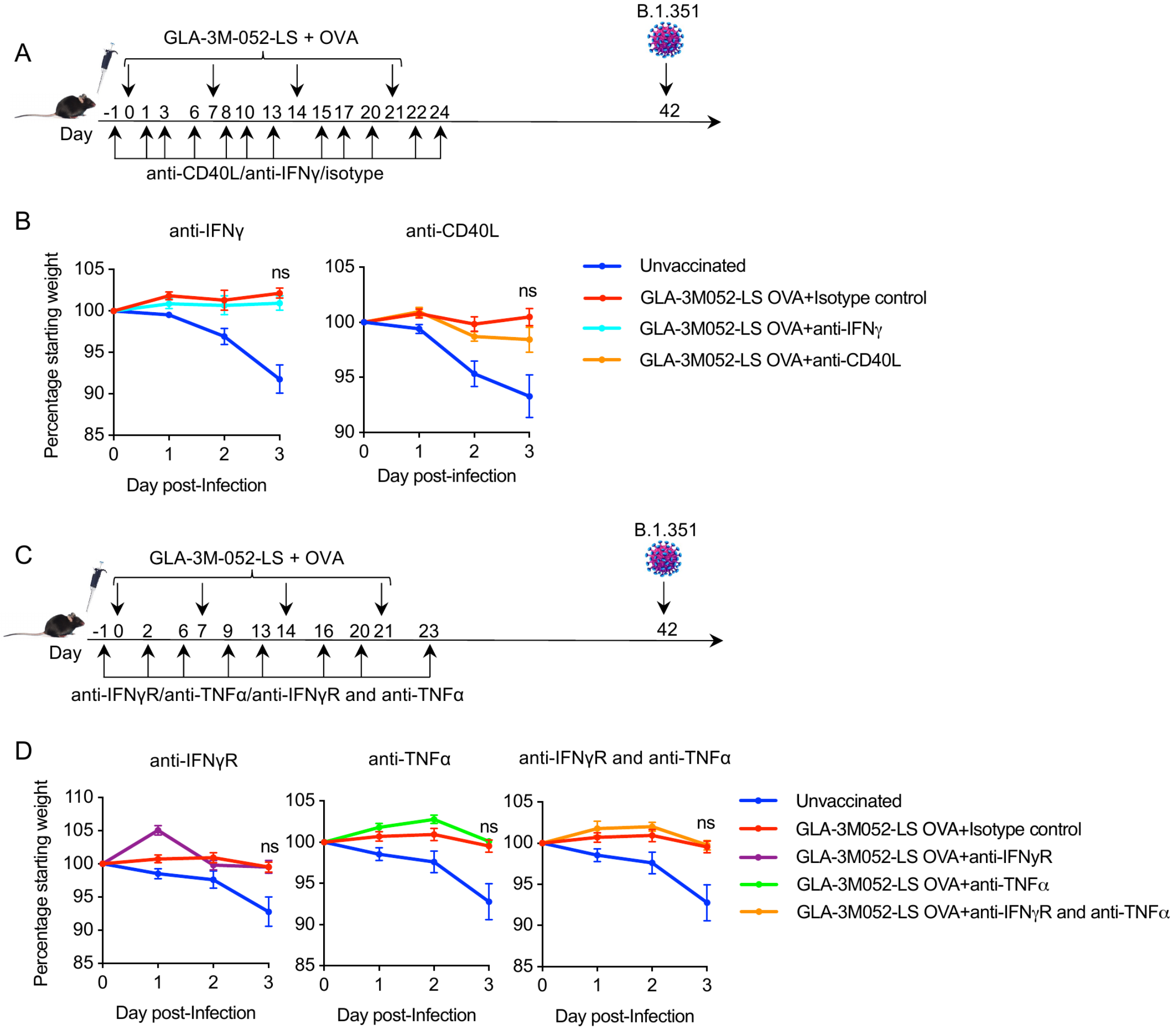

Fig. S15 CD40L, IFNγ, TNFα, IFNγR are not necessary for the protection. (A) Experimental strategy for (B). 250 μg/dose CD40L or 500 μg/dose IFNγ antibody were used in this experiment. (B) Body weight changes following SARS-CoV-2 infection. Left, *n* = 10 unvaccinated mice, 7 vaccinated mice with isotype control antibody treatment, 8 vaccinated mice with CD40L antibody treatment. Right, *n* = 8 unvaccinated mice, 5 vaccinated mice with isotype control treatment, 8 vaccinated mice with IFNγ antibody treatment. (C) Experimental strategy for (D). 250 μg/dose IFNγR and/or 250 μg/dose TNFα were used in this experiment. (D) Body weight changes following SARS-CoV-2 infection. *n* = 8 unvaccinated mice, 8 vaccinated mice with isotype control treatment, 8 vaccinated mice with IFNγR antibody treatment, 3 vaccinated mice with TNFα antibody treatment, 7 vaccinated mice with IFNγR and TNFα antibodies treatment. Data are representative of at least two independent experiments. Significance was assessed by two-way ANOVA with Šidák's multiple-comparison test. Data are mean ± SEM. ns indicates no significant difference between the vaccinated group and the vaccinated + antibody treatment group ($P > 0.05$).

Fig. S16.

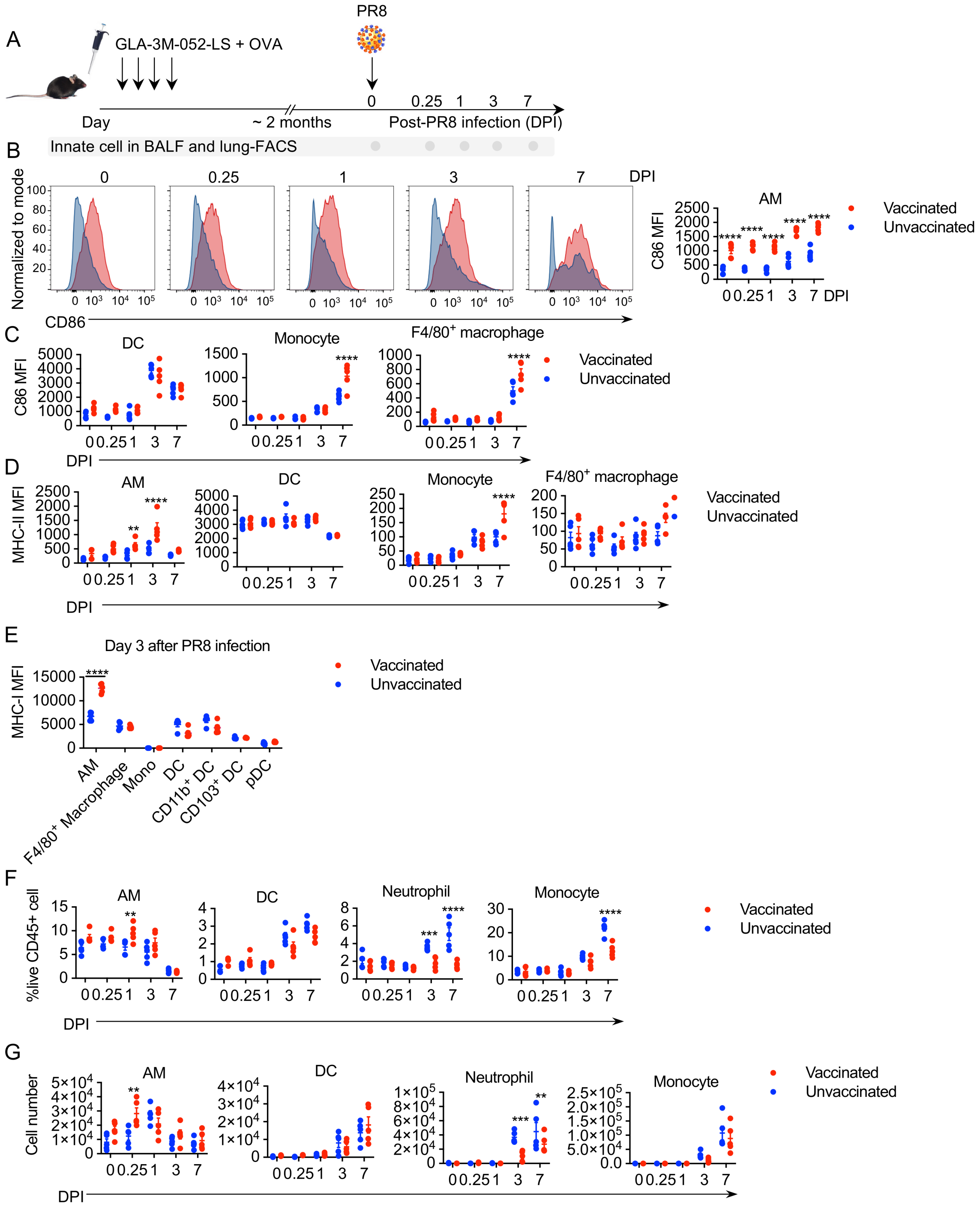

Fig. S16 Vaccinated AM were rapidly activated following PR8 infection. (A) Experimental design. Days post-PR8 infection (DPI). (B) Left: Representative flow cytometry plots of CD86 expression in AM at 0, 0.25, 1, 3, and 7 days post-PR8 infection. Right: MFI of CD86 in AM. (C) MFI of CD86 in DC, Monocyte, and F4/80$^+$ macrophage. (D) MFI of MHC-II in AM, DC, Monocyte, and F4/80$^+$ macrophage. (E) MFI of MHC-I in AM, F4/80$^+$ macrophage, Monocyte (Mono), and DC in lung at day 3 post PR8 infection. (F) Percentage of AM, DC, Neutrophil, and

Monocyte in live $CD45^+$ cells of lung. (G) Cell numbers of AM, DC, Neutrophil, and Monocyte in BAL. *n* = 5 mice in each group. Each dot represents one mouse. Gating strategies can be found in Fig. S23A. Data are representative of at least two independent experiments. Significance was assessed by two-way ANOVA with Šidák's multiple-comparison test. Data are mean ± SEM (**$P < 0.01$, ***$P < 0.001$, ****$P < 0.0001$)

Fig. S17.

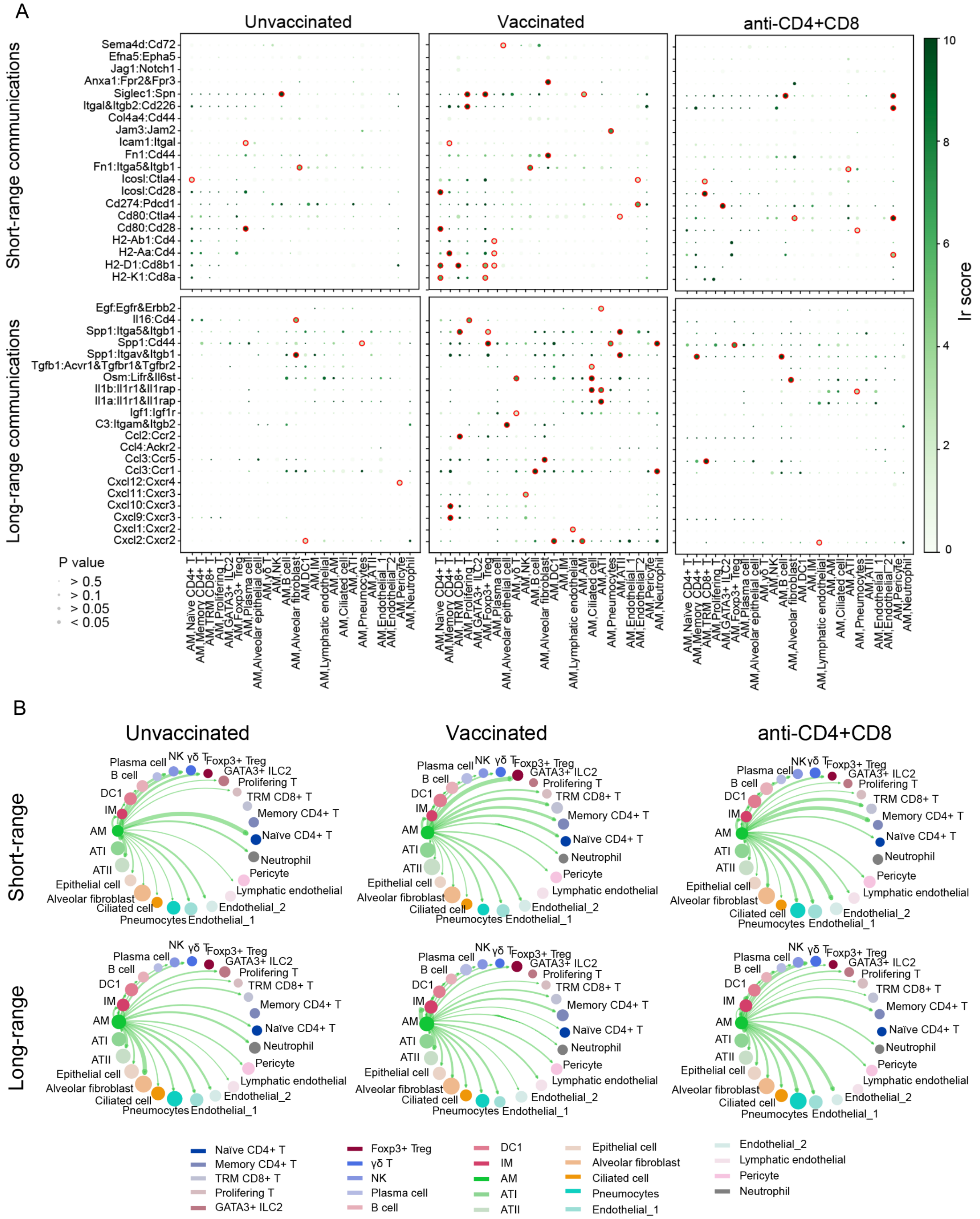

Fig. S17 Communications from AM to T cells and other cells based on spatial transcriptomic analysis. (A) Bubble plots display the top differentially expressed ligand–receptor interactions from alveolar macrophage (AM) to indicated cells in short- (up) and long-range communication (down). Bubble size represents *P* value, and color indicates Interaction Ranking (Ir) score. (B) Circle plots showing short- (up) and long- (down) range intercellular communication networks from AM to indicated cells. The thickness of the lines represents interaction event number, while the size of the circles indicates total number of interaction events.

Fig. S18.

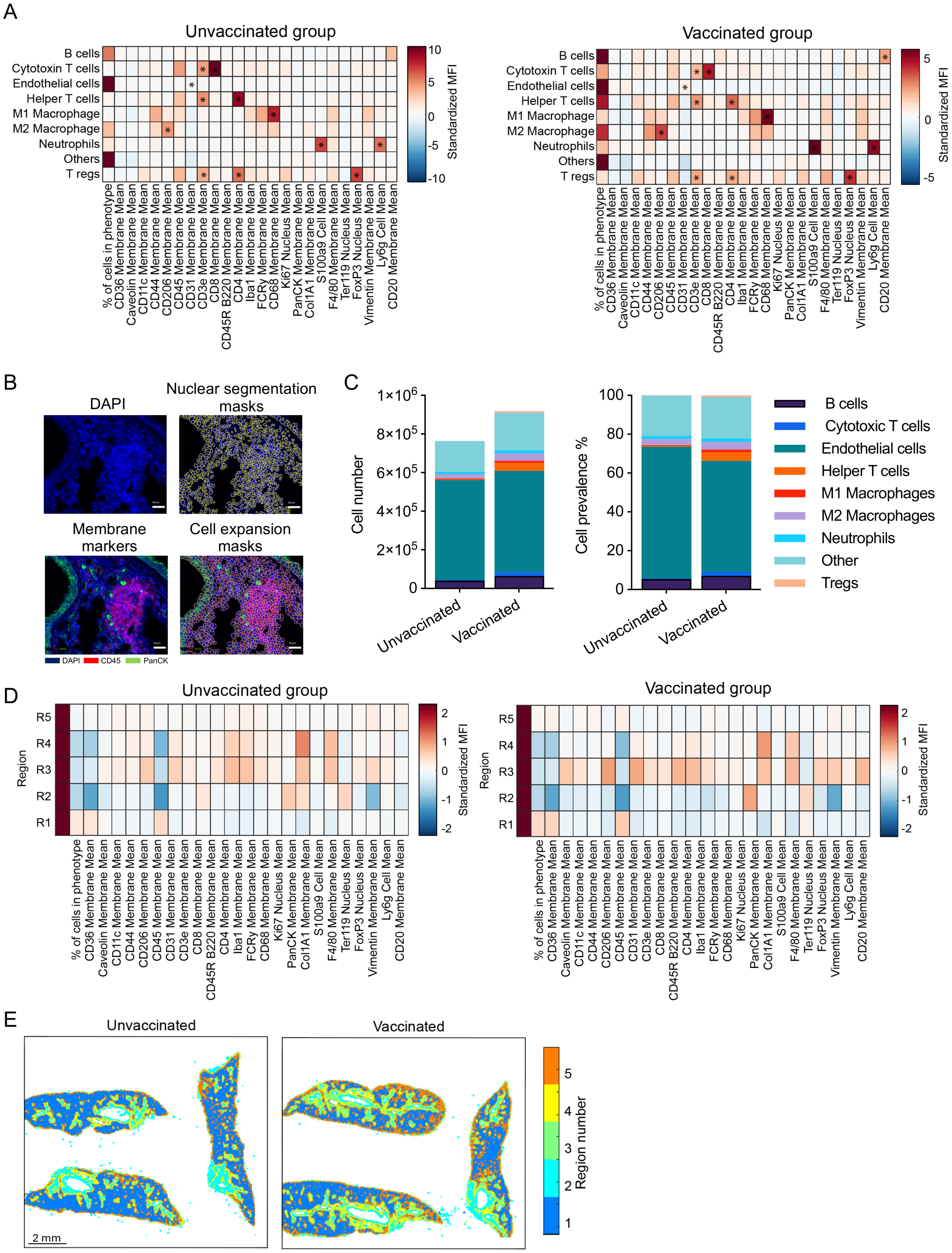

Fig. S18 Supplemental data for Figure 5. (A) Heatmap showing the standardized MFI of marker proteins in indicated cell types of (left) unvaccinated and (right) vaccinated mice on day 3 following SARS-CoV-2 infection. The positive signal in B cell (CD20$^+$), Cytotoxic T cells

($CD3e^+CD8^+$), Endothelial cells ($CD31^+$), Helper T cells ($CD3e^+CD4^+$), M1 Macrophage ($CD68^+CD206^-$ or weak), M2 Macrophage ($CD206^+$ $CD68^-$ or weak), Neutrophil ($Ly6g^+S100A9^+$), and Treg ($CD3e^+CD4^+FOXP3^+$) were marked. (B) Representative images demonstrating the strategy used to identify specific cell types. Scale bar: 40 μm. (C) Stacked bar plot showing the (left) cell number and (right) percentage of cell type within each group on day 3 after SARS-CoV-2 infection. (D) Heatmap showing the standardized MFI of marker genes in region 1-5 (R1-R5) of (left) unvaccinated and (right) vaccinated mice on day 3 following SARS-CoV-2 infection. (E) Representative images showing region 1-5 distribution in unvaccinated and vaccinated mice at day 3 after SARS-CoV-2 infection. Scale bar: 2 mm.

Fig. S19.

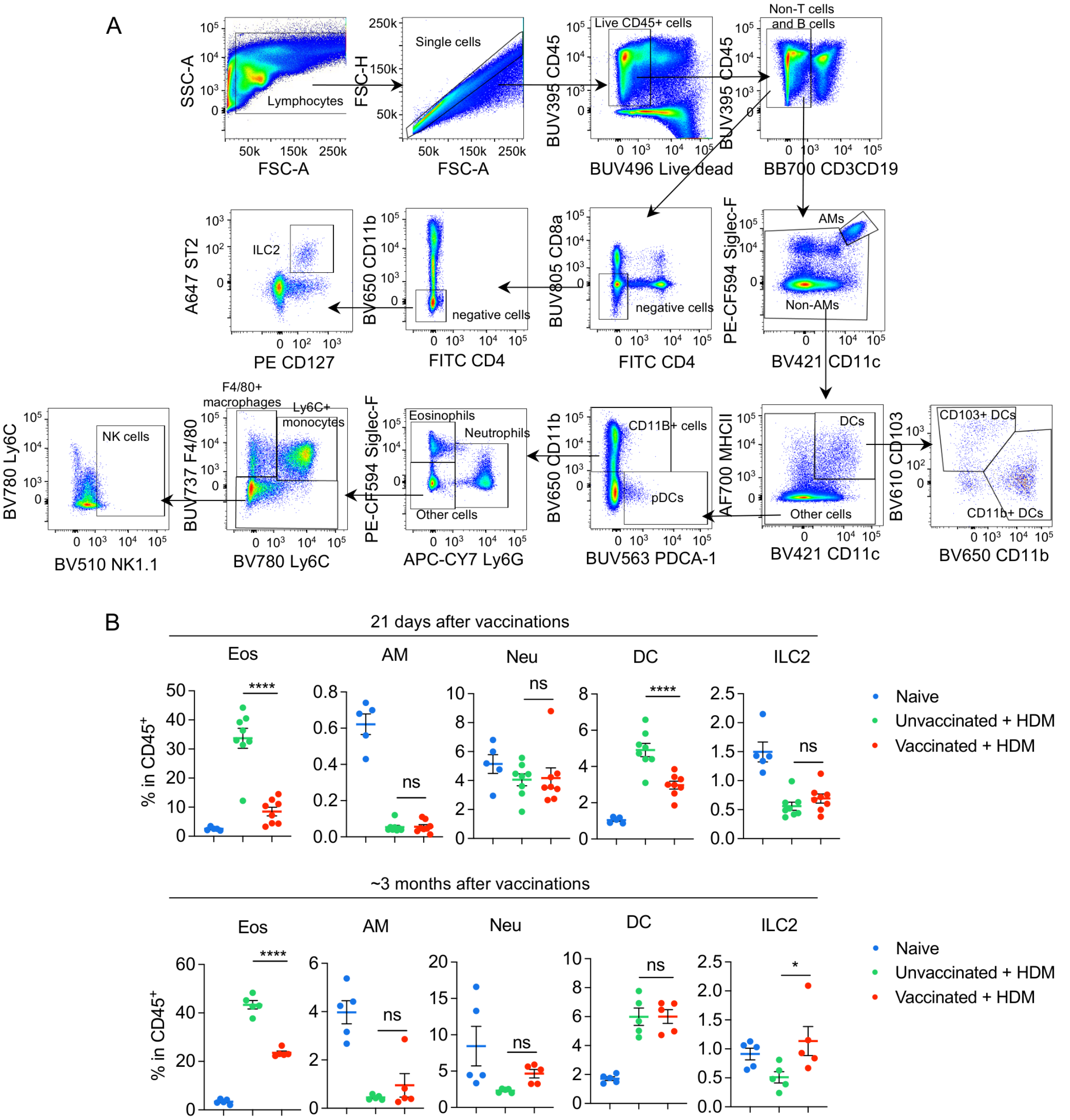

Fig. S19 Vaccination with GLA-3M-052-LS + OVA protects against allergic asthma. (A) Flow cytometric gating strategy for identifying innate immune cell subsets in the lung and BAL. For the phagocytosis experiments, only alveolar macrophages (AM) in BAL were tested. When assessing phagocytosis by AF594-labeled *S. aureus*, PE-CF594–Siglec-F was replaced with FITC–Siglec-F to avoid spectral overlap. (B) Percentage of Eosinophil (Eos), AM, Neutrophil (Neu), DC, ILC2 cells in lung live CD45$^+$ cells of (top) 21 days after vaccinations and (bottom) 3 months after vaccinations. *n* = 5 naïve mice, 8 mice for unvaccinated and HDM challenge, 8 mice for GLA-3M-052-LS + OVA vaccinated and HDM challenge (21 days after vaccinations) and *n* = 5 naïve mice, 5 mice for unvaccinated with HDM challenge, 5 mice for GLA-3M-052-LS + OVA vaccinated with HDM challenge (~3 months after vaccinations). Each dot represents one mouse. Data are representative of at least two independent experiments. Significance was assessed by one-way ANOVA with Šidák's multiple-comparison test. Data are mean ± SEM (ns $P > 0.05$, *$P < 0.05$, ****$P < 0.0001$).

Fig. S20.

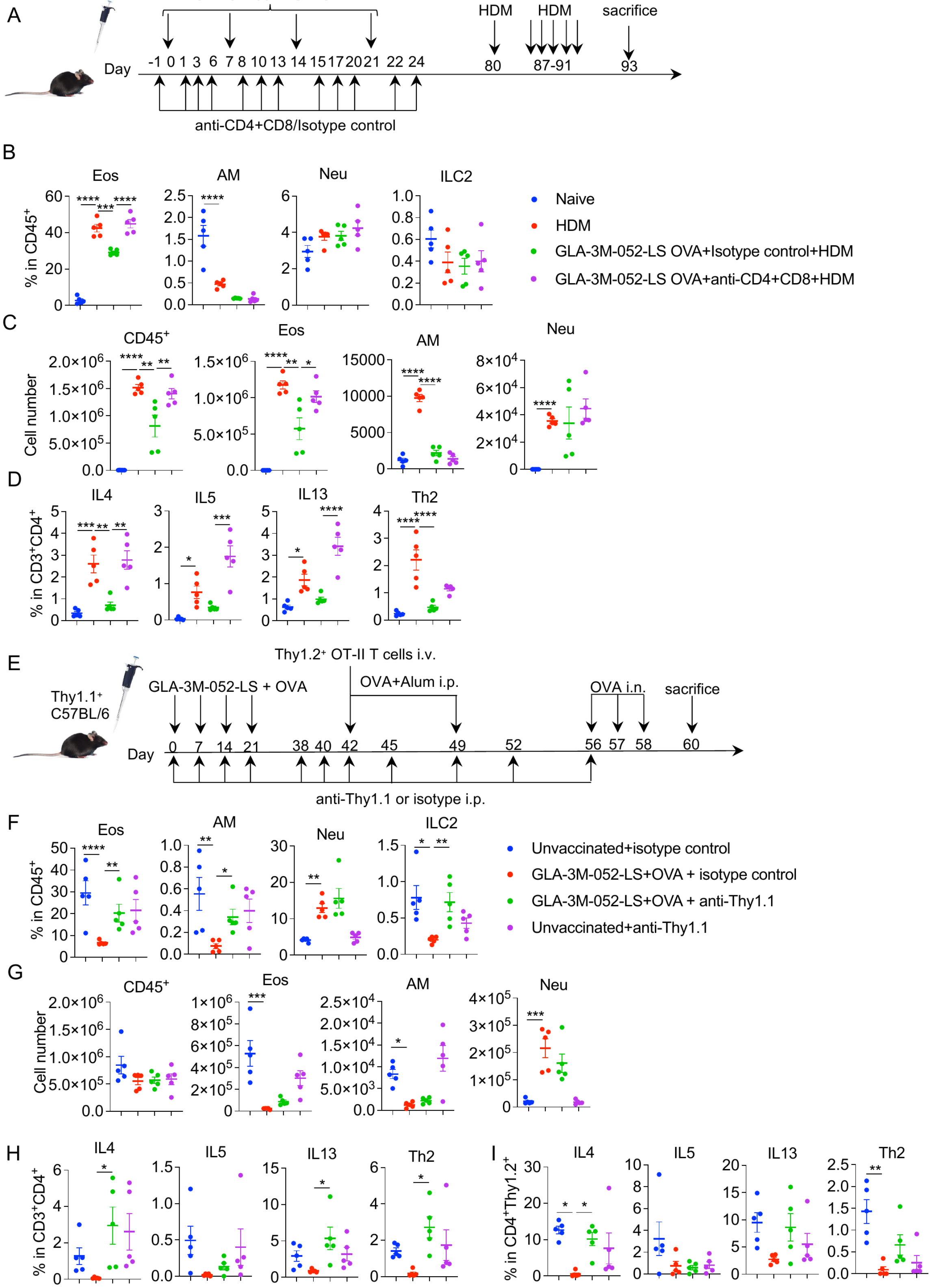
A
GLA-3M-052-LS + OVA
HDM
HDM
sacrifice
Day
-1 0 1 3 6 7 8 10 13 14 15 17 20 21 22 24
80
87-91
93
anti-CD4+CD8/Isotype control
B
Eos
AM
Neu
ILC2
% in CD45+
Naive
HDM
GLA-3M-052-LS OVA+Isotype control+HDM
GLA-3M-052-LS OVA+anti-CD4+CD8+HDM
C
CD45+
Eos
AM
Neu
Cell number
D
IL4
IL5
IL13
Th2
% in CD3+CD4+
E
Thy1.2+ OT-II T cells i.v.
Thy1.1+ C57BL/6
GLA-3M-052-LS + OVA
OVA+Alum i.p.
OVA i.n.
sacrifice
Day
0 7 14 21 38 40 42 45 49 52 56 57 58 60
anti-Thy1.1 or isotype i.p.
F
Eos
AM
Neu
ILC2
% in CD45+
Unvaccinated+isotype control
GLA-3M-052-LS+OVA + isotype control
GLA-3M-052-LS+OVA + anti-Thy1.1
Unvaccinated+anti-Thy1.1
G
CD45+
Eos
AM
Neu
Cell number
H
IL4
IL5
IL13
Th2
% in CD3+CD4+
I
IL4
IL5
IL13
Th2
% in CD4+Thy1.2+

Fig. S20 Blockade of CD4$^+$ and CD8$^+$ T cells abrogated the protective effects of vaccination against asthma. (A) Experimental strategy for (B to D). (B) Percentage of Eosinophil (Eos), AM, Neutrophil (Neu), and ILC2 cells in lung live CD45$^+$ cells. (C) Cell number of CD45$^+$ cells, Eos, AM, and Neu cells in the BAL. (D) The percentage of IL4$^+$, IL5$^+$, IL13$^+$ and Th2 cells (GATA3$^+$) in lung CD4$^+$ T cells. (E) Experimental strategy for (F to I). (F) Percentage of Eos, AM, Neu, and ILC2 cells in lung live CD45$^+$ cells. (G) Cell number of CD45$^+$ cells, Eos, AM, and Neu cells in the BAL. (H) The percentage of IL4$^+$, IL5$^+$, IL13$^+$ and GATA3$^+$ cells (Th2) in CD4$^+$ T cells or in (I) Thy1.2$^+$CD4$^+$ T cells. $n = 5$ for each group. Each dot represents one mouse. Gating strategies can be found in Fig. S23A. Data are representative of at least two independent experiments. Significance in (B to D) were assessed by one-way ANOVA followed by Tukey's multiple-comparison test. Significance in (F to I) were assessed by two-way ANOVA followed by Šidák's multiple-comparison test. Data are mean ± SEM (*$P < 0.05$, **$P < 0.01$, ***$P < 0.001$, ****$P < 0.0001$).

Table S1. List of antibodies used in depletion in vivo

In vivo depletion antibodies				
Target / Isotype Control	**Clone**	**Host / Isotype**	**Vendor**	**Catalog No.**
Anti-mouse CD4	GK1.5	Rat IgG2b	Bio X Cell	BE0003-1
Anti-mouse CD8β	53-5.8	Rat IgG1	Bio X Cell	BE0223
Anti-mouse IFN-γ	XMG1.2	Rat IgG1	Bio X Cell	BE0055
Anti-mouse IFN-γR	GR-20	Rat IgG2a	Bio X Cell	BE0029
Anti-mouse TNF-α	XT3.11	Rat IgG1	Bio X Cell	BP0058
Anti-mouse CD40L (CD154)	MR-1	Armenian hamster IgG	Bio X Cell	BE0017
Anti-mouse RANKL (CD254)	IK22/5	Rat IgG2a	Bio X Cell	BE0191
Anti-mouse Thy1.1	19E12	Mouse IgG2a	Bio X Cell	BE0214
Isotype control (Rat IgG1)	HPRN	Rat IgG1	Bio X Cell	BE0088
Isotype control (Rat IgG2b)	LTF-2	Rat IgG2b	Bio X Cell	BE0090
Isotype control (Rat IgG2a, anti-TNP)	2A3	Rat IgG2a	Bio X Cell	BE0089
Isotype control (Mouse IgG2a)	C1.18.4	Mouse IgG2a	Bio X Cell	BE0085
Polyclonal Armenian hamster IgG	Polyclonal	Armenian Hamster IgG	Bio X Cell	BE0091
Dilution Buffer (pH 6.5)	—	—	Bio X Cell	IP0065
Dilution Buffer (pH 7.0)	—	—	Bio X Cell	IP0070

Table S2. List of flow antibodies.

Flow cytometry Antibodies						
Target	**Fluorophore**	**Dilution**	**Panel**	**Vendor**	**Clone/peptide**	**Catalog Number**
anti-mouse CD103	PE	1:200	T cells	BioLegend	2E7	121406
anti-mouse CD103	BV610	1:400	Innate cells	BD	M290	748257
anti-mouse CD11b	BV650	1:200	Innate cells	BioLegend	M1/70	101239
anti-mouse CD11c	BV421	1:200	Innate cells	BioLegend	N418	117330
anti-mouse CD127	PE	1:100	Innate cells	BioLegend	A7R34	135010
anti-mouse CD16/32		1:200	all	BD	2.4G2	553141
anti-mouse CD19	BB700	1:200	Innate cells	BD	1D3	566411
anti-mouse CD3	BV785	1:50	T cells	BD	145-2C11	564379
anti-mouse CD3	BB700	1:200	Innate cells	BD	17A2	742175
anti-mouse CD4	BV650	1:200	T cells, TRM	BioLegend	RM4-5	100555
anti-mouse CD4	FITC	1:200	Innate cells	Alexa Fluor 488	GK1.5	100423
anti-mouse CD44	BV421	1:500	T cells, TRM	BioLegend	IM7	103040
anti-mouse CD45	BUV395	1:200	Innate cells, T cells	BD	30-F11	564279
anti-mouse CD45	BV605	3 ug/mouse	TRM	BioLegend	30-F11	103140
anti-mouse CD69	PE-Cy7	1:200	TRM	BioLegend	H1.2F3	104511
anti-mouse CD86	PE-Cy7	1:200	Innate cells	BD	GL1	560582
anti-mouse CD8a	BUV805	1:200	Innate cells	BD	53-6.7	612898
anti-mouse CD8α	BV711	1:200	T cells, TRM	BD	53-6.7	563046
anti-mouse CD90.1	BUV737	1:200	T cells	BD	OX-7	612837
anti-mouse CD90.2	PE-Cy7	1:200	T cells	BioLegend	53-2.1	140309
anti-mouse F4/80	BUV737	1:200	Innate cells	BD	T45-2342	749283
anti-mouse Foxp3	Alexa Fluor 488	1:100	T cells	BioLegend	MF-14	126406
anti-mouse GATA3	PE-Cy7	1:100	T cells	BD	L50-823	560405
anti-mouse IFN-γ	APC	1:100	T cells	BioLegend	XMG1.2	505810
anti-mouse IL-13	BUV805	1:100	T cells	Invitrogen	eBio13A	368-7133-82
anti-mouse IL-17A	BUV737	1:100	T cells	eBioscience	eBio17B7	367-7177-82
anti-mouse IL-2	PE	1:100	T cells	BioLegend	JES6-5H4	503808
anti-mouse IL-4	PE-CF594	1:100	T cells	BD	11B11	562450
anti-mouse IL-5	PE	1:100	T cells	BioLegend	TRFK5	504304
anti-mouse Ly6C	BV780	1:200	Innate cells	BioLegend	HK1.4	128041
anti-mouse Ly6G	APC-Cy7	1:200	Innate cells	BioLegend	1A8	127624
anti-mouse MHC-I	FITC	1:200	Innate cells	BioLegend	AF6-88.5	114605
anti-mouse MHC-II	Alexa Fluor 700	1:200	Innate cells	BioLegend	M5/114.15.2	107622
anti-mouse NK1.1	BV510	1:400	Innate cells	BioLegend	PK136	108738
anti-mouse PDCA-1	BUV563	1:400	Innate cells	BD	927	749275
anti-mouse Siglec-F	PE-CF594	1:200	Innate cells	BD	E50-2440	562757
anti-mouse Siglec-F	FITC	1:200	Phegocytosis (AF594 S.aureus)	BioLegend	S17007L	155503
anti-mouse ST2	APC	1:100	Innate cells	eBioscience	RMST2-2	12-9335-82
anti-mouse TCRβ	BUV737	1:200	TRM	BD	H57-597	612821
anti-mouse TNFα	FITC	1:100	T cells	BioLegend	MP6-XT22	506304
Ghost Dye Violet 510	Violet 510	1:300	T cells, TRM	Tonbo Bioscience		13-0870-T100
Zombie UV viability dye	BUV496	1:300	Innate cells	BioLegend		423107
NP Class I Tetramer	APC	1:100	T cells	NIH Tetramer Core Facility	ASNENMETM	
OVA Class I Tetramer	APC	1:100	T cells	NIH Tetramer Core Facility	SIINFEKL	
OVA Class II Tetramer	PE	1:50	T cells	NIH Tetramer Core Facility	AAHAEINEA	

Table S3. List of antibodies used in scRNA-seq

Ab-seq Antibodies				
Name	**Clone**	**Vendor**	**Catalog Number**	**Oligo Type / Application**
anti-mouse CD3ε	145-2C11	BD Biosciences	940107	BD AbSeq oligo-conjugated antibody (CITE-seq/AbSeq)
anti-mouse CD19	1D3	BD Biosciences	940111	BD AbSeq oligo-conjugated antibody (CITE-seq/AbSeq)
anti-mouse CD4	RM4-5	BD Biosciences	940108	BD AbSeq oligo-conjugated antibody (CITE-seq/AbSeq)
anti-mouse CD8α	53-6.7	BD Biosciences	940345	BD AbSeq oligo-conjugated antibody (CITE-seq/AbSeq)
anti-mouse CD18	C71/16	BD Biosciences	940480	BD AbSeq oligo-conjugated antibody (CITE-seq/AbSeq)
anti-mouse CD11c	HL3	BD Biosciences	940112	BD AbSeq oligo-conjugated antibody (CITE-seq/AbSeq)
anti-mouse CD11c BV421	N418	BioLegend	117330	
anti-mouse CD11b BV650	M1/70	BioLegend	101239	
anti-mouse CD326 (EpCAM) BV510	G8.8	BD Biosciences	563216	
anti-mouse CD3ε	17A2	BD Biosciences	742175	
Zombie UV viability dye BUV496		BioLegend	423107	

Table S4. List of antibodies used in CODEX staining

CODEX antibodies				
Antibody	**Clone**	**Reporter**	**Dilution**	**Exposure**
CD36-BX002	E8B7S	Atto550-RX002	1:200	150
CD11c-BX024	D1V9Y	AF647-RX024	1:100	150
Caveolin-BX086	D46G3	AF750-RX086	1:200	150
CD44-BX005	E7K2Y	Atto550-RX005	1:200	150
CD206-BX016	E6T5J	AF647-RX016	1:200	100
CD45-BX021	D3F8Q	Atto550-RX021	1:300	70
CD3e-BX080	E4T1B	AF647-RX080	1:200	60
CD31-BX001	D8V9E	AF750-RX001	1:200	150
CD8-BX026	EPR21769	Atto550-RX026	1:200	150
CD4-BX003	D7D27	AF647-RX003	1:100	150
CD45R/B220-BX010	Ra3-6B2	AF750-RX010	1:150	150
Iba1-BX014	E4O4W	Atto550-RX014	1:400	50
CD68-BX015	E307V	AF647-RX015	1:1200	20
FCRγ-BX037	E6Y1A	AF750-RX037	1:200	150
Ki67-BX047	B56	Atto550-RX047	1:200	70
Col1A1-BX042	E8F4L	AF647-RX042	1:600	50
PanCK-BX066	AE-1/AE-3	AF750-RX066	1:200	150
F4/80-BX006	D2S9R	AF647-RX006	1:200	125
S100A9-BX025	D3U8M	AF750-RX025	1:200	20
FoxP3-BX031	D6O8R	AF647-RX031	1:200	150
Ter119-BX004	TER-119	AF750-RX004	1:200	150
Ly6g-BX017	E6Z1T	AF647-RX017	1:200	20
Vimentin-BX022	D21H3	AF750-RX022	1:200	80
CD20-BX064	E3N70	AF750-RX064	1:200	50

Table S5. The results of QC scores for the CODEX staining

Markers	S789 (vaccinated)	S404142(unvaccinated)
CD36	2	2
Caveolin	2	2
CD11c	0	0
CD44	2	2
CD206	3	3
CD45	2	2
CD31	2	2
CD3e	2	2
CD8	2	2
CD45R/B220	1	0
CD4	2	2
Iba-1	2	2
FCRy	2	2
CD68	3	3
Ki67	2	2
PanCK	2	2
Col1A1	3	3
S100A9	2	2
F4/80	2	2
Ter119	2	2
FoxP3	2	1
Vimentin	3	3
Ly6g	2	2
CD20	2	2

Score	Interpretation	Include in analysis
-1	non-specific binding	no
0	no signal	no
1	weak signal	no
2	good staining	yes
3	saturated	yes

Table S6. Phenotypes and their corresponding markers for the CODEX staining

#	Phenotypes	Markers
1	B cells	CD20+
2	Cytotoxic T cells	CD3e+, CD8+
3	Endothelial cells	CD31+
4	Helper T cells	CD3e+, CD4+
5	M1 Macrophages	CD68+, CD206- or weak
6	M2 Macrophages	CD206+, CD68- or weak
7	Neutrophils	Ly6g+, S100A9+
8	Tregs	CD3e+, CD4+, FOXP3+
9	Other	All negative for above markers